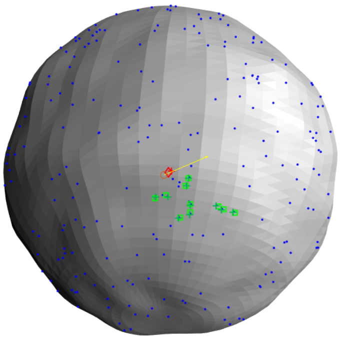

Advanced On-board Navigation Techniques for Disrupted Complex Asteroid Rotators

José António Severino Medeiro

Thesis to obtain the Master of Science Degree in

Aerospace Engineering

Supervisors: Prof. Pedro Tiago Martins Batista
Eng. Francisco da Silva Pais Cabral

Examination Committee

Chairperson: Prof. Paulo Sérgio de Brito André
Supervisor: Eng. Francisco da Silva Pais Cabral
Member of the Committee: Prof. Bruno João Nogueira Guerreiro

December 2024

Declaration

I declare that this document is an original work of my own authorship and that it fulfills all the requirements of the Code of Conduct and Good Practices of the Universidade de Lisboa.

Acknowledgments

The thesis the reader is about to read is the culmination of my journey at IST, a long travel of five years. In it, I was lucky enough to not only enrich myself academically, with each professor leaving in me more knowledge and wisdom, but also had the opportunity to meet colleagues from all around Portugal, with each one imprinting a mark on me and, for sure, turning me into a better person.

To start, I would like to express my gratitude to my supervisors, Prof. Pedro Batista and Eng. Francisco Cabral, having been both a pleasure and honour to been advised by them. I thank Prof. Pedro Batista for his role in kindling my interest for the Control field during his Introduction to Automatic Control course, leading to my current path. It is hard to imagine a more fitting supervisor to mark my Masters' conclusion, reinforcing my view of him as a great academic and great person. It is impossible to not mention the fantastic mentorship of Eng. Francisco Cabral, with his constant patience, guidance and extensive wisdom permeating all of the work here presented.

Secondly, I want to thank the friends that I made along my path at IST, and turned the, sometimes exhaustive, time at this faculty an experience worth remembering fondly. In particular, I want to thank two different groups of people. Firstly, to my dearest group from Bachelors, João, Mafalda, and Manuel, with who I had the joy to spend considerable time since the start, sharing countless adventures and growing as a person, and for that I can count myself lucky. However, my Masters was also shaped by the presence of Pratas, Carneiro, Duarte, Peixoto, Mariana and Vale. Each one of them left a lasting impression on me, be it their fellowship during my fourth year attending classes at IST, their deep commitment for every project in which they immersed themselves or the roller-coaster that was our AeroTéc's Executive Board term.

Thirdly, I can't overstate how important was Rafaela during the last two years. Our relationship was a beacon of light during this time. Her support, funniness and companionship made me not only survive but thrive, both here in Lisbon as well as abroad in Aachen.

Fourthly, I leave here my deepest appreciation for the support and caring of my family. Without them I wouldn't have grown up to become who I am. They are the embodiment of hard and honest work, cultivating in me the integrity and willingness to fight that I have, and allowing me to fly into heights that a couple generations ago would have been seen as an unthinkable dream.

Fifthly, I would like to thank my colleagues at GMV for making this last semester an enjoyable experience. The lunches of Pingo Doce, small banter and overall happiness raised my moral and carried my through the weeks.

Finally, I want to thank GMV for financing this work under its master thesis internship program, having provided also the tools to achieve the desired objectives and the environment in which to successfully and pleasantly work.

Resumo

A passagem de Apophis pela Terra, em 2029, trará uma oportunidade única para estudar a sua composição, a história de asteroides semelhantes e os efeitos de torques gravitacionais significativos num corpo grande. Para o estudar, uma nave espacial terá de estimar a sua posição e velocidade relativas. Além disso, se for pretendido estudar a perturbação da rotação do asteroide, a atitude e a velocidade angular de Apophis são também de interesse. A estimativa de tais valores tem de ser feita com recurso a sensores relativos, tal como LiDARs e câmaras. Esta tese apresenta uma estratégia de navegação que permite estimar as grandezas mencionadas, recorrendo a medições da distância relativa e da direção ao alvo, em conjunto com a direção a caraterísticas superficiais desconhecidas, auto-inicializando-as com um modelo simplificado do asteroide. A solução proposta baseia-se no filtro de Kalman multiplicativo estendido, um tipo de filtro que separa os estados numa versão nominal e de erro, permitindo um tratamento mais conveniente dos estados de representação da atitude. Inclusive, o filtro pode utilizar parâmetros de consideração, algo crucial para lidar com os vieses não observáveis da medição e incertezas dinâmicas, tais como os torques exercidos pela Terra sobre Apophis. A solução proposta foi exaustivamente analisada através de simulações de Monte Carlo, criando diferentes variantes de filtro para comparar o desempenho da solução. Os resultados são promissores, sendo a solução proposta capaz de seguir a atitude de Apophis e melhorar consideravelmente a estimativa da posição da nave espacial.

Palavras-chave: estimação de atitude, Apophis, mecânica orbital, filtro de Kalman multiplicativo extendido

Abstract

Apophis' close fly-by to Earth in 2029 will bring a prime opportunity to study its composition, history of similar asteroids, and the effects of a significant gravitational torque on a relatively large body. To study it, a spacecraft will have to estimate its relative position and velocity. Furthermore, if one is to study the disruption of the asteroid's rotation, the Apophis' attitude and angular velocity are also quantities of interest. The estimation of such values needs to be performed using relative sensors, with LiDARs and cameras being prime examples. This thesis presents a navigation strategy that estimates the quantities mentioned, resorting to relative distance and relative direction to the target, alongside the relative direction of unknown features, resorting to a self-initialization method with a simplified model of the asteroid. The proposed solution is based upon the multiplicative extended Kalman filter, a type of filter that separates the states into a nominal and error version, allowing a more convenient handling of attitude representation states. Moreover, the filter can consider parameters, crucial to deal with unobservable measurement biases and dynamic uncertainties, such as the torques exerted by Earth on Apophis. The proposed solution was thoroughly analysed through Monte Carlo simulations, with different filter variants created to compare the solution's performance. The results are promising, with the proposed solution able to track the Apophis' attitude and vastly improve the spacecraft's position estimate even if resorting to unknown features.

Keywords: attitude estimation, Apophis, on-orbit mechanics, multiplicative extended Kalman filter, simultaneous localization and mapping

Contents

List of Tables

List of Figures

Nomenclature

Operations

$\times$	Cross product
$\odot$	Quaternion product

Roman symbols

$\mathcal{AP}$	Apophis reference frame
$\mathcal{CI}$	Centred inertial reference frame
$\mathcal{SC}$	Spacecraft reference frame
$\mathcal{CA}$	Camera reference frame

Subscripts

i	Index
c	Centroiding related value
l	LiDAR related value
ft	Feature tracking related value

Superscripts

*	Conjugate
T	Transpose

Glossary

EKF	Extendend Kalman Filter
EO	Electro-Optical
FOGM	First Order Gauss Markov process noise
FoV	Field of View
IP	Image Processing
KF	Kalman Filter
LiDAR	Light Detection And Ranging
MEKF	Multiplicative Extended Kalman Filter
PnP	Perspective-n-Point Problem
SC	Spacecraft

Chapter 1

Introduction

1.1 Motivation

Space missions have increased in complexity throughout the years, carrying more sensible instruments, aiming for more ambitious goals and even being composed of more than one spacecraft (SC). This drive for larger objectives, in conjunction with other factors such as the desire for cost reduction, employment of multiple missions occurring simultaneously and intrinsic communication difficulties have pushed key actors, like NASA, to invest in the on-board automation of spacecrafts [1, 2].

One major aspect of the automation of space missions is the development of navigation systems, tasked with estimating the SC states at any given time, allowing the rest of the SC subsystems to perform accordingly, from deciding where to point its camera to better capture an image of its objective to how much force should commanded to the thrusters to not crash onto it. These navigation systems require, in turn, measurements of the environment and the SC states, in order to provide adequate estimates.

For space missions, eletro-optical (EO) sensors, usually called cameras, have been found useful to achieve this end, being small, light and efficient, while providing high-quality images [3] for image processing (IP) algorithms that output relative orientation measurements, be it for the full targeted body in the case of centroiding techniques or for specific parts of target in the case of feature tracking. One or more cameras can be employed, providing a larger field of view than one camera alone if pointing to different directions, a close vs. open view if combining two different aperture cameras or even a depth measurement if they share field of vision, becoming stereo-cameras. For absolute attitude sensors, such as star trackers, that also are EO sensors, and gyroscopes are used, noting, however, that these states and measurements are outside of the scope of the thesis [4]. Relative distance measurements are also widely employed, with LiDARs being one of the proliferous kind of sensors, ranging from simple altimeters that measure the distance of the SC to an object in a fixed direction to providing a full 3D point cloud of a surface [5].

Several successful missions using autonomous navigation with these sensors were launched, with JAXA's Hayabusa2 sample collecting of asteroid Ryugu [6–9], NASA's OSIRIS-REX mission to Bennu with the same objective [10–13] and yet to be completed ESA's HERA mission to the binary system

Didymos [14, 15] being three examples. These missions were/are characterized by the employment of more target attitude-robust but inaccurate relative orientation centroiding techniques, and switching to higher precision but attitude-dependent feature tracking techniques when entering in close proximity to their targets for better navigation, noting that the target's attitude were/are a uploaded quantity by ground, with a given, albeit small, uncertainty.

Another autonomous navigation usage case will be ESA's RAMSES mission [16] to accompany and study Apophis during its close encounter with Earth, coming within 32.000 km of its surface and becoming the largest object to approach Earth at such distances in recorded history [17]. This situation provides a unique opportunity of taking a look into the history of the Solar System, usually requiring deep exploration of it, while also expanding the knowledge of the asteroid's shape, composition, mass, rotational states and the effects of Earth gravitational forces on those attributes [16].

But this opportunity does not come without challenges: unlike the three hallmark missions mentioned previously, Apophis will suffer gravitational torques due to its close proximity to Earth, disrupting its rotation state [18] and removing the possibility of using ground calculations to inform the SC of Apophis' attitude, forcing the estimation of the rotational states of Apophis while subject to these uncertainties. Furthermore, Apophis also presents a short axis mode complex rotation, where the instantaneous angular velocity and momentum vectors do not align, resulting in a change on angular velocity across time, and, with it, a non-constant but periodic attitude change.

The work here developed tries to answer this augmented problem, defining a solution capable of estimating the SC position and velocity during its fly-by to Apophis while simultaneously observing and correctly keeping track of the asteroid's rotational states.

1.1.1 Pose Determination

With the motivation of this thesis laid out, it is important to categorize the problem at hand, so that a literature review may be performed.

The determination of the relative position and attitude of a target, in this case Apophis, is commonly known as a pose determination problem. These problems can be further divided into two subcategories, depending on the communication between the chaser, i.e., the SC, who is performing the estimation, and the target, i.e., Apophis, the object of the estimation. Cooperative pose determination is done when targets share internal states information, i.e., relative attitude and/or own angular velocity, that they measure or estimate themselves. The second category is the pose determination of uncooperative targets, where the chaser does not receive help from the target, and has itself to measure all the relative states. Asteroids are, by nature, uncooperative, lacking both sensors and means of communication. Space debris, e.g., inoperative satellites, are also uncooperative targets that have received attention in the last years [19].

The uncooperative nature of Apophis makes it so that the estimation of its relative states must be performed by using EO sensors, such as cameras, and altimeters measurements. The main issues with this reliance on these sensors are the loss of a direct state measurement of the target's states, the sensibility of cameras to lighting and distance to the target, and the intensive process power required to turn camera images into useful measurements. Moreover, the relationship between the measurements and the states to be estimated is nonlinear, adding a layer of complexity.

The knowledge of the target is also an important differentiating point between the different problems found in the literature. When estimating the rotational states of an uncooperative target, the angular velocity might be an interesting quantity to estimate as well. However, the evolution of the angular velocity is dependent not only upon the torques that may be applied to the target, but also upon the inertia tensor of the target. In most cases, the inertia tensor of the target is unknown, resulting in more parameters to be estimated. Furthermore, the knowledge about the surface of the target may vary, with shape, size and the *a priori* information of features' location being crucial to determine which measurement methods should be employed. The absence of known features raises some challenges, namely, their initialization. Measurements by altimeters, stereo, or multiple cameras provide 3D information about a point location. However, a monocular camera alone does not, and it is reliant on the knowledge of the target's surface characteristics or the information between consecutive frames to determine the features' 3D location.

1.2 Objectives

The objective of this thesis is to develop a navigation algorithm capable of on-board real-time estimation of the relative position of the SC during the close approach phase and attitude of Apophis during the Earth's influence on its rotation, resorting to on-board low frequency and latency-affected measurements, while dealing with both state and measurement dynamics uncertainties.

To achieve both objectives of this thesis, three different questions were defined:

1. What is the combination of sensors and techniques that deliver the best SC translational state estimate and, consequently, best pointing performance of the instruments to Apophis;
2. What is the combination of sensors and techniques that deliver the best estimation of Apophis rotational state evolution during its close Earth fly-by;
3. What is the impact on the SC pointing and Apophis attitude estimation performances of using a reduced sensor suite, e.g., no altimeter, that would allow to cut the mission costs.

Each of the questions has a direct impact on the desired mission objective: the first answers to the basic need of observing Apophis during the fly-by, allowing the measurement of its characteristics and their evolution across time; the second builds upon the first, and proposes to actually estimate the evolution of one of Apophis characteristics, its rotation state; and the final tries to explore cost-saving opportunities for the mission.

1.3 State-of-the-Art

Considering the problem in question, as well as the objectives defined for this thesis, it is important to review existing solutions to similar problems, so that a new proposal may be drawn.

For this, it is important to understand what is outside of the scope of this thesis. Most of the previously mentioned measurements rest on the detection and matching of features or even the whole target in an image. This kind of problem falls into the image processing field, and several solutions were already developed, notably in [20–23]. Due to the unrelated nature of the field and already present solutions, these algorithms are outside of the scope of this thesis.

The focus will be, instead, on the estimation of the desired states themselves. The estimation of a relative attitude and position of an uncooperative target can be achieved with recourse to different tools. The most prominent of these tools are algebraic estimation, dynamic estimation and, more recently, estimation based on deep learning models.

1.3.1 Literature Review

With the objectives and focus of this thesis defined, it is possible to review the current solutions to problems that fall onto the same category. This section will go over several cases where the previously mentioned tools for uncooperative pose estimation are employed.

Starting with algebraic estimation methods, the objective of these techniques is the minimization of an error function that describes the expected output at that instant in respect to the relative distances and attitude of the target. For monocular camera measurements, this is achieved by solving a perspective-n-point problem (PnP) [24], and methods to solve these problems are discussed and compared in [25]. While some of these solutions present interesting results, three downsides are common to them. Firstly, their pose estimation is based only on the current measurements and, therefore, are sensible to noisy measurements. A solution to this issue can be the integration of these methods into a larger estimator, and using them as measurements instead of final estimates, with this application being found in [26]. Secondly, these algorithms assume that an 3D model with the interest points already exists, which is not the case for Apophis. A possible bypass to this problem can be the offline reconstruction of the surface based of a set of images [27], however, this process is computationally expensive and requires previous observations of the body. Thirdly, some of the algorithms solve the minimization problem iteratively [28], adding computational load.

Dynamic estimators, or filters, fuse the knowledge of the dynamics of a system with the measurements it receives. This approach to estimation allows the filtering of sensor noise that may exist in the sensors, reducing their effects when compared to the results of the algebraic estimation methods alone. However, this improvement comes at the cost of a more detailed knowledge of the system, requiring the description of the systems' dynamics through a set of differential equations. The Kalman filter (KF) [29] and its variants, namely the extended Kalman filter (EKF) [30], are commonly used for the estimation of states in linear and nonlinear systems, respectively. The KF is the optimal filter under the assumptions that the system is linear and that the system's disturbances, both in the dynamics and measurements, are white, Gaussian, zero-mean, and uncorrelated noises. The EKF tries to capture the performance of the KF by linearizing the nonlinear system at its own estimation point, but it cannot offer convergence guarantees, unlike the KF, and its performance is, at most, near-optimal. Particle filters also exist, bypassing the probability density function limitation that the Kalman filters have and, therefore, being suitable to address nonlinear systems [31]. This is achieved by approximating the probability density function with a given number of sample points. However, these filters come with their downsides, requiring extensive computational power to properly represent the system's dynamics, with the necessary power increasing significantly as the dimensions of the system increase, something denoted as the curse of dimensionality. Furthermore, they may suffer from unbalanced samples, requiring resampling to properly propagate the probability density function as it is used. Unscented Kalman filters [32] try to bring the better of both approaches by mixing them. This is done by strategically sampling the probability density function, assuming an initial Gaussian distribution, and then reconstructing the final probability density function, that has passed through a nonlinear function, as a Gaussian distribution. In spite of its goals, however, the performance of the unscented Kalman filter can be similar or worse than that of an EKF, while suffering from the dimensionality problem that particle filters also suffer from, but in an accentuated scale [33].

A significant number of solutions to variations of the pose estimation problem using filters exist. Hayabusa2's close proximity operations relied on a detailed map of Ryugu [7] and its rotational states. Its navigation system for the touch-down used an EKF fed with measurements from one monocular camera to track one artificial feature, providing the relative orientation to a fixed and known spot on Ryugu's surface, and four rangefinders pointing at different directions, measuring the distance and inclination to Ryugu's surface. However, from [8, 9], it is not clear that the mapping of Ryugu's surface, and its rotational states, done in more detail during an earlier stage of the mission from an hover position, were performed in conjunction with the SC's pose estimation or separately. However, [9] mentions radio tracking measurements, indicating that the SC's navigation system uses other measurements to determine its position in this phase. OSIRIS-REx reports [11–13] state that the touch-down of the SC to Bennu's surface is done using two independent navigation strategies: one using scanning LiDAR measurements and other using previously mapped feature tracking with a monocular camera. The initial mapping of Bennu's surface is performed in an earlier stage, and this characterization is done using the previously mentioned instruments, while receiving radio tracking information to estimate the SC's position independently [13].

Moving to the realm of satellite servicing, [34] provides a solution to the relative pose estimation problem, as an exogenous Kalman filter is employed to filter, as measurements, PnP states estimates obtained from feature tracking measurements by a stereo camera. This solution resorts to a filter cascade, including an EKF and a KF, to achieve convergence guarantees, something that an EKF alone does not provide. Moreover, the proposed solution also estimates the inertia parameters of the target, a characteristic that is usually desired due to its uncertainty and influence over the rotational dynamics of the target. However, it requires previous knowledge of the features positions, which is a prohibitive condition for this thesis' tasks, and does not consider large rotational uncertainties regarding external torques. Still using stereo cameras measurements, [35] develops an iterative extended Kalman filter to estimate the pose of an unknown target, alongside its inertia parameters estimation, while resorting directly to the feature tracking measurements, bypassing algebraic estimation techniques. This solution also employs a pseudo-measurement, that assumes that the target's angular acceleration, and therefore torques, are known up to a zero-mean, white, Gaussian noise. Furthermore, this solution also estimates the tracked features' positions, since they were previously unknown.

Monocular-based measurements are more complex to use in pose determination, since they only convey 2D information to a point, instead of the full 3D position. A survey on the application of estimators resorting to these measurements can be found in [36], for both known and partially known targets. For a previously unknown target, the solution developed in [26] offers the possibility to both estimate the relative pose as well as reconstruct the target's shape. This result is achieved by splitting the estimation in three parts: Firstly, the angular velocity is estimated by solving an algebraic optimization problem based upon the optical flow measurement equation. Secondly, the relative position and translational velocity are estimated with the same optical flow measurements, and angular velocity estimation, in an EKF. Thirdly, a second EKF can be be implemented, with the target's relative position, velocity and attitude, and the features' positions being estimated here. The angular velocity previously estimated is used to propagate the target's attitude kinematics, with the initially estimated linear position and velocity being used as measurements, in conjunction with the feature tracking measurements and a single depth measurement provided by a LiDAR. The features are initialized and deleted in this filter, using the relative direction of the feature, alongside the depth measurement, with a given uncertainty. Lastly, a reconstruction of the target's shape can be made offline using the Structure from Motion method [27]. This solution assumes that the angular velocity of the target can be directly estimated from the optical flow measurements and thus, bypasses its dynamics. This assumption, while solving most of the rotational dynamics uncertainties, leads to a sub-optimal angular velocity estimation in the presence of noise.

Finally, a note should be made regarding the employment of deep learning methods for pose estimation. Deep learning methods rely on deep neural networks and/or convolutional neural networks for the pose determination of the target, with the possibility of incorporating more traditional steps, such as PnP solvers. These networks are defined by setting their architecture and then training them, i.e., iteratively minimizing their output error in respect to their intrinsic parameters. This training carries two large issues: firstly, a large database of inputs must already exist to train the network. Given the nature of space missions, this datasets are sparse and expensive, lowering the reliability of the trained networks, even when using synthetic data sets to mitigate this issue [37]. Secondly, due to their opaque inner workings, deep learning methods are inherently hard to validate, a crucial component in the development of space applications [37]. Nevertheless, [37] set out to access the capabilities of these methods to estimate the relative pose of a satellite, showing that there are promising results with deep learning methods employing PnP solvers. After analysing three strategies for CNN based pose estimation, [36] arrived at the same conclusion.

1.4 Contributions

The goals of this thesis were defined to develop and test a pose estimation algorithm subject to significant dynamic uncertainties alongside a partially known target, resorting to a relatively small and simple set of measurements. The contribution of this thesis is the development of a filter capable of estimating the pose of a target, and the estimation of the position of features on its surface, subject to:

- Strong dynamic uncertainties on the target's rotation and SC's translation;
- Significant measurement uncertainties;
- Target's surface model errors and no known features;
- No optical flow measurements.

Furthermore, the proposed solution is compared to a simplified version, where the features' positions are known, alongside one that does not rely on features, allowing a baseline in which to compare the proposed algorithm. The removal of depth measurements also contribute to the value of this work, resulting in the evaluation of the importance of this kind of measurements when resorting to a monocular camera.

1.5 Organization of the Thesis

This thesis is organized as follows. In Chapter 2, the generic dynamics model of the system are showcased, followed by an overview of the measurement sensors available and filtering algorithms. In Chapter 3, the problem at hand is formally stated, presenting the quantities to estimate, the restrictions imposed on the solution and assumptions. In Chapter 4, the solution to this work's problem is proposed, detailing the inner workings of each subsystem. Chapter 5 presents the environment parameters necessary for the evaluation of the proposed solution, followed by the results of said filters after simulating the mission. In Chapter 6, the main conclusions of this thesis are presented, alongside future work.

Chapter 2

Background

2.1 Notation

The notation used in this thesis is the following one:

- reference frames, r.f., will be denoted with calligraphic upper case, e.g, $\mathcal{I}$;
- matrices with bold uppercase letters, e.g., $\mathbf{M}$,
- vectors with lowercase bold letters, e.g, $\mathbf{v}$,
- quantities expressed in a r.f. with superscripted r.f. followed by the quantity, e.g., ${}^{\mathcal{I}}\mathbf{v}$;
- variable scalars and indexes with lowercase letters, e.g., b and n, respectively;
- constant scalars follow the typical nomenclature in the literature, being properly identified and defined.

2.2 Attitude Representation and Kinematics

This section will showcase different forms of attitude representation, each one with their own properties, alongside their strengths and weaknesses. The relationship between the attitude representations here contemplated: quaternions, Euler angles, and transformation matrices, can be found in [38].

2.2.1 Transformation Matrix

A transformation matrix is a matrix that expresses the rotation between two different right-handed r.f.. Consider right-handed reference frames $\{\mathcal{A}\}$ and $\{\mathcal{B}\}$, that rotate in relation to each other, with basis vectors $\{\mathbf{a}_1, \mathbf{a}_2, \mathbf{a}_3\} \in \mathrm{R}^3$ and $\{\mathbf{b}_1, \mathbf{b}_2, \mathbf{b}_3\} \in \mathrm{R}^3$, respectively. The matrix that relates the basis vectors between two reference frames is the rotation matrix ${}^{\mathcal{B}}_{\mathcal{A}}\mathbf{R} \in \mathbb{R}^{3\times3}$, following

$$\begin{bmatrix} \mathbf{b}_1 & \mathbf{b}_1 & \mathbf{b}_3 \end{bmatrix} = {}^{\mathcal{B}}_{\mathcal{A}}\mathbf{R} \begin{bmatrix} \mathbf{a}_1 & \mathbf{a}_1 & \mathbf{a}_3 \end{bmatrix} \tag{2.1}$$

and can be calculated by

$$^{\mathcal{B}}_{\mathcal{A}}\mathbf{R} = \begin{bmatrix}\mathbf{b}_1^{\mathsf{T}} & \mathbf{b}_2^{\mathsf{T}} & \mathbf{b}_3^{\mathsf{T}}\end{bmatrix}^{\mathsf{T}} \begin{bmatrix}\mathbf{a}_1 & \mathbf{a}_2 & \mathbf{a}_3\end{bmatrix}. \tag{2.2}$$

Transformation matrices have a set of properties that caracterize them, as being orthogonal, leading to (2.3), and their determinant being equal to 1, since they preserve the scalar product of vectors and both reference frames are right-handed, and the inverse satisfies

$$^{\mathcal{B}}_{\mathcal{A}}\mathbf{R}^{-1} = {}^{\mathcal{B}}_{\mathcal{A}}\mathbf{R}^{\mathsf{T}}, \tag{2.3}$$

resulting in 6 constraints imposed upon any transformation matrix.

This representation has the advantage that for any pair of r.f. only one transformation matrix represents their relative attitude, and only one attitude is represented by a given rotation matrix. Another point in favour of this representation is its simplicity to represent the attitude between multiple r.f.. Consider a new right-handed r.f. $\{\mathcal{C}\}$ to which only the relation between itself and $\{\mathcal{B}\}$ is given. The relation between $\{\mathcal{A}\}$ and $\{\mathcal{C}\}$ can be obtained by

$$^{\mathcal{C}}_{\mathcal{A}}\mathbf{R} = {}^{\mathcal{C}}_{\mathcal{B}}\mathbf{R}{}^{\mathcal{B}}_{\mathcal{A}}\mathbf{R}, \tag{2.4}$$

which is called the composition rule. Its kinematics are, linear in respect to its elements, [39]

$$^{\mathcal{B}}_{\mathcal{A}}\dot{\mathbf{R}} = {}^{\mathcal{B}}_{\mathcal{A}}\mathbf{R}[{}^{\mathcal{B}}\omega]_{\times}, \tag{2.5}$$

where ${}^{\mathcal{B}}\boldsymbol{\omega}$ is the rotation velocity of $\{\mathcal{B}\}$ in relation to $\{\mathcal{A}\}$ and expressed in $\{\mathcal{B}\}$ and $[\mathbf{p}]_{\times}$ is a skew matrix such that

$$[\mathbf{p}]_{\times}\mathbf{v} = \mathbf{p} \times \mathbf{v}. \tag{2.6}$$

However, a downside to this representation is that it has 9 elements to only 3 degrees of freedom, which can take a toll on operations dependent on the size of the state while not adding information, and the error between each variable is dependent on the others by constraints, making the interpretation of such errors more complicated to evaluate.

2.2.2 Euler Angles

The attitude between two reference frames can be represented by three angles, ϕ, θ, and ψ, since in a 3D rotation there are 3 degrees of freedom. These angles define a series of rotations about a given axis, requiring the definition of which axis are the rotations to be taken. In this thesis only the classic sequence, 3-1-3, was employed to describe the rotation of Apophis.

The transformation matrices that describe the rotation about the three main axes are

$$
{}_1\mathbf{R}(\alpha) = \begin{bmatrix} \cos(\alpha) & \sin(\alpha) & 0 \\ -\sin(\alpha) & \cos(\alpha) & 0 \\ 0 & 0 & 1 \end{bmatrix}, \quad {}_2\mathbf{R}(\alpha) = \begin{bmatrix} \cos(\alpha) & 0 & \sin(\alpha) \\ 0 & 1 & 0 \\ -\sin(\alpha) & 0 & \cos(\alpha) \end{bmatrix}, \tag{2.7}
$$

$$
{}_3\mathbf{R}(\alpha) = \begin{bmatrix} 1 & 0 & 0 \\ 0 & \cos(\alpha) & \sin(\alpha) \\ 0 & -\sin(\alpha) & \cos(\alpha) \end{bmatrix}, \tag{2.8}
$$

and, therefore, the full rotation matrix for the classical representation is,

$$
\mathbf{R}(\phi, \theta, \psi) = {}_3\mathbf{R}(\psi){}_1\mathbf{R}(\theta){}_3\mathbf{R}(\phi), \tag{2.9}
$$

where ϕ is the precession, θ the nutation and ψ the spin angles of the r.f..

Although this representation is minimal, in the sense that it only has 3 variables to represent 3 degrees of freedom, a large number of issues arise, such as indetermination problems when $\theta = 0$, discontinuities in the conversion between rotation matrices and Euler angles, no readily available composition rule, and the kinematics of the attitude require the evaluation of trigonometric functions [38].

2.2.3 Quaternions

The quaternions are the final representation form exposed in this section, and was the choice to implement in the filter.

There are different conventions on to how transformations are represented with quaternions which lead to different relationships, so it is important to clarify the choice made in this thesis. The quaternion convention chosen is the Hamiltonian convention, where the quaternion is right-handed and a passive rotation operation, just as the transformation matrices previously described [39]. Moreover, a general quaternion has four parameters and can be viewed as pair scalar-vector

$$
\mathbf{q} = \begin{bmatrix} q_w & \mathbf{q_v}^\mathsf{T} \end{bmatrix}^\mathsf{T} = \begin{bmatrix} q_w & q_x & q_y & q_z \end{bmatrix}^\mathsf{T}, \tag{2.10}
$$

with an arbitrary 3D vector $\mathbf{x}$ being expressed in $\mathbf{q_v}$ and setting $\mathbf{q}_w$ to zero. The following properties of the quaternion are only valid with the chosen convention.

The product between two quaternions is generally non-commutative and, using $\mathbf{q_v}$ and q_w, can be defined as

$$
\mathbf{p} \odot \mathbf{q} = \begin{bmatrix} p_w q_w - \mathbf{p_v}^\mathsf{T} \mathbf{q_v} \\ p_w \mathbf{q_v} + q_w \mathbf{p_v} + \mathbf{p_v} \times \mathbf{q_v} \end{bmatrix}. \tag{2.11}
$$

The quaternions that can express a transformation between two r.f. have one constraint related to their their module, that must be one,

$$||\mathbf{q}|| = \sqrt{q_w^2 + q_x^2 + q_y^2 + q_z^2} = 1, \tag{2.12}$$

and these quaternions can be understood as

$$\mathbf{q}\{\boldsymbol{\theta}\} = \begin{bmatrix} \cos(||\boldsymbol{\theta}||/2) \\ \boldsymbol{\theta}/||\boldsymbol{\theta}|| \sin(||\boldsymbol{\theta}||/2) \end{bmatrix}, \tag{2.13}$$

where $\boldsymbol{\theta}/||\boldsymbol{\theta}||$ is the orientation of the rotation and $||\boldsymbol{\theta}||$ is the rotation magnitude.

The change in r.f. of a vector $\mathbf{v}$ from $\{\mathcal{A}\}$ to $\{\mathcal{B}\}$ can be written as

$$^{\mathcal{B}}\mathbf{v} = {}^{\mathcal{B}}_{\mathcal{A}}\mathbf{q} \odot {}^{\mathcal{A}}\mathbf{v} \odot {}^{\mathcal{B}}_{\mathcal{A}}\mathbf{q}^*, \tag{2.14}$$

where $\mathbf{q}^*$ is the conjugate of $\mathbf{q}$ and is defined by

$$\mathbf{q}^* = \begin{bmatrix} q_w & -\mathbf{q_v}^\mathsf{T} \end{bmatrix}^\mathsf{T}. \tag{2.15}$$

With this, one can compare the rotation operation of a generic vector $\mathbf{v}$ by a quaternion and by a matrix,

$${}^{\mathcal{B}}_{\mathcal{A}}\mathbf{R}^{\mathcal{B}}\mathbf{v} = {}^{\mathcal{B}}_{\mathcal{A}}\mathbf{q} \odot {}^{\mathcal{A}}\mathbf{v} \odot {}^{\mathcal{B}}_{\mathcal{A}}\mathbf{q}^*, \tag{2.16}$$

and, henceforward, for the sake of conciseness, rotation operations will be represented as if a rotation matrix were being used, even if the actual operation is done with quaternions, unless a specific development of (2.14) is desired.

Quaternions allow easy composition of transformations, like their matrices counterparts,

$${}^{\mathcal{C}}_{\mathcal{A}}\mathbf{q} = {}^{\mathcal{C}}_{\mathcal{B}}\mathbf{q} \odot {}^{\mathcal{B}}_{\mathcal{A}}\mathbf{q}. \tag{2.17}$$

Regarding the kinematics of the attitude, consider the attitude quaternion ${}^{\mathcal{A}}_{\mathcal{B}}\mathbf{q}$ and the angular velocity of $\{\mathcal{B}\}$ in relation to $\{\mathcal{A}\}$ expressed in $\{\mathcal{B}\}$, ${}^{\mathcal{B}}\boldsymbol{\omega}_{\mathcal{B}/\mathcal{A}}$. The time derivative of the attitude quaternion is [39]

$${}^{\mathcal{A}}_{\mathcal{B}}\dot{\mathbf{q}} = \frac{1}{2}{}^{\mathcal{A}}_{\mathcal{B}}\mathbf{q} \odot {}^{\mathcal{B}}\boldsymbol{\omega}_{\mathcal{B}/\mathcal{A}}. \tag{2.18}$$

This representation is not minimal, since there are 4 variables for a 3 degree of freedom system, leading to the same issues discussed on the transformation matrix representation, albeit only one restriction must now be followed in this case. It also loses accuracy when $\theta \longrightarrow \pi$ and there are two quaternions that represent the same attitude, $\mathbf{q}\{\boldsymbol{\theta}\}$ and $\mathbf{q}\{-\boldsymbol{\theta}\}$. However, the kinematics of the attitude with this representation are linear and each variable can be made continuous, as opposed to the ones while using Euler angles, while allowing a more efficient composition than that of the rotation matrices [40].

2.3 Orbital Mechanics

In this thesis, all bodies are assumed to be rigid, with the implication that all forces applied to them can be represented by a resultant force acting on their centre-of-mass and a resultant torque upon it. For this reason, the total motion of a body within its environment can be decomposed into two: the translation movement, with forces acting on the centre-of-mass of the body as if it is a point-mass, and a rotation around it, governed by the torques applied to the body and its moments of inertia, that characterise the different distributions of mass across the body.

The next sections aim to give a brief exposition of the environment the SC will operate on, mentioning the reference frames used and going through the basics of the translation and rotation dynamics as considered above.

2.3.1 Reference Frames

To properly apply Newton's second law, it is important to define a inertial frame, $\mathcal{I}$. Since in this thesis the Sun is considered, due to its non negligible influence on both the SC and Apophis's orbits, the inertial r.f. has its origin in the Solar System barycentre and orientation defined the same way as the J2000 inertial reference frame, where the z axis has the orientation of the mean north pole, x the direction of the mean Vernal equinox, both in the epoch J2000.0, and y completes the right-handed r.f. [41]. However, this reference frame is not ideal to represent the movement of the Apophis and the SC, due to the large disparities between the distance of both objects to the origin (Sun) and their translation in this r.f., which can cause numerical issues. For this reason, a new reference frame called Centred Inertial $\{\mathcal{CI}\}$, will be employed in the filter, with its centre on the the Apophis's centre-of-mass at all times and same orientation as $\{\mathcal{I}\}$, or, in other words, a point position given in $\{\mathcal{CI}\}$ is the same as the relative position of a point in respect to the Apophis's centre-of-mass in $\{\mathcal{I}\}$. An important property of $\{\mathcal{CI}\}$ is that it does not rotate in relation to $\{\mathcal{I}\}$, meaning that

$$ {}^{\mathcal{CI}}_{\mathcal{I}}\dot{\mathbf{R}} = \mathbf{0}. \tag{2.19} $$

Beyond the inertial reference frame, there are other three main r.f. relevant to discuss: the Apophis's r.f. $\{\mathcal{AP}\}$, the SC's r.f. $\{\mathcal{SC}\}$, and the camera's r.f, $\{\mathcal{CA}\}$, with each of them playing a different role regarding the characterisation of the system.

The Apophis's r.f. $\{\mathcal{AP}\}$ is a reference frame centred on the centre-of-mass of the Apophis and orientation coinciding with the body's principal inertia axis at all times, therefore rotating in $\{\mathcal{CI}\}$ given that the body has angular velocity, and in which the moment of inertia is assumed to be constant, which one can exploit to express the rotational dynamics as done in Section 2.3.3.

The SC's r.f. $\{\mathcal{SC}\}$ has its origin in the centre-of-mass of the SC, its orientation fixed to the body frame such that its z axis is aligned with the constant laser altimeter direction.

Finally, the camera's r.f. $\{\mathcal{CA}\}$ has its origin on the camera and is oriented so that its z axis coincides with with the camera's pointing direction and the x and y are oriented to be align with the camera's plane axis. With this said, for practical purposes the origin of $\{\mathcal{CA}\}$ will be considered as the centre-of-mass of the SC.

Ideally $\{\mathcal{SC}\}$ and $\{\mathcal{CA}\}$ are coincident, however it may happen that during the mission a pointing error may occur, albeit small, and therefore the distinction should be made.

A final r.f. $\{\mathcal{RAC}\}$ will be used during the analysis of the estimation error, with its origin in the centre-of-mass of the SC and Radial-Along-Cross track orientation, where the non-normalized basis vectors, in relation to $\{\mathcal{I}\}$, are depicted in Fig. A.1, and can be formally describes as

$$\begin{cases} \mathbf{r} = {}^{\mathcal{I}}\mathbf{x}_{SC} - {}^{\mathcal{I}}\mathbf{x}_{AP}, & (2.20a) \\ \mathbf{c} = \mathbf{r} \times {}^{\mathcal{I}}\mathbf{v}_{SC}, & (2.20b) \\ \mathbf{a} = \mathbf{c} \times \mathbf{r}, & (2.20c) \end{cases}$$

where $\mathbf{x}_{SC}$ is the position of the SC, $\mathbf{x}_{AP}$ the position of the Apophis, and $\mathbf{v}_{SC}$ the velocity of the SC.

The relationship between the position of a point $\mathbf{p}$ in two generic reference frames $\{\mathcal{A}\}$ and $\{\mathcal{B}\}$ is

$$^{\mathcal{B}}\mathbf{p} = {}^{\mathcal{B}}_{\mathcal{A}}\mathbf{R}({}^{\mathcal{A}}\mathbf{p} - {}^{\mathcal{A}}\mathbf{o}_{\mathcal{B}}), \tag{2.21}$$

where ${}^{\mathcal{A}}\mathbf{o}_{\mathcal{B}}$ is the origin of $\{\mathcal{B}\}$ in $\{\mathcal{A}\}$.

2.3.2 Translational Mechanics

In missions, spacecrafts are subject to several forces, e.g. gravitational forces, atmospheric drag and radiation pressure. In this thesis, only central gravitational forces and the solar radiation pressure were considered, and this subsection is dedicated to present their characteristics.

Consider two bodies with masses m_1 and m_2, and positions ${}^{\mathcal{I}}\mathbf{x_1}$ and ${}^{\mathcal{I}}\mathbf{x_2}$, respectively. The force on body 2 due to the gravity of body 1, $\mathbf{f}_{2/1}$, is described by Newton's law of gravitation and, with Newton's third law, one knows that the force on body 1, $\mathbf{f}_{1/2}$, has the same magnitude and opposite direction

$$\begin{aligned} {}^{\mathcal{I}}\mathbf{f}_{2/1} &= - Gm_1m_2\frac{{}^{\mathcal{I}}\mathbf{x_2} - {}^{\mathcal{I}}\mathbf{x_1}}{||{}^{\mathcal{I}}\mathbf{x_2} - {}^{\mathcal{I}}\mathbf{x_1}||^3}, \\ {}^{\mathcal{I}}\mathbf{f}_{1/2} &= + Gm_1m_2\frac{{}^{\mathcal{I}}\mathbf{x_2} - {}^{\mathcal{I}}\mathbf{x_1}}{||{}^{\mathcal{I}}\mathbf{x_2} - {}^{\mathcal{I}}\mathbf{x_1}||^3}. \end{aligned} \tag{2.22}$$

where $G = 6.674 \cdot 10^{-11}$Nm^{2}kg^{-2} is the universal gravitational constant.

With Newton's second law one can find the respective acceleration of the bodies, henceforward called central acceleration,

$$\begin{aligned} {}^{\mathcal{I}}\mathbf{a}_{2/1} &= {}^{\mathcal{I}}\mathbf{f}_{2/1}/m_2 = -Gm_1\frac{{}^{\mathcal{I}}\mathbf{x_2} - {}^{\mathcal{I}}\mathbf{x_1}}{||{}^{\mathcal{I}}\mathbf{x_2} - {}^{\mathcal{I}}\mathbf{x_1}||^3}, \\ {}^{\mathcal{I}}\mathbf{a}_{1/2} &= {}^{\mathcal{I}}\mathbf{f}_{1/2}/m_1 = +Gm_2\frac{{}^{\mathcal{I}}\mathbf{x_2} - {}^{\mathcal{I}}\mathbf{x_1}}{||{}^{\mathcal{I}}\mathbf{x_2} - {}^{\mathcal{I}}\mathbf{x_1}||^3}, \end{aligned} \tag{2.23}$$

where the term $\mu_n : Gm_n$ describes the gravitational constant of a given body n. Notice that, if one body's mass is much larger than the other's, $m_1 >> m_2$, then the effects on body 1 due to the gravity of

2 can be neglected. For our case, since the mass of the SC is much smaller than the mass of Apophis, the dynamics of Apophis are not affected by the presence of the SC.

Another force to be considered for the SC's dynamics is the solar radiation pressure. This force is caused by the exchange of momentum between the photons emitted by the Sun and the satellite's surface. Therefore, the force will depend on the satellite's geometric characteristics, and its formula is, assuming a flat surface [42],

$$\mathbf{f}_{SRP} = Ac_r\frac{p_0}{c}r_0^2\frac{{}^{\mathcal{I}}\mathbf{x_1} - {}^{\mathcal{I}}\mathbf{x_S}}{||{}^{\mathcal{I}}\mathbf{x_1} - {}^{\mathcal{I}}\mathbf{x_2}||^3}, \tag{2.24}$$

where A is the surface area exposed to the light, $p_0 = 1367$ Wm^{-2} is the solar flux at r_0, $c = 299.792 \times 10^6$ ms^{-1} is the speed of light in a vacuum, $r_0 = 149.598 \times 10^6$ km is the Sun-Earth mean distance, and c_r accounts for the reflective nature of the SC's surface. The variable $\rho_S : Ac_r\frac{p_0}{c}r_0^2m$ will be used to encapsulate all this constants and, considering that the area, reflection characteristics and mass of the SC do not change, is constant. It is useful to note that the force applied to the SC due to radiation pressure has the same model as the gravitational force where $\mu = -\rho$.

Finally, the relative acceleration of a point in respect to another point in an inertial reference frame can be obtained by differentiating two times the position both in the inertial r.f. and in the relative frame. Consider the r.f. $\{\mathcal{I}\}$, the r.f. $\{\mathcal{CI}\}$, and a point $\mathbf{x}$. Recalling that both r.f. do not rotate over time, the acceleration of $\mathbf{x}$ in $\{\mathcal{CI}\}$ is

$$({}^{\mathcal{C}\ddot{\mathcal{I}}}\mathbf{x}) = ({}^{\mathcal{I}}\mathbf{x} - {}^{\ddot{\mathcal{I}}}\mathbf{x}_{AP}) \Leftrightarrow ({}^{\mathcal{CI}}\ddot{\mathbf{x}}) = {}^{\mathcal{I}}\ddot{\mathbf{x}} - {}^{\mathcal{I}}\ddot{\mathbf{x}}_{AP}. \tag{2.25}$$

2.3.3 Rotational Dynamics

A key aspect of this thesis is the fact that the target, Apophis, will be rotating and suffer changes to its angular momentum and with it important measurements will be affected, which turns the rotational dynamics of Apophis a relevant topic to discuss. For this reason, this section introduces the basic concepts of the rotational dynamics, noting that its results are dependent upon the attitude conventions chosen.

Starting with the rotational dynamics themselves, the assumption that the target is a rigid body implies that the distance of two physical points in the body does not change across time and, therefore, that the distribution of mass of the body does not change.

The angular momentum of a rigid body $\mathbf{h}$ relative to a point $\mathbf{o}$ is

$$\mathbf{h} = \int_C (\mathbf{x} - \mathbf{o}) \times \mathbf{v}\mathrm{d}m, \tag{2.26}$$

where C is the body's volume. Given that $\mathbf{o}$ is the centre-of-mass of the body and no torques are applied, it is constant in an inertial r.f..

Furthermore, the angular momentum in relation to the centre-of-mass of the body is related to its angular velocity by the inertia tensor $\mathbf{J}$,

$${}^{\mathcal{A}}\mathbf{h} = {}^{\mathcal{A}}\mathbf{J}{}^{\mathcal{A}}\boldsymbol{\omega}, \tag{2.27}$$

where the terms of $\mathbf{J}$ for axis pair ij can be calculated as

$$J_{ij} = \int_C \mathbf{x}^\mathsf{T}\mathbf{x}\delta_{ij} - r_i r_j \mathrm{d}m, \tag{2.28}$$

where δ_{ij} being the Kronecker delta. One interesting property of $\mathbf{J}$ is that, if the r.f. it is expressed is aligned with the principal axis of the body, $\mathbf{J}$ is a positive definite diagonal matrix, where the axis of the largest moment of inertia is the major axis, and smallest the minor axis. Consider a r.f. $\{\mathcal{B}\}$ aligned with the principal axis of the body at all times.

The rotational energy of a body is also an important characteristic of its motion, and it is related to the angular velocity and inertia tensor by

$$E = \frac{1}{2}\boldsymbol{\omega}^\mathsf{T}\mathbf{J}\boldsymbol{\omega}. \tag{2.29}$$

With these quantities presented, one can express the time derivative of the angular velocity of r.f. $\{\mathcal{B}\}$ in respect to $\{\mathcal{I}\}$, ${}^{\mathcal{B}}\dot{\omega}$, in function of the torques acting on the body $\boldsymbol{\tau}$, its inertia tensor ${}^{\mathcal{B}}\mathbf{J}$ and own angular velocity ${}^{\mathcal{B}}\omega$ with the Euler equation [43],

$${}^{\mathcal{B}}\dot{\boldsymbol{\omega}} = {}^{\mathcal{B}}\mathbf{J}^{-1}({}^{\mathcal{B}}\boldsymbol{\tau} - {}^{\mathcal{B}}\boldsymbol{\omega} \times {}^{\mathcal{B}}\mathbf{J}{}^{\mathcal{B}}\boldsymbol{\omega}). \tag{2.30}$$

An important observation to make (2.30) is that, unlike in the translational dynamics, the (angular) velocity can have a non-zero derivative when no torque is exerted on the system, provided that ${}^{\mathcal{B}}\boldsymbol{\omega} \times {}^{\mathcal{B}}\mathbf{J}{}^{\mathcal{B}}\boldsymbol{\omega} \neq \mathbf{0}$, which happens when ${}^{\mathcal{B}}\boldsymbol{\omega}$ is not align with a principal inertia axis, and this phenomena is called a complex rotation. These rotations are characterized by both periodic circular motion of the angular velocity around the angular momentum in an inertial r.f. and an a periodic attitude motion around the angular momentum, and can be fully defined by initial precession, ϕ_0, and spin, ψ_0, angles, average precession and spin periods P_ϕ and P_ψ, respectively, and the ratio between angular energy and minimum angular energy E/E_0, i.e., the angular energy that the body would have if rotating around its major axis with the same angular momentum [44]. The relation between this quantities and the desired states, attitude and angular velocity, are explored in [45].

Moreover, torques may also be applied to the body. Although the gravitational force applied to a body is most of the times assumed constant through the body, this is not true, since the distance to the source of the gravitational pull is, in most cases, different, and if the principal axis of inertia of the body are not align with the gravitational force at the centre-of-mass, torques are generated. In particular, only when the major axis is aligned with the gravitational pull is the configuration stable. This, coupled with the fact that in space there are no other significant forces to counteract this torque, this effect is important to consider.

The derivations of the torque on a body due to gravitational forces of another are made in [46] up to the fourth order. However, only terms up to the second order should influence the rotation of Apophis [18],

$$\begin{cases} \tau_x = \dfrac{3\mu}{r^3} e_x e_z (J_{zz} - J_{yy}), & \text{(2.31a)} \\ \tau_y = \dfrac{3\mu}{r^3} e_x e_z (J_{xx} - J_{zz}), & \text{(2.31b)} \\ \tau_z = \dfrac{3\mu}{r^3} e_x e_z (J_{yy} - J_{xx}), & \text{(2.31c)} \end{cases}$$

where r is the distance between the centre-of-mass of the bodies and $\mathbf{e}^{\mathsf{T}} = [e_x \; e_y \; e_z]$ is the orientation of the affected body in relation to the perturbing body in $\{\mathcal{B}\}$.

With the major rotational quantities and relationships explained, there is one final note to make: the variation of angular velocity (2.30) where the torques are caused due to the gravitational pull does not depend on magnitude of its inertia tensor, but instead on the relationship between the inertia moments of its main axis. Therefore, any inertia tensor that satisfy those relationships can be a suitable tensor to employ in the rotational dynamic, provided that the assumptions made are valid. In this thesis, the z axis of $\{\mathcal{AP}\}$ was chosen to be aligned with the major inertial axis of the body, and J_{yy} and J_{xx} are normalized to J_{zz}, resulting in the inertia tensor

$$^{\mathcal{AP}}\mathbf{J} = \begin{bmatrix} J_{xx}/J_{zz} & 0 & 0 \\ 0 & J_{yy}/J_{zz} & 0 \\ 0 & 0 & 1 \end{bmatrix}. \tag{2.32}$$

2.4 Measurement Sensors

An integral part of any system is its output, or measurements, obtained with sensors. These measurements inform the SC of its state, allowing closed-loop control and estimation techniques, alongside the determination of the current flight phase, crucial for the fulfilment of the objectives of each phase. However, these measurements are not perfect, being affected by noise, suffering from latency or introducing different errors into raw estimates. Moreover, the sensors might not give direct measurements of the desired states, as it is the case for measuring the relative position of points on a body, when the desired measurement is the attitude of that body. For this reason, these measurements should be filtered by an observer.

Attitude sensors can be either absolute or relative: the first refer to the attitude relative to an inertial r.f., while the second its the attitude relative to two generic non inertial frames. An example of a type of absolute attitude sensor are the star trackers, that measure the attitude of the SC relative to inertial r.f. by identifying star constellations [4]. Since uncooperative targets, as is the case of Apophis, do not provide active information about their states, EO sensors are currently the main technology for pose estimation, with LiDAR, monocular and stereo cameras being part of this selection [26]. With this said, the outputs of these sensors must be further processed in order to obtain useful information, as feature's positions, adding a layer of complexity that if filled by image processing (IP) algorithms and in this thesis addressed in conjunction to the "physical" sensors.

Regarding position measurements, these can also be absolute or relative, with the former relating the position of a point relative to an inertial r.f., while the latter relating the relative position of two generic points. The relative position of the SC to Apophis will be measured by the same sensors that were described in the pose measurement, where monocular cameras, alongside the attitude of the SC, can provide along and cross-track position measurements and LiDAR providing radial measurements during the trajectory.

This section has the objective to address the main characteristics of this sensors, reviewing their utilization, outputs and their models.

2.4.1 LiDAR

Light Detection And Ranging (LiDAR), also known as LiDAR, is an active sensor that measures the range to one or more points of the surface of a target. Its basic premise is straightforward, using light, normally a laser, to illuminate the target and measure the time it takes for the emitted signal to return to the sensor, with this time, t, being related to the range, r, of the targeted point by

$$r = \frac{ct}{2},$$

where c is the speed of light in vacuum [47].

Three main types of LiDAR systems are identified in [47], where scanning systems and detector arrays are the main focus, with spatial light modulators being still in development and, therefore, not expanded upon. Scanning systems consist of using a single narrow laser beam to sweep the sensor's field of view while a single, or small number of, detector receives the reflected light. These systems contain moving parts for redirecting the laser, resulting in a possible point of failure due to wear, while also suffering from motion blur and relatively slow refresh rate, since the single beam cannot illuminate the entire scene at the same time [47]. Detector arrays illuminate the scene at once, and then a series of detectors capture each of the returning beam, using them to create a point cloud, not unlike a camera. However, this has its price: the moving parts are replaced with multiple detectors, each one needed to be calibrated, and the resolution of the image is fixed by the detector array, while in a scanning system the laser can be pointed in a specific direction within the Field of View (FoV) precisely [47].

Beyond the systems themselves, the method of determining the time of flight of the light can be also separated into *flash* or *continuous wave*, with the first being more common in space applications and consisting of sending a pulse of light and waiting for its return, while the *continuous wave* method measures the phase difference between the emitted and the received signal with wave modulation. From these techniques, *continuous wave* only operates at close ranges, 10 m, due to phase angle ambiguities, while *Flash* has no such problem [47].

For this thesis, a single LiDAR beam pointed in the z axis direction of the SC was considered, not unlike [26], to provide a range measurement between the SC and Apophis. This type of sensor is also called a laser rangefinder, and for the rest of this thesis will be refered as an altimeter, given its function. Furthermore, in order to avoid finding the intersection of a discrete body model with the ray of the altimeter, the altimeter measurement was approximated to

$$y_l = d + b_l + v_l, \tag{2.33}$$

where v_l is a Gaussian white noise, b_l a first order Gauss Markov process noise, described in Section 2.5.2.6, and d the distance between the SC and the ray's intersection with a perfect ellipsoid model. This value can be expressed by,

$$\begin{cases} a =\mathbf{e}^{\mathsf{T}}\boldsymbol{\Lambda}\mathbf{e}, & \text{(2.34a)} \\ b =\mathbf{x}^{\mathsf{T}}\boldsymbol{\Lambda}\mathbf{e}, & \text{(2.34b)} \\ c =\mathbf{x}^{\mathsf{T}}\boldsymbol{\Lambda}\mathbf{x}, & \text{(2.34c)} \\ d =\dfrac{-b-\sqrt{b^2-4ab}}{2a}, & \text{(2.34d)} \end{cases}$$

given the orientation of the ray $\mathbf{e}$ and the position of the SC $\mathbf{x}$ in relation to the ellipsoid principal axis r.f., alongside the diagonal matrix of the squared inverse of the principal axes radii, $\boldsymbol{\Lambda}$. Furthermore, (2.34) can validate its own result: if the SC does not point to the asteroid, then d will be complex, and if the SC points in the opposite direction of Apophis, d is negative.

2.4.2 Monocular Camera

Monocular cameras are, unlike LiDARs, passive sensors, that measure light emitted and/or reflected in the scene in a given range of frequencies, namely in the visible spectrum. The main characteristics of a monocular camera are its FoV in each axis, F_n, and its number of pixels, R_n, determining the angular resolution of the camera, F_n/R_n.

The advantage of using monocular cameras instead of LiDAR systems for processing the environment is the lower power and space requirements, while also being simpler [48]. With this said, it is important to note that passive EO sensors, such as cameras, are more dependent on lighting conditions than active sensors, and monocular cameras do not fully map the scene information.

A monocular camera can be modelled by a perfect pinhole projection, depicted in Fig. A.2, where a 3D point $\mathbf{p}$, expressed in $\{\mathcal{CA}\}$, input has as a 2D output $\mathbf{u}$. The relationship between $\mathbf{p}$ and $\mathbf{u}$ can be expressed as

$$\begin{bmatrix} a \\ b \\ c \end{bmatrix} = \begin{bmatrix} f_b & 0 & 0 \\ 0 & f_y & 0 \\ 0 & 0 & 1 \end{bmatrix} {}^{\mathcal{CA}}\mathbf{p}, \qquad \mathbf{u} = \begin{bmatrix} u \\ v \end{bmatrix} = \begin{bmatrix} -a/c \\ b/c \end{bmatrix} + \begin{bmatrix} R_x/2 \\ R_y/2 \end{bmatrix}, \tag{2.35}$$

where

$$f_x = \frac{\tan(F_x/2)}{R_x/2}, \qquad f_y = \frac{\tan(F_y/2)}{R_y/2}, \tag{2.36}$$

and (2.35) takes into account the camera pixel coordinate system represented in Fig. A.3.

If one were to try and convert the pixel output into the input point, it would be clear that it would be impossible without more information. In fact, any point that is in a semi-line connecting the camera focal point with the point $\mathbf{p}$ will have the same output. Although it is not possible to retrieve the input point $\mathbf{p}$ given the output of the camera, the direction of $\mathbf{p}$ in relation to the camera, $\mathbf{e}$, can be calculated, and their relation is

$$\begin{bmatrix} a' \\ b' \end{bmatrix} = \begin{bmatrix} u \\ v \end{bmatrix} - \begin{bmatrix} R_x/2 \\ R_y/2 \end{bmatrix}, \quad \mathbf{e} = \begin{bmatrix} -a'/f_x \\ b'/f_y \\ 1 \end{bmatrix} \frac{1}{\sqrt{\left(\frac{a'}{f_x}\right)^2 + \left(\frac{b'}{f_y}\right)^2 + 1}}, \tag{2.37}$$

concluding that monocular cameras measure the relative orientation of a point, and not its position.

For the remainder of this thesis is assumed that the angular aperture is the same in both camera axis, $F = F_x = F_y$, and resolution is also identical in both axis, $R = R_x = R_y$.

2.4.2.1 Centroiding

Although not directly a sensor in the traditional sense, the centroiding as an IP technique is used in conjunction with a monocular camera to provide the centre of mass of Apophis and, as such, the conjunction of camera and centroiding image processing can be seen as a sensor.

Some centroiding IP techniques described in [49] are centre-of-brightness, with this being the one chosen to be modelled, where the body is isolated in the image by isolating the body's illumination pixels and then the average position of them is used; limb-scanning, where limbs of the body are identified the image by matching the expected edges of those limbs with their correspondent projections on the image; and normalized cross-correlation, where the captured image is correlated with a rendering of the expected scene to find the centre of the figure.

The centre-of-brightness IP technique, although presenting poor precision, especially when the target is at closer ranges and/or at high phase angles, as evaluated in [49], and requiring the full body to be within the camera FoV, provides cheaper measurements in comparison to the other methods, that require either more computational effort and/or more knowledge about the target shape and rotational model.

With this said, no IP techniques were employed in this thesis, but instead modelled, due to the laborious process of generating synthetic images, implementing the methods discussed in the previous paragraph and the computational intensive burden that such processes are associated with. The modelling of the centroiding IP output was

$$\mathbf{y}_c = \mathbf{u}_{Ap} + r_{ap,px}\sqrt{\frac{2\alpha}{\pi}} b_c \mathbf{e}_S + r_{ap,px}\mathbf{v}_{CEN}, \tag{2.38}$$

where $\mathbf{e}_S$ is the direction of the Sun in the image, obtained by the normalization of the projection of the position of the Sun in the camera r.f. in its xy plane, $r_{ap,px}$ is the apparent mean radius of body, in pixels, α is the phase angle between Sun-Apophis-SC, b_c is a First Order Gauss Markov process noise, described in Section 2.5.2.6, v_c a Gaussian white noise, and $\mathbf{u}_{Ap}$ is the pixel position of the centre-of-mass of Apophis (2.35). Notice the the noise in pixels scales linearly with the apparent radius of Apophis and, therefore, at smaller distances the performance of this method deteriorates.

The square root of the phase angle normalized to 90 degrees, was chosen to simulate a fast increase in this error's effect when moving away from the ideal zero phase angle (with the Sun behind the camera and, therefore, the best illumination of the target), and the tapering off of this effect as α increases, noting that, as reviewed in Section 5.1.1, this angle will be capped at 90 degrees.

2.4.2.2 Feature Tracking

Feature tracking is the process of, as the name suggests, tracking unique image patche(s) on a sequential set of images, with the objective of this sections of the image corresponding to physical features of the observed scene.

Several fast algorithms were developed for feature tracking, such as the Kanade-Lucas-Tomasi algorithm, that relates sequential frames based on affine transformations of the original image while also keeping track of the quality of the feature [20–22] and the ORB algorithm, that generates a binary descriptor of the feature that can then be used to relate to the same image in the next frames [23].

The main advantages of tracking features instead of relying on the centroiding IP are the far more exact measurements that one can obtain with feature IP methods the closer the chaser get to the target, while also being able to keep track of the body's pose. However, these algorithms are more computationally intensive for detect and keep track of features.

As stated in Section 2.4.2.1, no IP techniques were implemented during this thesis. Instead, the measurement's model for a feature position in the captured image $\mathbf{u}_{FT,i}$ in the image is

$$\mathbf{y}_{ft,i} = \mathbf{u}_{ft,i} + \mathbf{v}_{ft,i} \tag{2.39}$$

where $\mathbf{v}_{FT,i}$ is a Gaussian white noise. Notice that, unlike the centroiding IP measurement (2.38) the noise of the output does not depend on the distance between the SC and Apophis. This reflects one of the previously mentioned advantages of feature tracking: when getting closer to the target the measurement error in position, assuming a given distance, is reduced due to the angular error, reflected in pixel error, being constant.

Another aspect of the feature measurement is that if the IP can, or not, identify the feature between different frames. To simulate this, an error limit was defined between the predicted position of the feature in the image and the measured one, and if crossed the interface would consider that feature not tracked.

One final issue regarding the usage of features its their initialization. When using LiDAR [5] or stereo-cameras [35] for feature tracking one has the required information to calculate the position of the feature in space, albeit with the noise associated with the measurements. As already pointed out in Section 2.4.2, the monocular camera only retrieves 2D information at a given, leaving the possible feature position as a line connecting the camera to the feature actual position. However, this problem can be readily solved if one has a model of the target by intersecting it (2.34) with the ray with the orientation of the camera's input line (2.37), with the distance to the target obtained with the altimeter.

Other solutions exist, such has having a already built database of the features [5], or relying on consecutive measurements to solve the 5 point motion problem [50], in the case that the body's shape is unknown and the features' relative motions in consecutive images are significant enough.

2.5 Dynamic Estimation

As briefly touched upon in Section 1.3.1, dynamic estimation is a method which bases itself upon the dynamical models of a system to estimate its states as they evolve through time. Two major advantages that this method have over other approaches is the ability to filter both measurement and process noises, and also the possibility of estimating states outside of the direct measurement relationships, provided that the system is observable. These advantages have made dynamic estimation observers an excellent choice for space related applications [51].

The observers contemplated in this thesis are, therefore, based on the dynamics of the system, namely the evolution of its states through time and the output of those states at a given time, called state and measurement dynamics, respectively.

Consider the dynamics of a general system in discrete time,

$$\begin{cases} \mathbf{x}(k) = \mathbf{f}(\mathbf{x}(k-1), \mathbf{u}(k-1), k, k-1) + \mathbf{M}(k+1, k)\mathbf{w}(k) & \text{(2.40a)} \\ \mathbf{y}(k) = \mathbf{h}(\mathbf{x}(k), k) + \mathbf{v}(k) & \text{(2.40b)} \end{cases}$$

where $k-1$ and k are two consecutive instances, $\mathbf{x}$ is the state of the system, $\mathbf{u}$ the system's input, $\mathbf{y}$ the system's output, $\mathbf{f}(.)$ and $\mathbf{h}(.)$ are function describing the state and measurement dynamics, respectively, $\mathbf{w}$ and $\mathbf{v}$ the process and measurement noises, respectively, and $\mathbf{M}(.)$ a function that relates the process noise to the system's state.

The estimation problem is the minimization of the estimation error of the state $\mathbf{x}(k)$ given the initial condition of the state, the set of inputs from 0 through $k-1$ and the measurements from 1 through k.

2.5.1 Algorithms and Formulations

The filter used in this thesis is an error state extended Kalman filter, also called multiplicative extended Kalman filter. This section aims to introduce the ground work for this filters and, from there, expand the scope gradually into its extensions and changes in formulations until the desired filter formulation is achieved.

2.5.1.1 Kalman Filter

The Kalman filter, as originally proposed in 1960 [29], is a recursive filter that fuses the current knowledge of the estimated state with received measurements at that time in such way that, provided a linear time varying (LTV) system where both dynamic and measurement models is correct and both process and measurement noises are Gaussian, zero-mean and uncorrelated, is optimal, in the sense that the new estimate minimises the expected mean-square error.

Consider a LTV system, where (2.41a) and (2.41b) corresponds to the particularization of (2.40a) and (2.40b), respectively,

$$\begin{cases} \mathbf{x}(k+1) =\mathbf{\Phi}(k+1,k)\mathbf{x}(k) + \mathbf{\Gamma}(k)\mathbf{u}(k) + \mathbf{M}(k+1,k)\mathbf{w}(k), & \text{(2.41a)} \\ \mathbf{y}(k+1) =\mathbf{H}(k+1)\mathbf{x}(k+1) + \mathbf{v}(k+1), & \text{(2.41b)} \end{cases}$$

where $\mathbf{\Phi}(k+1,k)$ is the system's transition matrix to time $k+1$ from time k, $\mathbf{\Gamma}(.)$ is a matrix valued function of the appropriate size and $\mathbf{H}(.)$ is the observation matrix, such that,

$$\mathbf{f}(\mathbf{x}(k),\mathbf{y}(k),k+1,k) = \mathbf{\Phi}(k+1,k)\mathbf{x}(k) + \mathbf{\Gamma}(k)\mathbf{u}(k),$$

$$\mathbf{h}(\mathbf{x}(k),k) = \mathbf{H}(k)\mathbf{x}(k).$$

Assume as well the initial state is characterized by

$$\mathsf{E}(\mathbf{x}) = \mathbf{x}(0), \qquad \mathsf{E}\left[(\mathbf{x}-\mathbf{x}(0))(\mathbf{x}-\mathbf{x}(0))^{\mathsf{T}}\right] = \mathbf{P}(0), \tag{2.42}$$

$\mathbf{w}$ and $\mathbf{v}$ are sequences of white, Gaussian uncorrelated noises, such that

$$\mathsf{E}(\mathbf{w}(k)) =\mathbf{0}, \qquad \mathsf{E}\left[\mathbf{w}(k)\mathbf{w}(l)^{\mathsf{T}}\right] = \mathbf{Q}(k)\delta(k-\tau), \tag{2.43}$$

$$\mathsf{E}(\mathbf{v}(k)) =\mathbf{0}, \qquad \mathsf{E}\left[\mathbf{v}(k)\mathbf{v}(l)^{\mathsf{T}}\right] = \mathbf{R}(k)\delta(k-\tau), \tag{2.44}$$

where $\mathbf{Q}(k)$ and $\mathbf{R}(k)$ are the respective covariance matrices at time k and $\delta(k-l)$ is the Dirac delta function.

With this, one can estimate $\mathbf{x}(k+1)$ by conditioning its probability distribution function to the state at time k, the input $\mathbf{u}(k)$ and measurement $\mathbf{y}(k+1)$.

The optimal solution for this problem is the algorithm of the Kalman Filter, and is separated in two steps. Firstly, a propagation step (2.45)

$$\begin{cases} \hat{\mathbf{x}}(k+1|k) =\mathbf{\Phi}(k+1,k)\hat{\mathbf{x}}(k) + \mathbf{\Gamma}(k)\mathbf{u}(k), & \text{(2.45a)} \\ \mathbf{P}(k+1|k) =\mathbf{\Phi}(k+1,k)\mathbf{P}(k|k)\mathbf{\Phi}^{\mathsf{T}}(k+1,k) + \mathbf{S}(k+1,k), & \text{(2.45b)} \end{cases}$$

where $\mathbf{S}(k+1,k) = \mathbf{M}(k+1,k)\mathbf{Q}(k)\mathbf{M}^{\mathsf{T}}(k+1,k)$, and conditions the "blind" state estimate $\hat{\mathbf{x}}(k+1|k)$, without outputs, to the evolution of the system from the previously estimated state $\hat{\mathbf{x}}(k|k)$ with the system's input and having in consideration the process uncertainties represented by $\mathbf{w}(k)$ in the covariance of the predicted state.

After the propagation, the correction step (2.46) is given,

$$\begin{cases} \mathbf{K}(k) =\mathbf{H}(k)^{\mathsf{T}}\mathbf{P}(k|k-1)(\mathbf{H}(k)\mathbf{P}(k|k-1)\mathbf{H}^{\mathsf{T}}(k) + \mathbf{R}(k))^{-1}, & \text{(2.46a)} \\ \hat{\mathbf{x}}(k|k) =\mathbf{K}(k)(\mathbf{y}(k) - \mathbf{H}(k)\hat{\mathbf{x}}(k|k-1)), & \text{(2.46b)} \\ \mathbf{P}(k|k) =(\mathbf{I} - \mathbf{K}(k)\mathbf{H}(k))\mathbf{P}(k|k-1), & \text{(2.46c)} \end{cases}$$

where the previously "blind" estimation is conditioned to the outputs observed by the filter, in accordance to their respective uncertainties. The gain $\mathbf{K}(k)$ is chosen to minimize the expected mean-square estimation error $J = \mathsf{E}\left[||\mathbf{x}(k) - \hat{\mathbf{x}}(k|k)||^2\right]$, with the derivation of $\mathbf{K}$ found in [29], noting that, since the system is linear, by definition, the state at the beginning is a Gaussian vector and both noises are also Gaussian vectors, the conditional probability density functions will too be Gaussian at all times, which allows the KF to be the optimal filter under the assumptions made.

One important mention to do, before moving to the effects of the initialization and noise parameters of the Kalman Filter, is that the system must be globally observable to ensure convergence of the filter state, and if it is, then it presents an exponential convergence rate.

The parameters $\mathbf{Q}$ and $\mathbf{R}$ describing process and measurement noise covariances, respectively, will affect the convergence speed and error, with each one working in opposite ways when determining the gain $\mathbf{K}$ (2.46a): on one hand, $\mathbf{Q}$ can be seen as how much the model should be trusted, with an increase in this value will lead to a larger perceived degradation of the state estimation during propagation, therefore, less confidence, which will increase the correction gain for the same $\mathbf{R}$; on the other hand, $\mathbf{R}$ is an indication of the measurement accuracy, and an increase in its value will lead to a filter that is more confident on its state model. A filter more reliant on its state dynamics will have a slower convergence but less disturbances during steady-state than a filter that trusts its measurements more, and part of the process of implementing a KF is its tuning, that can be done by performing tests on the system, evaluating statistically its process and measurement noise, or fine-tuning it with custom values in order to obtain reasonable results. Note that $\mathbf{R}$ has a direct relationship with the measurement sensors, and thus is more readily deducted from sensor sheets than $\mathbf{Q}$, which evaluates the overall system propagation noise over time and is harder to define.

Regarding the initialization of the filter, this should reflect the starting uncertainty of the system's state, considering the mean of the Gaussian pdf at that point $\hat{\mathbf{x}}(0|0)$ and its covariance $\mathbf{P}(0|0)$. Usually this uncertainty is unknown, resulting in common simplification of setting the initial covariance a diagonal matrix.

2.5.1.2 Extended Kalman Filter

The Extended Kalman Filter (EKF) is, as the name implies, an extension of the KF, specifically for nonlinear systems. This extension is necessary due to the non linear dynamics, will make so that the probability density functions that provide the minimum mean-square estimation error are non Gaussian [30].

The core idea of the EKF is to linearize the system's dynamics, whether they are the state or observation dynamics, around the last estimated state, and, in practice, treat the system as a LTV system, as opposed to either simplifying the problem too much and just linearize the system around an equilibrium point, where large deviations would be more likely to arise and invalidate such linearization, or trying to keep track of nonlinear Gaussian pdf during propagation and correction, which would be computationally expensive. By going with the middle route, one should keep the linearizations valid, provided a relatively small error in the estimation compared to the system's dynamics' nonlinearities, and with that being able to enjoy the Kalman Filter, now near-optimal, estimation process.

The main steps are the same as in the KF, however one has to compute $\mathbf{\Phi}(k+1,k)$, $\mathbf{S}(k+1,k)$

and $\mathbf{H}(k)$ by linearizing the system at the time of their evaluations, adding these processes to the propagation and correction steps, in addiction to integrating the system's state dynamics and evaluating its observation dynamics. Section 2.6 covers the discretization of continuous systems, and it should be applied during these proceedings.

One relevant note is that the previous covariance correction (2.46a) is not valid, since $\mathbf{K}$ is not optimal: the state covariance $\mathbf{P}$ and state dynamics are only approximated with this method, and therefore $\mathbf{K}$ is also approximately optimal. For this reason, the covariance update should be done instead with Joseph's Formula,

$$\mathbf{P}^{+} = (\mathbf{I} + \mathbf{K}\mathbf{H})\mathbf{P}^{-}(\mathbf{I} + \mathbf{K}\mathbf{H})^{\mathsf{T}} + \mathbf{K}\mathbf{R}\mathbf{K}^{\mathsf{T}}, \tag{2.47}$$

where the time k was omitted for clarity and the superscript $-$ corresponds a propagated variable, while $+$ to a corrected variable. Besides being valid for any $\mathbf{K}$, the Joseph's Formula also is more numerically stable due to its symmetric and additive form [52].

Note that, although the EKF can offer near-optimal results when the error is small, and have a fast convergence rate, there are no convergence guarantees, unlike the ones provided by the KF, raising issues regarding the applicability in pose determination, since the initial values can contain errors large enough to invalidate the linear approximations.

2.5.1.3 Error State Extended Kalman Filter

The error state extended Kalman filter, also known as a multiplicative extended Kalman filter, is a modification of the EKF where the state, as previously conceived, is split into a nominal part and error part, from now on called nominal state and an error state, respectively. The composition of the nominal and errors states is called the true state. With this split, the nominal state is used to propagate the nominal dynamics and, therefore, the mean of the estimated state, while the error state will reflect the uncertainty of the estimation and collect the errors captured during the correction phase [39].

For the purpose of this thesis, two types of states are considered: vector states, $\mathbf{v}$ and quaternion states, $\mathbf{q}$, with the latter referring to attitude representations and the former to all other quantities. The split between nominal, $\mathbf{x}_n$ and error, $\delta\mathbf{x}$, states are, for the respective state types,

$$\mathbf{v}_t = \mathbf{v}_n + \delta\mathbf{v} \tag{2.48}$$

$$\mathbf{q}_t = \mathbf{q}_n \odot \mathbf{q}\{\delta\theta\}. \tag{2.49}$$

Some of the advantages that this method provides, given the proposed attitude representation are [53]:

- The error state $\delta\theta$ is minimal, in contrast to its nominal quaternion representation, which avoids issues related to violating the normalization constraint for unitary quaternions;

- The error state, by being minimal, provides a more understandable reading of the state's covariance, since their parameters are not intrinsically restricted;

- The error state system is always operating close to its origin and, therefore, where the attitude representation has less issues;

In general it also allows simplifications in the Jacobians computation, given that second-order products of the error states are negligible.

The procedure for a full step of the MEKF changes from that of the EKF, due to the fact that now the system's dynamics used to propagate and correct the covariance of the state are no longer in respect to the nominal state but in respect to the error state, and adding a new step, the update, where the nominal state is injected with the error state (2.50a), the error state reseted (2.50c) and covariance updated to reflect this reset (2.50b). This is a particularly important step that should be done after every correction, since one major advantage of the filter is its error state being $\mathbf{0}$ during propagation, allowing to skip their value propagation and ensuring that $\hat{\mathbf{x}}_n$ is the most recent estimation.

The update step can be summarized as

$$\begin{cases} \hat{\mathbf{x}}_n = \mathbf{g}(\hat{\mathbf{x}}_n, \delta\hat{\mathbf{x}}), & \text{(2.50a)} \\ \mathbf{P} = \mathbf{G}\mathbf{P}^{+}\mathbf{G}^{\mathsf{T}}, & \text{(2.50b)} \\ \delta\hat{\mathbf{x}} = \mathbf{0}, & \text{(2.50c)} \end{cases}$$

where $\mathbf{g}$ is the composition function of the respective nominal-error state pair and $\mathbf{G}$ is the Jacobian of the reset functions, developed in [39].

2.5.2 Special Techniques

With the MEKF explained, it is relevant to note that the environment in question poses a number of challenges that would be poorly solved by an off-the-shelf filter implement. The techniques detailed in this section were employed precisely to solve those problems, from non-observable parameters to latency in measurements.

2.5.2.1 Kalman-Schmidt Filter

One improvement over the Kalman filter is the Kalman-Schmidt filter, or consider Kalman filter, developed in 1966 by Schmidt [54]. This filter allows the consideration of uncertain parameters that can either affect the dynamic or the measurement models, being suitable for systems where low observability of parameters is present [52].

The main change, in comparison to the KF, is the inclusion of ”consider” states in the filter's state, that will not be corrected, and, therefore, the correction step is also modified. Assume a filter whose states are divided between estimated states, $\mathbf{s} \in \mathbb{R}^n$, and consider states, $\mathbf{p} \in \mathbb{R}^m$,

$$\mathbf{x}^{\mathsf{T}} = \begin{bmatrix} \mathbf{s}^{\mathsf{T}} & \mathbf{p}^{\mathsf{T}} \end{bmatrix}, \quad \mathbf{P} = \begin{bmatrix} \mathbf{P}_{ss} & \mathbf{P}_{sp} \\ \mathbf{P}_{ps} & \mathbf{P}_{pp} \end{bmatrix}, \tag{2.51}$$

with $\mathbf{x}$ being the full state. Thus,

$$\mathbf{K}_{opt} = \begin{bmatrix} \mathbf{K}_{\mathbf{s},opt} \\ \mathbf{K}_{\mathbf{p},opt} \end{bmatrix} = \mathbf{P}\mathbf{H}^{\mathsf{T}} \left(\mathbf{H}\mathbf{P}\mathbf{H}^{\mathsf{T}} + \mathbf{R}\right)^{-1} = \mathbf{P}\mathbf{H}^{\mathsf{T}}\mathbf{W}^{-1}, \tag{2.52}$$

and the state covariance update becomes

$$\mathbf{P}^{+} = \begin{bmatrix} \mathbf{P}_{ss}^{+} - \mathbf{K}_s\mathbf{W}\mathbf{K}_s^{\mathsf{T}} & \mathbf{P}_{sp}^{-} - \mathbf{K}_s\mathbf{H}\begin{bmatrix} \mathbf{P}_{sp}^{-} \\ \mathbf{P}_{pp}^{-} \end{bmatrix} \\ \mathbf{P}_{ps}^{-} - \begin{bmatrix} \mathbf{P}_{sp}^{-} \\ \mathbf{P}_{pp}^{-} \end{bmatrix}^{\mathsf{T}} \mathbf{H}^{\mathsf{T}}\mathbf{K}_s^{\mathsf{T}} & \mathbf{P}_{pp}^{-} - \mathbf{K}_s\mathbf{H}\begin{bmatrix} \mathbf{P}_{sp}^{-} \\ \mathbf{P}_{pp}^{-} \end{bmatrix} - \begin{bmatrix} \mathbf{P}_{sp}^{-} \\ \mathbf{P}_{pp}^{-} \end{bmatrix}^{\mathsf{T}} \mathbf{H}^{\mathsf{T}}\mathbf{K}_s^{\mathsf{T}} + \mathbf{K}_p\mathbf{W}\mathbf{K}_p^{\mathsf{T}} \end{bmatrix}. \tag{2.53}$$

Notice that neither the cross-covariance of the estimated states with the considered one nor the covariance of the estimated states depend on $\mathbf{K}_{\mathbf{p}}$.

It can be shown [55] that the Schmidt-Kalman filter gain can be obtained from the optimal Kalman gain by setting out $\mathbf{K}_{\mathbf{p}} = \mathbf{0}$, or,

$$\mathbf{K} = \mathbf{S}\mathbf{K}_{opt}, \quad \mathbf{S} = \begin{bmatrix} \mathbf{I}^{n\times n} & \mathbf{0}^{n\times m} \\ \mathbf{0}^{m\times n} & \mathbf{0}^{m\times m} \end{bmatrix}, \tag{2.54}$$

with the alternative being calculating $\mathbf{P}$ and $\hat{\mathbf{x}}$ as if all states are estimated and then reverting the changes for $\mathbf{P}_{pp}$ and $\mathbf{p}$.

Finally, although already implemented while discussing the EKF, it is important to note that the update equation using this gain must be done with the Joseph's Formula (2.47), due to the simplified correction (2.46c) only being applicable when using $\mathbf{K}_{opt}$.

2.5.2.2 UDU Factorization

One of the issues that can affect the stability of the KF is the numeric error intrinsic to calculations. This error can be aggravated when the covariance matrix $\mathbf{P}$ has a ”weak” diagonal or when non-linearities appear, possibly resulting in the relatively important loss of symmetry or even loss of positive definiteness, which would result in $\mathbf{P}$ losing its meaning and the filter diverging [52].

To solve this issue, several factorization algorithms were developed, with UDU being one of the most popular. The premise of the algorithm is that $\mathbf{P}$ can be split into two matrices: a diagonal $\mathbf{D}$ and a triangular $\mathbf{U}$, in a way that

$$\mathbf{P} = \mathbf{U}\mathbf{D}\mathbf{U}^{\mathsf{T}}, \tag{2.55}$$

where efficient algorithms can be used to calculate the propagation and measurement steps of the KF.

For this thesis only the modified Gram-Schmidt orthogonalization, presented in [56], was implemented for the propagation and update steps, with measurement, reset, feature initialization and feature elimination being calculated on $\mathbf{P}$ and then converted into $\mathbf{U}$ and $\mathbf{D}$ with the algorithm expanded upon in [52]. The modified Gram-Schmidt orthogonalization algorithm provides the $\mathbf{U}$ and $\mathbf{D}$ components of

$\mathbf{P}^{+}$, such that

$$\mathbf{P}^{+} = \mathbf{A}\mathbf{P}^{-}\mathbf{A}^{\mathsf{T}} + \mathbf{B}, \tag{2.56}$$

where $\mathbf{A}$ and $\mathbf{B}$ are positive definite matrices. Notice that both the propagation (2.45) and the update (2.50b) steps are written as such.

The reason for the partial implementation of the UDU algorithm was a equilibrium between implementation and results: the main issues of numeric errors happened during the propagation of the covariance, and the implementation of the UDU method for calculating the propagation, alongside conversion in between the other steps, was enough to solve all non-positiveness issues.

2.5.2.3 Latency

One aspect to consider in filters is that measurements have latency, i.e., the filter will be ahead of the measurements. While this time difference might be insignificant for fast interfaces and small-sized, data wise, measurements, IP measurements such as the ones employed in this thesis require large data inputs, especially considering the power, processing and data size limitations during space missions. These differences may lead to the filter diverging if sufficiently large, and therefore, should be accounted by it [52].

Consider that the filter is at time t_k and the the measurement to account for is at time t_m, with $t_k > t_m$. Furthermore, consider the Taylor series of 1st order of the measurement dynamics

$$\mathbf{h}(\mathbf{x}_m, t_m) = \mathbf{h}(\hat{\mathbf{x}}_m, t_m) + \mathbf{H}_m\tilde{\mathbf{x}}_m, \tag{2.57}$$

where $\tilde{\mathbf{x}}_m$ is the error of the estimation at measurement time. This error can be related to the error at the propagation time by (2.41a),

$$\tilde{\mathbf{x}}_m = \mathbf{\Phi}(t_m, t_k)\tilde{\mathbf{x}}_k + \mathbf{M}_m\mathbf{w}. \tag{2.58}$$

Ignoring the process noise term, with the assumption that during the delay its small comparing to $\mathbf{\Phi}$, the new value of the residual and observation matrix become

$$\begin{cases} \mathbf{r} = \mathbf{y} - \mathbf{h}(\hat{\mathbf{x}}_m), & \text{(2.59a)} \\ \mathbf{H} = \mathbf{H}_m\mathbf{\Phi}(t_m, t_k), & \text{(2.59b)} \end{cases}$$

with $\hat{\mathbf{x}}_m$ being calculating by back integrating $\hat{\mathbf{x}}_k$ to t_m [52]. The same algorithm used for the usual forward propagation of the state was used to propagate $\hat{\mathbf{x}}_m$ and simultaneously calculate $\mathbf{\Phi}(t_m, t_k)$.

2.5.2.4 Underweighting

Underweighting is the term referring the technique where the measurement correction of the EKF is diminish in value by increasing its perceived variance. The necessity of underweighting the correction comes from the non-linearities of the measurement, that are not captured in the calculation of $\mathbf{H}$, clashing with the relative high uncertainty of the state, leaving the filter to overestimate the certainty of the estimation, and, in extreme cases, causing the filter to diverge.

One solution to this issue may pass by adding a term $\mathbf{B}$ in the inverted term in (2.46a),

$$\mathbf{K} = \mathbf{H}^{\mathsf{T}}\mathbf{P}^{-}(\mathbf{H}\mathbf{P}^{-}\mathbf{H}^{\mathsf{T}} + \mathbf{R} + \mathbf{B})^{-1}, \tag{2.60}$$

where the time relation is omitted.

There are different methods of calculating $\mathbf{B}$, with [52] focusing on three: expanding the measurement function $\mathbf{h}$ with a Taylor-series and truncating it at the 2nd order, and using the second order term to calculate $\mathbf{B}$ and, while it has theoretical merit, its computationally expensive; assuming that $\mathbf{B}$ is proportional to $\mathbf{R}$, which, although implementable, lacks a solid theoretical foundation, since $\mathbf{R}$ its not related to the measurement linearization process, and for that reason it may also lead to a more difficult tunning procedure; and considering $\mathbf{B}$ proportional to $\mathbf{HPH}^{\mathsf{T}}$, which was employed in the Orion and the Space Shuttle programs [52], and reasons that the direction of the errors caused by the non-linearities is the same as the linear error, but the magnitude should be increased to count them. The gain, therefore, becomes,

$$\mathbf{K} = \mathbf{H}^{\mathsf{T}}\mathbf{P}^{-}(\mathbf{H}\mathbf{P}^{-}\mathbf{H}^{\mathsf{T}}(1+\beta) + \mathbf{R})^{-1}, \tag{2.61}$$

where β defines how much underweighted the correction becomes.

The need to apply underweighting can be determined by the filter given certain conditions, such as the magnitude of the position uncertainty being larger than a certain threshold or simply a certain measurement being used. One clear effect of this technique is the slow down of the convergence speed of the filter, with this being a desired characteristic for the EKF.

2.5.2.5 Batch Correction

When incorporating different measurements for the correction of the filter, it is usual to process them at the same time, using the usual correction step (2.46). However, there might be cases when processing measurements one at the time, but still in the same correction step, is preferable, with one such case being when desiring to underweighting specific measurements instead of all.

There are three considerations to make before implementing a batch correction: firstly, the measurement noises must be uncorrelated [52], since the measurements will be processed individually. Secondly, that the nominal state is not updated between corrections, ensuring that the order in which the measurements are taken do not affect the filter's final state. Thirdly, if the filter has consider parameters. If so, the final output must return the consider states mean and covariance to their original value. Section 2.5.2.1 already showed that the only change in output between a filter with and without consider parameters is the maintenance of the self-correlation and mean of the consider parameters.

For m measurements, where R_i is the i^{th} element of the diagonal measurement noise matrix $\mathbf{R}$, $\mathbf{H}_i$ is the i^{th} row of the observation matrix $\mathbf{H}$, and i_p are the indices of the consider parameters of the filter, Algorithm 1 summarizes the batch correction [57].

Algorithm 1 Batch correction with consider parameters

```
$\tilde{\mathbf{x}}_0 = 0$
$\mathbf{P}_0^+ = \mathbf{P}^-$
for $i = 1$ until $m$ do
    $r_i = y_i - h_i(\hat{\mathbf{x}}^-, t)$
    $\mathbf{K} = \mathbf{P}_{i-1}^+ \mathbf{H}_i^\mathsf{T} (\mathbf{H}_i \mathbf{P}_{i-1}^+ \mathbf{H}_i^\mathsf{T} + R_i)^{-1}$
    $\tilde{\mathbf{x}}_i \leftarrow \tilde{\mathbf{x}}_{i-1} + \mathbf{K}_i (r_i - \mathbf{H}\tilde{\mathbf{x}}_{i-1})$
    $\mathbf{P}_i^+ = (\mathbf{I} + \mathbf{K}_i \mathbf{H}_i) \mathbf{P}_{i-1}^+ (\mathbf{I} + \mathbf{K}_i \mathbf{H}_i)^\mathsf{T} + \mathbf{K}_i R_i \mathbf{K}_i^\mathsf{T},$
end for
$\tilde{\mathbf{x}}_m(i_p) \leftarrow 0$
$\mathbf{P}_m^+(i_p, i_p) \leftarrow \mathbf{P}^-(i_p, i_p)$
$\hat{\mathbf{x}}^+ \leftarrow \hat{\mathbf{x}}^- + \tilde{\mathbf{x}}_m(i_p)$
```

2.5.2.6 Gauss Markov process noise

When characterizing errors in state and measurement dynamics, only white, zero-mean, Gaussian noises or constant biases were explicitly considered in the filter formulations. However, it may so happen that a bias changes through time, and it is important that the filter has this in consideration when evaluating the uncertainties of its state.

A way of representing this changing bias is a random walk, where the bias b_{RW} is the result of integrating a zero mean white Gaussian noise w_{RW},

$$\dot{b}_{RW} = w_{RW}, \tag{2.62}$$

resulting in the covariance growing linearly in relation to time. This representation is simple and forces the covariance of the bias to be positive by being constantly stimulated by noise. However, it has the drawback that, for non observable or considered states, the covariance growing to infinity, leading to numeric issues. It also cannot represent biases that can be considered within a certain maximum uncertainty.

An improvement on this method is the Gauss Markov process noise, namely the First Order Gauss Markov process noise (FOGM). The dynamics of this noise are

$$\dot{b}_{FOGM} = -\frac{1}{\tau} b_{FOGM} + w_{FOGM}, \tag{2.63}$$

where w_{FOGM} is a zero mean white Gaussian noise with variance q and τ is a positive real number that controls the time correlation of the FOGM, and is usually called its time constant. As τ increases, $\dot{b}_{FOGM}$ will decay slower, and in the limit that τ reaches infinity, the FOGM becomes a random walk, where no decay is present. On the contrary, if τ decreases, the initial value of b_{FOGM} will vanish faster.

In contrast to the random walk, the FOGM has a steady-state constant covariance, with its value being related to the input noise covariance and dynamic's time constant by

$$\sigma_\infty^2 = \frac{q\tau}{2}. \tag{2.64}$$

This result allows the modelling of the FOGM such that its covariance remains within certain bounds while being constantly stimulated by noise, having the same advantages that a random walk would provide. One important note to make is that the mean of a FOGM will naturally tend to 0.

2.6 Discretization

The dynamic and kinematic equations in continuous time, as they have been laid out in Section 2.3, clash with the dynamic estimators, whose derivations are for equations in discrete time that, given the discrete nature of digital signal processing, are only natural. This section has the purpose to bridge this gap between the continuous dynamics that rule the system and discrete-time requirements of the estimators.

Consider a generic continuous-time system

$$\begin{cases} \mathbf{x}(t) = \mathbf{f}(\mathbf{x}, \mathbf{u}, t) + \mathbf{B}(t)\mathbf{w}(t), & (2.65a) \\ \mathbf{y}(t) = \mathbf{h}(\mathbf{x}, t) + \mathbf{v}(t), & (2.65b) \end{cases}$$

where $\mathbf{x} \in \mathrm{R}^{n\times 1}$ is the state of the system, $\mathbf{B}(.) \in \mathrm{R}^{n\times l}$ a function relating the process noise with the state's derivative, $\mathbf{y} \in \mathrm{R}^{m\times 1}$ the output of the system, $\mathbf{w} \in \mathrm{R}^{l\times 1}$ and $\mathbf{v} \in \mathrm{R}^{m\times 1}$ are the process and measurement noise, respectively, the measurement dynamics. Neither $\mathbf{f}(.)$ nor $\mathbf{h}(.)$ are necessarily linear.

The desired values to find in order to use (2.45)-(2.46) and, therefore, any of the detailed filters with their proper modifications, are

$$\mathbf{x}(k+1) = \mathbf{x}(k) + \int_k^{k+1} \mathbf{f}(\mathbf{x}(t), \mathbf{u}(t), \mathbf{t})\mathrm{d}t, \tag{2.66}$$

$$\mathbf{\Phi}(k+1, k) = \int_k^{k+1} \mathbf{\Phi}(k+1, t)\mathbf{A}(t)\mathrm{d}t, \tag{2.67}$$

$$\mathbf{S}(k+1, k) = \int_k^{k+1} \mathbf{\Phi}(k+1, t)\mathbf{B}(t)\mathbf{Q}(t)\mathbf{B}^{\mathsf{T}}(t)\mathbf{\Phi}^{\mathsf{T}}(k+1, t)\mathrm{d}t, \tag{2.68}$$

$$\mathbf{H}(t) = \left.\frac{\partial \mathbf{h}(\mathbf{x}, \tau)}{\partial \mathbf{x}}\right|_{\mathbf{x}=\mathbf{x}(t), \tau=t}, \tag{2.69}$$

where

$$\mathbf{\Phi}(k, k) = \mathbf{I}, \quad \mathbf{A}(t) = \left.\frac{\partial \mathbf{f}(\mathbf{x}, \mathbf{u}, \tau)}{\partial \mathbf{x}}\right|_{\mathbf{x}=\mathbf{x}(t), \mathbf{u}=\mathbf{u}(t), \tau=t}. \tag{2.70}$$

Since neither $\mathbf{f}$ nor $\mathbf{h}$ are necessarily linear, there might be no known analytical solution to this integrals, and therefore numeric methods should be used to solve (2.66)-(2.68).

In accordance with results shown in [52], the second order middle-point Runge-Kutta method was used to approximate $\mathbf{\Phi}(k+1, k)$, and, since $\mathbf{x}(k+1)$ is integrated in conjunction with $\mathbf{\Phi}$, was also approximated with this method,

$$\begin{cases} \mathbf{x}(t+\Delta t/2) \approx \mathbf{x}(t) + \mathbf{f}(\mathbf{x}(t), \mathbf{u}(t), t)\Delta t/2, & \text{(2.71a)} \\ \mathbf{x}(t+\Delta t) \approx \mathbf{x}(t) + \mathbf{f}(\mathbf{x}(t+\Delta t/2), \mathbf{u}(t+\Delta t/2), t+\Delta t/2)\Delta t, & \text{(2.71b)} \\ \mathbf{\Phi}(t+\Delta t, t) \approx \mathbf{I} + \mathbf{A}(t+\Delta t/2)\Delta t + \mathbf{A}^2(t+\Delta t/2)\dfrac{\Delta t^2}{2}. & \text{(2.71c)} \end{cases}$$

For $\mathbf{S}(k+1,k)$, however, a Forward Euler propagation was implemented assuming that $\mathbf{Q}(t) = \mathbf{Q}$ and $\mathbf{B}(t) = \mathbf{B}$ are constant during the integration and $\mathbf{\Phi}(t+\Delta t, t)$ can be approximated to its 1st order Taylor series, resulting in

$$\begin{aligned} \mathbf{S} \approx & \int_t^{t+\Delta t} (\mathbf{I} + \mathbf{A}\tau)\mathbf{B}\mathbf{Q}\mathbf{B}^\mathsf{T}(\mathbf{I} + \mathbf{A}\tau)^\mathsf{T} \mathsf{d}\tau = \\ = & \mathbf{B}\mathbf{Q}\mathbf{B}^\mathsf{T}\Delta t + (\mathbf{A}\mathbf{B}\mathbf{Q}\mathbf{B} + \mathbf{B}\mathbf{Q}\mathbf{B}\mathbf{A}^\mathsf{T})\frac{\Delta t^2}{2} + \mathbf{A}\mathbf{B}\mathbf{Q}\mathbf{B}\mathbf{A}^\mathsf{T}\frac{\Delta t^3}{3}, \end{aligned} \tag{2.72}$$

where $\mathbf{A} = \mathbf{A}(t)$.

Regarding the differentiation of a generic scalar function $f(.)$, one may also approximate it using the definition of derivative

$$\left.\frac{\partial f(\alpha)}{\partial \alpha}\right|_{\alpha = x} = \lim_{\delta \longrightarrow 0} \frac{f(x+\delta) - f(x)}{\delta}, \tag{2.73}$$

given a small enough δ, such as 10^{-6}. Additionally, at the cost of doubling the calculations required, the difference forward can be averaged with the difference backwards to reduce errors, resulting in

$$\left.\frac{\partial f(\alpha)}{\partial \alpha}\right|_{\alpha = x} \approx \frac{f(x+\delta) - f(x-\delta)}{2\delta}. \tag{2.74}$$

Finally, its worth pointing out that the numeric result of the state dynamics does not respect the normalization constraint for the quaternion state. To solve this issue a zero-order integration was used, where the angular velocity is assumed to be constant and equal to its value at mid-step [39],

$$\mathbf{q}(t+\Delta t) = \mathbf{q}(k+1) \odot \mathbf{q}\{\omega(t+\Delta t/2)\Delta t\}. \tag{2.75}$$

Chapter 3

Problem Statement

Consider the spacecraft as a chaser SC, a Apophis a the target AP, a r.f. aligned with the target principal inertia axis body-frame r.f. $\{\mathcal{AP}\}$ and a relative inertial r.f. $\{\mathcal{CI}\}$, both with origin on the centre-of-mass of the target. The problem addressed in this thesis is the estimation of the relative position of the chaser to the target and the tracking of the target's attitude in respect to $\{\mathcal{CI}\}$ in real-time with on-board measurements. Hence, the desired states of the system are

- ${}^{\mathcal{CI}}\mathbf{x}_{SC}(t)$, the relative position of the chaser in $\{\mathcal{CI}\}$;
- ${}^{\mathcal{CI}}\mathbf{v}_{SC}(t)$, the relative velocity of the chaser in $\{\mathcal{CI}\}$;
- ${}^{\mathcal{CI}}_{\mathcal{AP}}\mathbf{q}(t)$, the attitude quaternion that relates $\{\mathcal{AP}\}$ with $\{\mathcal{CI}\}$;
- ${}^{\mathcal{AP}}\boldsymbol{\omega}_{AP}(t)$, the angular velocity of the target expressed in $\{\mathcal{AP}\}$.

The goal of this thesis is to develop and validate a solution that can estimate the desired states with an approximate geometric model of the target but without an *a priori* knowledge of the target's features and no other target attitude measurements, while being robust to measurement and dynamic biases.

In this scenario, the significant forces exerted on the chaser are the gravitational forces of Apophis, Earth, Sun and Moon, alongside the SRP, generally described in Section 2.3.2. However, to simulate processing constraints and verify the filter's robustness to acceleration biases, the position of the Moon will be unknown by the filter and, therefore, its force not directly counted in its state dynamics.

The rotational dynamics also showcased the possibility of a significant torque due to Earth's gravitational gradients on the body. Here a discrepancy between the information available to the filter is also present, with the filter not directly modelling this torque. The inertia tensor ${}^{\mathcal{AP}}\mathbf{J}$ is assumed to be known without uncertainties.

Regarding the measurements detailed in Section 2.4, consider that the frequency of the measurements are 1 per minute, with latency of the same time duration, and the filter has partial knowledge of each model, knowing their dynamics but not the values of the altimeter and centroiding biases, b_l and b_c, respectively.

Assume that the target's surface can be represented as a sphere within a certain error margin, that the features can be modelled as points on the surface and that their position in $\{\mathcal{AP}\}$ is fixed, since the target is a rigid body. Moreover, consider that the attitude and angular velocity of the target is known, up to an error, when initializing the feature tracking measurements for the first time and that, at no other point in time during the attitude estimation, the filter has less than five features to correct its state at any given instant, i.e., at least five features are successfully tracked between measurements. This value is used in [35] and is also the minimum number of points to a five-point algorithm to work [50].

Finally, consider that the chaser can command its attitude ${}^{\mathcal{CI}}_{\mathcal{SC}}\mathbf{q}(t)$ between measurements, up to a Gaussian white noise error. This noise simulates the control error that the chaser would suffer in real conditions. The the relative attitude of the camera relative to the chaser, ${}^{\mathcal{SC}}_{\mathcal{CA}}\mathbf{q}$, can be considered a constant bias.

With this assumptions in place, the system dynamics can be described by, omitting the time dependence for clarity,

$$\left\{\begin{aligned}
{}^{\mathcal{CI}}\dot{\mathbf{x}}_{SC} =& {}^{\mathcal{CI}}\mathbf{v}_{SC} && \text{(3.1a)}\\
{}^{\mathcal{CI}}\dot{\mathbf{v}}_{SC} =& \mathbf{a_c}({}^{\mathcal{CI}}\mathbf{x}_{SC}, \mathbf{0}, \mu_{AP})+ &&\\
& +\mathbf{a_c}({}^{\mathcal{CI}}\mathbf{x}_{SC}, {}^{\mathcal{CI}}\mathbf{x}_{E}, \mu_E) - \mathbf{a_c}(\mathbf{0}, {}^{\mathcal{CI}}\mathbf{x}_{E}, \mu_E)+ &&\\
& +\mathbf{a_c}({}^{\mathcal{CI}}\mathbf{x}_{SC}, {}^{\mathcal{CI}}\mathbf{x}_{S}, \mu_S) - \mathbf{a_c}(\mathbf{0}, {}^{\mathcal{CI}}\mathbf{x}_{S}, \mu_S)+ &&\\
& +\mathbf{a_c}({}^{\mathcal{CI}}\mathbf{x}_{SC}, {}^{\mathcal{CI}}\mathbf{x}_{M}, \mu_M) - \mathbf{a_c}(\mathbf{0}, {}^{\mathcal{CI}}\mathbf{x}_{M}, \mu_M)+ &&\\
& +\mathbf{a_c}({}^{\mathcal{CI}}\mathbf{x}_{SC}, {}^{\mathcal{CI}}\mathbf{x}_{S}, -\rho_S) && \text{(3.1b)}\\
{}^{\mathcal{CI}}_{\mathcal{AP}}\dot{\mathbf{q}} =& \frac{1}{2}{}^{\mathcal{CI}}_{\mathcal{AP}}\mathbf{q} \odot {}^{\mathcal{AP}}\boldsymbol{\omega}_{\mathcal{AP}} && \text{(3.1c)}\\
{}^{\mathcal{AP}}\dot{\boldsymbol{\omega}}_{AP} =& {}^{\mathcal{AP}}\mathbf{J}^{-1}({}^{\mathcal{AP}}\boldsymbol{\tau}_{AP} - {}^{\mathcal{AP}}\boldsymbol{\omega}_{AP} \times {}^{\mathcal{AP}}\mathbf{J}{}^{\mathcal{AP}}\boldsymbol{\omega}_{AP}) && \text{(3.1d)}\\
\dot{b_l} =& -\tau_l^{-1} b_l + w_l && \text{(3.1e)}\\
\dot{b_c} =& -\tau_c^{-1} b_c + w_c && \text{(3.1f)}\\
{}^{\mathcal{AP}}\dot{\mathbf{x}}_{FT,i} =& \mathbf{0} && \text{(3.1g)}\\
{}^{\mathcal{SC}}_{\mathcal{CA}}\dot{\mathbf{q}} =& \mathbf{0} && \text{(3.1h)}
\end{aligned}\right.$$

where w_l and w_c are Gaussian white noises, E, S, and M represent Earth, Sun, and Moon, respectively, μ_N is the gravitational constant of body N, ρ_N the radiation pressure of body N, $\mathbf{a_c}(\mathbf{x}_1, \mathbf{x}_1, \mu)$ represents a central acceleration applied to body 1 by body 2 with constant μ, as defined in Section 2.3.2 and ${}^{\mathcal{AP}}\boldsymbol{\tau}_{AP}$ is the gravitational torque (2.31).

The true measurement dynamics for the altimeter (2.33), centroiding (2.38), and features (2.39) have been presented throughout section 2.4 and are, respectively, rewritten here,

$$\left\{\begin{aligned}
y_l &= d + b_l + v_l, && \text{(3.2a)}\\
\mathbf{y}_c &= \mathbf{u}_{ap} + r_{ap,px}\sqrt{\frac{2\alpha}{\pi}} b_c \mathbf{e}_S + r_{ap,px}\mathbf{v}_c && \text{(3.2b)}\\
\mathbf{y}_{ft,i} &= \mathbf{u}_{ft,i} + \mathbf{v}_{ft,i}. && \text{(3.2c)}
\end{aligned}\right.$$

Chapter 4

Problem Approach

Given the background and the problem at hand, the following step is to develop a solution for it. This chapter provides a detailed exposition and description of the conceived solution, presenting its mathematical formulation and assumptions, detailing the proposed filter, the control assumptions and feature management system.

4.1 Filter Design

The proposed solution for the estimation problem is an MEKF with consider parameters. Moreover, the filter has the ability to self-initialize, or bootstrap, features based on feature tracking measurements and own state estimations. The filter, with its workflow shown in Fig. B.1, is composed of several submodules, namely, and in order of operation in a time-step,

- Feature Reset;
- Residual calculation;
- Correction;
- Update;
- Feature Initialization;
- Propagation.

In this section each step is presented, describing how they work and remarking the underlying assumptions made.

4.1.1 Filter States

The first step to define a filter is the definition of its state vector and, therefore, the quantities of the system to be estimated. Some states that are present in the proposed filter were already mentioned in the problem statement. Furthermore, the chosen MEKF formulation splits the "full" state into a nominal and error states, adding the necessity to review both.

All states present in the filter can be viewed in Tab. B.1, where their names, nominal and error representations, composition rule, and units are written. The states can be separated into four main groups: translational states, rotational states, measurement biases, and feature positions. Apart from the Apophis attitude state, that is a quaternion state, all other states are vector states, and their composition rule was described in Section 2.5.1.3.

The first set of states to review are the ones related to the traslational dynamics of the SC: the position of the SC in $\{\mathcal{CI}\}$, ${}^{\mathcal{CI}}\mathbf{x}_{SC}$, its velocity, ${}^{\mathcal{CI}}\mathbf{v}_{SC}$, and non-modelled accelerations ${}^{\mathcal{CI}}\mathbf{a}_{SC,nm}$ on the same r.f.. These states are crucial for the purposes of this thesis, since they are the ones that will allow the filter to estimate the SC relative position to Apophis, with ${}^{\mathcal{CI}}\mathbf{a}_{SC,nm}$ dealing with forces not considered in the filter's system dynamics.

Other two important states are the altimeter and centroiding biases, b_l and b_c, respectively. These states will be consider parameters, and allow the filter to take into account the sensors' biases and not be overconfident of its estimation. In conjunction with the translational states, the measurement biases states form the core of the filter, being the minimal required states for the estimation of the position of the SC, meaning that a filter without feature tracking would not need the remaining states to properly work.

However, if one is to fully fulfil the objectives proposed, the rotational states of Apophis must be estimated: Apophis' attitude in relation to $\{\mathcal{CI}\}$, ${}^{\mathcal{CI}}_{\mathcal{AP}}\mathbf{q}$, its angular velocity expressed in its body-frame, ${}^{\mathcal{AP}}\boldsymbol{\omega}_{AP}$ and non-modelled torques, ${}^{\mathcal{AP}}\boldsymbol{\tau}_{AP}$. The non-modelled torques state is similar in purpose to ${}^{\mathcal{CI}}\mathbf{a}_{SC,nm}$, making the filter aware of the uncertainties posed by the gravitational pull of Earth.

Finally, the n_{ft} tracked features' positions, ${}^{\mathcal{AP}}\mathbf{x}_{ft,i}$, are also a quantity to be estimated, reflecting not only the position of the feature but the filter's uncertainty of that position. As is the case for the position of the SC, this states are vectors and their composition rule is the sum.

One notably missing state is the attitude of the camera in relation to the SC, ${}^{\mathcal{SC}}_{\mathcal{CA}}\mathbf{q}$, that would model the misalignment of the camera referred in Section 2.3.1. This error was considered small enough to not require its direct consideration, therefore, it is assumed by the filter that there is no misalignment and, consequently, ${}^{\mathcal{SC}}_{\mathcal{CA}}\mathbf{q} = [1\ 0\ 0\ 0]^{\mathsf{T}}$. Moreover, this error would not be observable and, therefore, if it were to be a state would be a consider parameter, just like the other measurement biases.

All error states are differentiated from the nominal states by an δ, with the exception being the attitude pair, already covered in this section. Moreover, due to the fact that the "full", or true, states are rarely referenced, and to lighten the use of subscripts, the nominal and true states share the same representation. Unless explicitly mentioned, when referring to a state, in text or in an equation, the state to consider is the nominal one.

4.1.2 Propagation Step

With the proposed states for the filter presented, the state dynamics of the system can be reviewed. Having the real state dynamics (3.1) in mind, the filter's system dynamics for the true states are

$$\left\{\begin{aligned}
{}^{\mathcal{CI}}\dot{\mathbf{x}}_{SC} &= {}^{\mathcal{CI}}\mathbf{v}_{SC} && \text{(4.1a)}\\
{}^{\mathcal{CI}}\dot{\mathbf{v}}_{SC} &= \mathbf{a_c}({}^{\mathcal{CI}}\mathbf{x}_{SC}, \mathbf{0}, \mu_{AP}) + \\
&\quad + \mathbf{a_c}({}^{\mathcal{CI}}\mathbf{x}_{SC}, {}^{\mathcal{CI}}\mathbf{x}_{E}, \mu_{E}) - \mathbf{a_c}(\mathbf{0}, {}^{\mathcal{CI}}\mathbf{x}_{E}, \mu_{E}) + \\
&\quad + \mathbf{a_c}({}^{\mathcal{CI}}\mathbf{x}_{SC}, {}^{\mathcal{CI}}\mathbf{x}_{S}, \mu_{S}) - \mathbf{a_c}(\mathbf{0}, {}^{\mathcal{CI}}\mathbf{x}_{S}, \mu_{S}) + \\
&\quad + \mathbf{a_c}({}^{\mathcal{CI}}\mathbf{x}_{SC}, {}^{\mathcal{CI}}\mathbf{x}_{S}, -\rho_{S}) + {}^{\mathcal{CI}}\mathbf{a}_{nm,SC} && \text{(4.1b)}\\
{}^{\mathcal{CI}}\dot{\mathbf{a}}_{nm,SC} &= -\frac{1}{\tau_{\mathbf{a}}}{}^{\mathcal{CI}}\mathbf{a}_{nm,SC} + \mathbf{w_a} && \text{(4.1c)}\\
\dot{b}_l &= -\frac{1}{\tau_l}b_l + w_l && \text{(4.1d)}\\
\dot{b}_c &= -\frac{1}{\tau_c}b_c + w_c && \text{(4.1e)}\\
{}^{\mathcal{CI}}_{\mathcal{AP}}\dot{\mathbf{q}} &= \frac{1}{2}{}^{\mathcal{CI}}_{\mathcal{AP}}\mathbf{q} \odot {}^{\mathcal{AP}}\boldsymbol{\omega}_{\mathcal{AP}} && \text{(4.1f)}\\
{}^{\mathcal{AP}}\dot{\boldsymbol{\omega}}_{AP} &= {}^{\mathcal{AP}}\mathbf{J}^{-1}({}^{\mathcal{AP}}\boldsymbol{\tau}_{nm,AP} - {}^{\mathcal{AP}}\boldsymbol{\omega}_{AP} \times {}^{\mathcal{AP}}\mathbf{J}{}^{\mathcal{AP}}\boldsymbol{\omega}_{AP}) && \text{(4.1g)}\\
{}^{\mathcal{AP}}\dot{\boldsymbol{\tau}}_{nm,AP} &= -\frac{1}{\tau_{\boldsymbol{\tau}}}{}^{\mathcal{AP}}\boldsymbol{\tau}_{nm,AP} + \mathbf{w}_{\boldsymbol{\tau}} && \text{(4.1h)}\\
{}^{\mathcal{AP}}\dot{\mathbf{x}}_{FT,i} &= \mathbf{w}_{ft,i} && \text{(4.1i)}
\end{aligned}\right.$$

where $\mathbf{w_a}$, $\mathbf{w}_{\boldsymbol{\tau}}$, $\mathbf{w}_{ft,i}$, w_l, and w_c are zero-mean Gaussian white noises and $\tau_{\mathbf{a}}$, $\tau_{\boldsymbol{\tau}}$, τ_l, and τ_c are real positive constants.

One important aspect of the proposed dynamics (4.1) is the substitution of forces and torques present in the real true system dynamics (3.1) by the states ${}^{\mathcal{CI}}\mathbf{a}_{nm,SC}$ and ${}^{\mathcal{AP}}\boldsymbol{\tau}_{nm,AP}$, respectively. What this entails is that some forces, namely the gravity of the Moon, as well as the gravitational torque affecting Apophis, are not directly modelled in the filter, and instead are purely considered errors in the dynamics, allowing a simpler propagation while still considering their effects.

Another important aspect to discuss is the model of the state dynamics biases, ${}^{\mathcal{CI}}\mathbf{a}_{nm,SC}$ and ${}^{\mathcal{AP}}\boldsymbol{\tau}_{nm,AP}$, and the measurement biases, b_l and b_c. The chosen model for this errors is a FOGM, introduced in Section 2.5.2.6, that is characterised by an input noise and by a time constant and is used when desiring to estimate a bias. The advantages of using a FOGM are twofold: on one hand, the FOGM allows the increase of the estimated uncertainty through time, something that a simple bias without noise input does not allow. On the other hand, it forces the uncertainty to reach a steady-state value even if the variable is not estimated, which would not be possible using a random walk. In fact, none of the proposed biases are actually estimated and, therefore, their evolution depends solely on the noise injected, time constant, and initial state.

With these remarks made about the filter's true state dynamics, the MEKF actually requires two different functions: the dynamics of the nominal state for the propagation of the estimated state and the Jacobian $\mathbf{A}$ of the error state's dynamics for the covariance propagation. The first is directly given by the true state dynamics (3.1) after disregarding all process noises, since the nominal state is the true state when the error state is $\mathbf{0}$ and, therefore, a simple substitution for each state can be applied.

To derive the Jacobian of the state dynamics in respect to the error state, one could expand the true states in the system (4.1) and from there isolate each error state derivative to arrive at the nominal equations. However, there is an easier way of computing $\mathbf{A}$ if resorting to its numerical computation is an available option. Consider a true state $\mathbf{x}$ such that its decomposition in nominal and error states, $\mathbf{x_n}$ and $\delta\mathbf{x}$, respectively, is

$$\mathbf{x} = \mathbf{x_n} + \delta\mathbf{x}, \tag{4.2}$$

and, therefore, the state dynamics and respective Jacobians in order to the error state are

$$\begin{aligned} \frac{\mathrm{d}\delta\mathbf{x}}{\mathrm{d}t} &= \frac{\mathrm{d}\mathbf{x}}{\mathrm{d}t} - \frac{\mathrm{d}\mathbf{x_n}}{\mathrm{d}t} \\ \partial\left(\frac{\mathrm{d}\delta\mathbf{x}}{\mathrm{d}t}\right)\frac{1}{\partial\delta\mathbf{x}} &= \partial\left(\frac{\mathrm{d}\mathbf{x}}{\mathrm{d}t}\right)\frac{1}{\partial\delta\mathbf{x}} - \partial\left(\frac{\mathrm{d}\mathbf{x_n}}{\mathrm{d}t}\right)\frac{1}{\partial\delta\mathbf{x}}. \end{aligned} \tag{4.3}$$

Notice that in the nominal dynamics $\mathrm{d}\mathbf{x_n}/\mathrm{d}t$ are independent of $\delta\mathbf{x}$ by definition and, therefore, the true state Jacobian is equal to the error state Jacobian,

$$\partial\left(\frac{\mathrm{d}\delta\mathbf{x}}{\mathrm{d}t}\right)\frac{1}{\partial\delta\mathbf{x}} = \partial\left(\frac{\mathrm{d}\mathbf{x}}{\mathrm{d}t}\right)\frac{1}{\partial\delta\mathbf{x}}. \tag{4.4}$$

This means that $\partial\left(\frac{\mathrm{d}\mathbf{x}}{\mathrm{d}t}\right)\frac{1}{\partial\delta\mathbf{x}}$ can be approximated by a numerical differentiation method (2.74), with the proper nominal-error states composition, which in this case is just the sum function. As mentioned during the definition of the states, all except ${}^{\mathcal{CI}}_{\mathcal{AP}}\mathbf{q}$ respect this composition rule. For this last state, its error dynamics are derived in [39] and are, considering the filter's states,

$$\delta\dot{\boldsymbol{\theta}}_{AP} = -{}^{\mathcal{AP}}\boldsymbol{\omega}_{AP} \times \delta\boldsymbol{\theta}_{AP} + \delta{}^{\mathcal{AP}}\boldsymbol{\omega}_{AP}. \tag{4.5}$$

One important part of the propagation phase to address is the influence of the process noise in the system's dynamics. As implied in the true system dynamics (4.1), process noise will only be injected in the non-modelled acceleration and torque, features' positions and altimeter and centroiding biases. This choice, as opposed to injecting noise in every state with tuned covariances, comes from a desire to better represent the real dynamics and simplify any tuning performed to the noises covariance's values, even if at a possible loss of performance of the filter. The resulting $\mathbf{B}^{\mathsf{T}}(t)\mathbf{Q}(t)\mathbf{B}^{\mathsf{T}}(t)$ that represent the covariance of the process noises and their interaction with the true state is the diagonal matrix

$$\mathbf{B}^{\mathsf{T}}(t)\mathbf{Q}(t)\mathbf{B}^{\mathsf{T}}(t) = \begin{bmatrix} \mathbf{0}^{6\times 6} & \cdots & & & & \cdots & 0 \\ \vdots & \mathbf{Q_a}(t) & & & & & \vdots \\ & & q_{b_l}(t) & & & & \\ & & & q_{b_c}(t) & & & \\ & & & & \mathbf{0}^{6\times 6} & & \\ \vdots & & & & & \mathbf{Q}_{\tau}(t) & \\ 0 & \cdots & & & & & \mathbf{Q}_{ft}(t) \end{bmatrix} \in \mathbb{R}^{20+3n_{ft}\times 20+3n_{ft}} \tag{4.6}$$

where

$$\mathbf{Q_a}(t) = \mathsf{E}(\mathbf{w_a}(t)\mathbf{w_a}^{\mathsf{T}}(t)) \in \mathbb{R}^{3\times 3}, \qquad \mathbf{Q}_{\tau}(t) = \mathsf{E}(\mathbf{w}_{\tau}(t)\mathbf{w}_{\tau}^{\mathsf{T}}(t)) \in \mathbb{R}^{3\times 3}, \tag{4.7}$$

$$q_{b_l} = \mathsf{E}(w_{b_l}(t)w_{b_l}(t)) \in \mathbb{R}^{3\times 3}, \qquad q_{b_c} = \mathsf{E}(w_{b_c}(t)w_{b_c}(t)) \in \mathbb{R}^{3\times 3}, \tag{4.8}$$

$$\mathbf{Q}_{ft,i} = \mathsf{E}(\mathbf{w}_{ft,i}(t)\mathbf{w}_{ft,i}^{\mathsf{T}}(t)) \in \mathbb{R}^{3\times 3}, \tag{4.9}$$

and $\mathbf{Q}_{ft} \in \mathbb{R}^{3n_{ft}\times 3n_{ft}}$ is the diagonal per blocks matrix that has as entries $\mathbf{Q}_{ft,i}$, the covariance of the process noise for the i^{th} feature position. Most of this process noises covariances are constants throughout the filter's application, given that the states they affect are being estimated, with the exception of the noise driving the non-modelled torques. This differentiation was made to improve the filter's performance, and only injects noise into the state in the interval of time between 6 hours before and 6 hours after the point of closest approach of Apophis to Earth. Moreover, when active, this injected noise has constant covariance.

Lastly, one issue regarding the application of the UDU covariance formulation must be mentioned: the modified Gram-Schmidt orthogonalization algorithm [56] for propagation forces all state variables to have a positive variance, or, in other words, to have some uncertainty. While in an usual filter this is not a problem, the proposed filter does not necessary consider all of its states at a given time, and as a result the variance of these states is 0. The choice of defining the non-accounted states' covariances to 0 is done to avoid the free integration of random variables, that would lead to numerical issues due to unchecked growth. The UDU covariance limitation is, however, easily bypassed by only considering the indexes of the states whose value in the $\mathbf{D}$ matrix is positive.

4.1.3 Correction Step

The second step of an MEKF is the correction of the prediction by the output of the system (3.2), and can be decomposed into two sub-processes: the calculation of the residual alongside the observation matrix and measurement noise matrix are analysed in Section 4.1.3.1, and the correction of the state's mean and covariance with the gain matrix and the previously calculated values is looked at in Section 4.1.3.2.

4.1.3.1 Residuals

For the calculation of the residuals, observation matrix and measurement noise matrix, is important to define filter's measurement equations, which are identical to the real ones, where y_l is the altimeter's measurement model presented in Section 2.33, $\mathbf{y}_c$ the centroiding measurement described in Section 2.38 and $\mathbf{y}_{ft,i}$ the feature tracking measurements mentioned in Section 2.39. The equations are

$$\begin{cases} y_l = d + b_l + v_l, & \text{(4.10a)} \\ \mathbf{y}_c = \mathbf{u}_{ap} + r_{ap,px}\sqrt{\frac{2\alpha}{\pi}} b_c \mathbf{e}_S + r_{ap,px}\mathbf{v}_c & \text{(4.10b)} \\ \mathbf{y}_{ft,i} = \mathbf{u}_{ft,i} + \mathbf{v}_{ft,i}, & \text{(4.10c)} \end{cases}$$

where d is the distance between the SC and the model of Apophis along the altimeter's direction (2.34) and, in it,

$$\mathbf{x} = {}^{\mathcal{AP}}\mathbf{x}_{SC} = {}^{\mathcal{AP}}_{\mathcal{CI}}\mathbf{R}^{\mathcal{CI}}\mathbf{x}_{SC} \tag{4.11}$$

$$\mathbf{e} = {}^{\mathcal{AP}}\mathbf{e}_{z,SC} = {}^{\mathcal{AP}}_{\mathcal{CI}}\mathbf{R}^{\mathcal{CI}}_{\mathcal{SC}}\mathbf{R}\begin{bmatrix}0 & 0 & 1\end{bmatrix}^{\mathsf{T}}, \tag{4.12}$$

the apparent radius of Apophis $r_{ap,px}$ is related to the distance to Apophis, the radius of Apophis, R_{ap}, and the camera's FoV, F, and its number of pixels, R,

$$r_{ap,px} = \frac{R}{F}\arcsin\left(\frac{R_{ap}}{||^{\mathcal{CI}}\mathbf{x}_{SC}||}\right), \tag{4.13}$$

the ideal pixel measurement of the centre-of-mass of Apophis, $\mathbf{u}_{ap}$, can be calculated (2.35) considering

$$^{\mathcal{CA}}\mathbf{p} = {}^{\mathcal{CA}}\mathbf{x}_{Ap} = {}^{\mathcal{CA}}_{\mathcal{SC}}\mathbf{R}^{\mathcal{SC}}_{\mathcal{CI}}\mathbf{R}(-{}^{\mathcal{CI}}\mathbf{x}_{SC}), \tag{4.14}$$

with the remaining terms of (4.10b), namely the phase angle α and Sun direction $\mathbf{e}_S$, being

$$^{\mathcal{CA}}\mathbf{x}_S = {}^{\mathcal{CA}}_{\mathcal{SC}}\mathbf{R}^{\mathcal{SC}}_{\mathcal{CI}}\mathbf{R}^{\mathcal{CI}}\mathbf{x}_S, \tag{4.15}$$

$$\mathbf{e}_S = \begin{bmatrix}-{}^{\mathcal{CA}}x_{S,x} & {}^{\mathcal{CA}}x_{S,y}\end{bmatrix}^{\mathsf{T}} \frac{1}{\sqrt{({}^{\mathcal{CA}}x_{S,x}^2 + {}^{\mathcal{CA}}x_{S,y}^2}}, \tag{4.16}$$

$$\alpha = \text{acos}\left(\frac{{}^{\mathcal{CI}}\mathbf{x}_{SC}^{\mathsf{T}}\,{}^{\mathcal{CI}}\mathbf{x}_S}{||^{\mathcal{CI}}\mathbf{x}_{SC}||\;||^{\mathcal{CI}}\mathbf{x}_S||}\right). \tag{4.17}$$

The pixel position of the i^{th} feature can be computed considering in the camera pinhole projection (2.35)

$$^{\mathcal{CA}}\mathbf{p} = {}^{\mathcal{CA}}\mathbf{x}_{ft,i} = {}^{\mathcal{CA}}_{\mathcal{SC}}\mathbf{R}^{\mathcal{SC}}_{\mathcal{CI}}\mathbf{R}({}^{\mathcal{CI}}_{\mathcal{AP}}\mathbf{R}^{\mathcal{AP}}\mathbf{x}_{ft,i} - {}^{\mathcal{CI}}\mathbf{x}_{SC}). \tag{4.18}$$

With the measurement model presented, the residual can be obtained by calculating the difference between the innovations of the measurements and the measurements themselves.

The observation matrix $\mathbf{H} \in \mathbb{R}^{3+2n_{ft} \times 14+3n_{ft}}$ can be calculated by approximating the Jacobian of the dynamics in respect to the error state $\mathbf{H_m}$ (2.69) at the measurement time, respecting the composition rule defined for each state. Since the measurements have latency, this alone is not enough, and the state transition matrix from the propagation time to measurement time must be multiplied to $\mathbf{H_m}$ (2.59b).

Something worth pointing out are the state dependencies of each measurement: all of the measurements depend on ${}^{\mathcal{CI}}\mathbf{x}_{SC}$, the altimeter and centroiding on their respective biases, b_l and b_c, but, considering the model of Apophis as a sphere, only the feature tracking depends on ${}^{\mathcal{AP}}_{\mathcal{CI}}\mathbf{q}$ and on ${}^{\mathcal{AP}}\mathbf{x}_{ft,i}$.

Finally, the diagonal measurement noise covariance matrix $\mathbf{R}$ is given by

$$\mathbf{R}(t) = \begin{bmatrix} R_l(t) & \dots & 0 \\ \vdots & \mathbf{R}_c(t) & \vdots \\ 0 & \dots & \mathbf{R}_{ft}(t) \end{bmatrix} \in \mathbb{R}^{3+2n_{ft} \times 3+2n_{ft}}, \tag{4.19}$$

where

$$R_l(t) = \mathsf{E}(v_l^2(t)), \qquad \mathbf{R}_c(t) = \mathsf{E}(\mathbf{v}_c(t)\mathbf{v}_c^{\mathsf{T}}) \in \mathbb{R}^{2\times 2}, \tag{4.20}$$

$$\mathbf{R}_{ft,i} = \mathsf{E}(\mathbf{v}_{ft,i}(t)\mathbf{v}_{ft,i}^{\mathsf{T}}(t)) \in \mathbb{R}^{2\times 2}, \tag{4.21}$$

and, as $\mathbf{Q}_{ft}$ was for the process noise, $\mathbf{R}_{ft} \in \mathbb{R}^{2n_{ft}\times 2n_{ft}}$ is the diagonal per blocks matrix that has as entries $\mathbf{R}_{ft,i}$, the covariance of the measurement noise for the i^{th} feature tracking measurement. The matrix $\mathbf{R}(t)$ is diagonal per blocks since each measurement noise is uncorrelated with all others.

A relevant remark to make is the absence of any mention of the pointing error of the SC in the measurement noise. In fact, this pointing error will introduce correlations into the measurements, since all of them depend on ${}^{\mathcal{SC}}_{\mathcal{CI}}\mathbf{q}$, that is affected by noise. With this said, the expected errors are in the order of $\sigma = 0.5$ mrad [58], which, as shown during the environment analysis in Section 5.1.2, are around a quarter of pixel, and therefore overshadowed by the comparatively large centroiding and feature tracking errors considered.

One important note to make is that the feature tracking measurements are not always available, due to the SC being too far away from Apophis to have an high enough resolution of its surface. This has implications on the estimation of the rotational states of Apophis, further discussed in Section 4.1.6.

4.1.3.2 Correction

After gathering the residuals, observation matrix and measurement noise covariance matrix, the next step is to correct the propagated state estimation by computing the gain $\mathbf{K}$ and, with it, obtain the new state estimation and uncertainty.

Before moving directly to the correction step, it is important to recall that one characteristic of this filter is its ability to consider parameters, meaning that the usual gain (2.47) cannot be used alone but multiplied by a selection matrix to account for this states (2.54). The state and measurement dynamics biases, ${}^{\mathcal{CI}}\mathbf{a}_{nm,SC}$, ${}^{\mathcal{CI}}\tau_{nm,SC}$, b_l and b_c, are always consider parameters.

Moreover, the non-linear nature of the attitude contributions to the measurement might require the use of underweighting, as detailed in Section 2.5.2.4. When this happens, the modified version of the filter's gain (2.61) is applied, with the preconfigured β for the condition. For this application, two situations proved the usage of the underweighting beneficial: in the initial steps, $\beta_p = 1.2$, where the error is large compared to the steady-state results for the centroiding-altimeter measurement couple, and this situation is said to occur when

$$\sqrt{\text{tr}(\mathbf{P}_{\mathbf{x}_{sc}})} > 100 \text{ m}, \tag{4.22}$$

where tr$(.)$ is the trace of a matrix and $\mathbf{P}_{\mathbf{x}_{sc}}$ is the covariance of the position of the SC.

The second event that merits underweighting is the integration of feature tracking measurements into the filter, since the non-linear relationship between their position and the SC proved to be large in the face of the initial uncertainties. The undeweighting parameter, β_{ft}, is only applied to the feature tracking measurements, unlike the previous one, and the trigger conditions are

$$\begin{aligned} \sqrt{\text{tr}(\mathbf{P}_{\mathbf{x}_{ft,i}})} \geq 5\% R_{ap} \Rightarrow \beta = \beta_{ft}, \\ 5\% R_{ap} > \sqrt{\text{tr}(\mathbf{P}_{\mathbf{x}_{ft,i}})} \geq 1\% R_{ap} \Rightarrow \beta = \beta_{ft}/2, \end{aligned} \tag{4.23}$$

where $\mathbf{P}_{\mathbf{x}_{ft,i}}$ is the covariance of the position of the i^{th} feature and R_{ap} is Apophis' radius.

4.1.4 Update

Mentioned during the background exposition in Section 2.5.1.3, the MEKF introduces a step after the correction of the estimated states, injecting the errors revealed by the measurements into the nominal state, resetting the mean of the error states and updating the covariance to reflect this transfer.

The update procedure for the filter is straight-forward, not distancing itself from the standard algorithm. The only relevant change is that, to use the modified Gram-Schmidt orthogonalization algorithm [56] for the covariance update (2.50b), one must first select the states in estimation, this is, states where the covariance is larger than 0, as it is done in the propagation step.

The injection of the error states into the nominal ones follows the composition rule for each state, defined in Section 4.1.1, and the reset consists in zeroing all error states. In practice, this means that the error state is only carried between the correction step and update steps, since the latter is always done right after the former.

The reset Jacobian $\mathbf{G}$ necessary for the covariance update (2.50b) is computed using the derivatives for the reset function for each state, with their derivation found in [39]. This means that

$$\mathbf{G} = \begin{bmatrix} \mathbf{I}^{11\times 11} & \dots & 0 \\ \vdots & \mathbf{I} - [\delta\boldsymbol{\theta}/2]_\times & \vdots \\ 0 & \dots & \mathbf{I}^{6+3n_{ft}\times 6+3n_{ft}} \end{bmatrix} \in \mathbb{R}^{20+2n_{ft}\times 20+2n_{ft}}. \tag{4.24}$$

At last, the covariance update can be done using the modified Gram-Schmidt orthogonalization algorithm by direct comparison of the update equation (2.50b) and the equation solved by the algorithm (2.56).

4.1.5 Feature Handling

The solution proposed for the problem at hand involves the self-initialization of features that the modelled IP technique, alongside the filter, is tracking, and their removal once they are no longer tracked. This subsection will present how the initialization and deletion of the features were done.

4.1.5.1 Feature Initialization

If a feature is detected for the first time by the feature tracking algorithm, its position on the surface of Apophis is unknown, and therefore, must be calculated and introduced in the correspondent filter position. One important note to make before explaining the initialization algorithm is that feature's pixel measurements are not used in the correction step until the feature is initialized, due to the fact that, before this step, there is no innovation for the measurement, since the innovation depends on the feature position estimation.

The initialization of the nominal position of the features is done by intersecting the filter's model of Apophis with the orientation of the ray whose orientation is given by the pixel output, so, finding $\mathbf{e}_{ft,i}$ with the output-input relationship of the camera (2.37) and applying it, alongside the estimated states of the system, to the intersection of the model relationship (2.34) to find the distance between the SC and the feature d. The nominal feature position is the intersection point between the ray and the model, computed by

$$^{\mathcal{AP}}\mathbf{x}_{ft,i} = {}^{\mathcal{AP}}\mathbf{x}_{SC} + d^{\mathcal{AP}}\mathbf{e}_{ft,i}. \tag{4.25}$$

With the nominal initialization covered, it is important to analyse the feature covariance initialization. There are three main sources of error when bootstraping a feature: state errors, measurement errors, and model errors. Each plays a different role and require different compensation methods.

The state errors are the errors introduced by not knowing the true state of the system, which results in an difference between the real feature position and the nominal feature position when determining the intersection point of the feature's ray with Apophis. These errors are, therefore, correlated with the other states, and it is important that the filter has the knowledge of this correlation. The procedure chosen to correlate the the feature with the rest of the states passes through the computation of the sensibility matrix

$$\mathbf{S}_{ft,i} = \frac{\partial^{\mathcal{AP}}\mathbf{x}_{ft,i}}{\partial \mathbf{x}}, \tag{4.26}$$

where $\mathbf{x}$ is full state of the system. Assuming that the initialized feature is the last state vector and the covariance of the other states is $\mathbf{P}_{pre}$, the full covariance can be calculated as

$$\mathbf{P}_{correlated} = \begin{bmatrix} \mathbf{P}_{pre} & \mathbf{P}_{pre}\mathbf{S}_{ft,i}^{\mathsf{T}} \\ \mathbf{S}_{ft,i}\mathbf{P}_{pre} & \mathbf{S}_{ft,i}\mathbf{P}_{pre}\mathbf{S}_{ft,i}^{\mathsf{T}} \end{bmatrix}. \tag{4.27}$$

The sensibility matrix relates the error of the feature initialization with the state error by linearizing the function around the nominal state. Due to the spherical nature of Apophis surface, however, there is one issue with this approach: the accounted errors are tangent to the surface norm. In a flat surface this

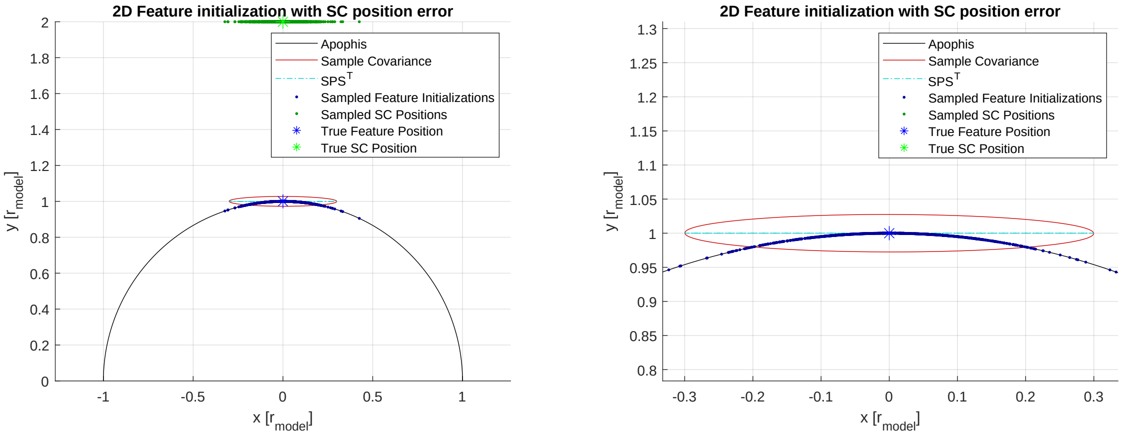

(a) Overall view.

(b) Detail of the features sampled.

Figure 4.1: 2D feature initialization sampling with SC position errors

would not be a problem, but if the surface to intersect has a significant curvature in relation to the state error, the error normal to the tangent of the surface at the nominal feature position might be too large to not compensate. When first initializing the features this might be the case, due to the relative large uncertainty on position of the SC.

With this said, the remaining analysis is made in relation to the SC's position uncertainty and not the attitude uncertainty of Apophis, having assumed that the errors caused to attitude errors would be both small and already captured by the proposed correction.

The effect of the curvature of Apophis can be seen in Fig.4.1, where the covariance of the sampled feature initializations in a 2D environment has a normal component, σ_{radial}, but the proposed covariance, $\mathbf{S}_{ft,i}\mathbf{P}_{pre}\mathbf{S}_{ft,i}$ does not. The SC has an initial uncertainty along the x axis, the direction perpendicular to the camera pointing direction, the y axis.

To mitigate this problem a term was added to the covariance to add a radial component to the covariance, with $\mathbf{P}_{correlated}$ becoming

$$\mathbf{P}_{correlated} = \begin{bmatrix} \mathbf{P}_{pre} & \mathbf{P}_{pre}\mathbf{S}_{ft,i}^{\mathsf{T}} \\ \mathbf{S}_{ft,i}\mathbf{P}_{pre} & \mathbf{S}_{ft,i}\mathbf{P}_{pre}\mathbf{S}_{ft,i}^{\mathsf{T}} + \mathbf{e_r}\mathbf{e_r}^{\mathsf{T}}\sigma_{radial}^2 \end{bmatrix}, \tag{4.28}$$

where $\mathbf{e_r}$ is the orientation vector of the surface norm that, being the surface a sphere, has the direction of the estimated feature position, and σ_{radial}^2 is the magnitude of the normal variance. This solution, although having the possibility of solving the correlation between the position of the feature, will not solve the inaccuracies introduced into the cross correlation between the features and the states, with one more accurate method being, for example, sampling a large number of initializations and correlating them directly with the state. However, the adopted solution has the advantage of not requiring sampling, being therefore less computationally expensive, and simpler in application.

The next question becomes how to properly define σ_{radial}^2 for any feature initialization. Two solutions were considered, with one relating the σ_{radial} directly with the uncertainty of the state $\sigma_{\mathbf{x}}$ and other with the magnitude of tangential covariance, σ_{tan}, that was already being approximated by $\mathbf{S}_{ft,i}\mathbf{P}_{pre}\mathbf{S}_{ft,i}^{\mathsf{T}}$

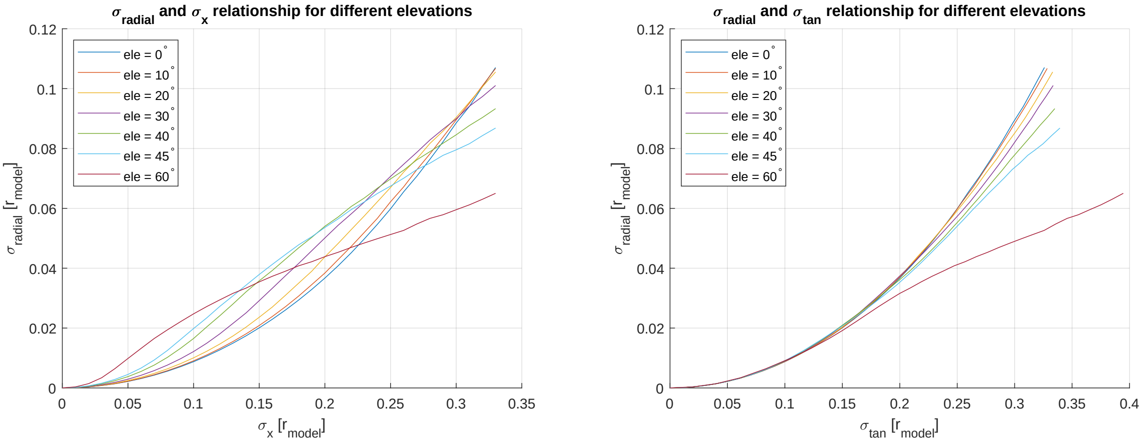

(a) $\sigma_{\mathbf{x}}$ and σ_{radial}. (b) σ_{tan} and σ_{radial}.

Figure 4.2: 2D feature initialization dispersion relationships for different elevations

and retrievable through its eigenvalues. The relationship of this quantities is displayed on Fig. 4.2 for different SC's elevations, and shows that, for both relationships, elevations above 45 do not have the same behaviour as the relations for higher elevations. Therefore, the initial elevation of the SC for a new feature should be larger than 45 degrees.

Another conclusion from Fig. 4.2 that can be taken is that the relationship with σ_{tan}, and consequently $\mathbf{S}_{ft,i}\mathbf{P}_{pre}\mathbf{S}_{ft,i}^{\mathsf{T}}$, is less dependent on the SC's elevation than the one with $\sigma_{\mathbf{x}}$. For this reason only the former relationship will be further considered, with the added benifit that it may also capture the uncertainty introduced by the attitude error, since this is also mirrored in the tangential uncertainty.

With the relationship chosen, the next step is to determine a function that reflects it. A simple quadratic function was chosen,

$$\sigma_{radial} = \alpha\sigma_{tan}^2, \tag{4.29}$$

and α was determined by a linear regression of all the curves presented in Fig. 4.2b given the proposed function, resulting in $\alpha \approx 0.9$ and the interpolating curve can be seen in Fig. 4.3.

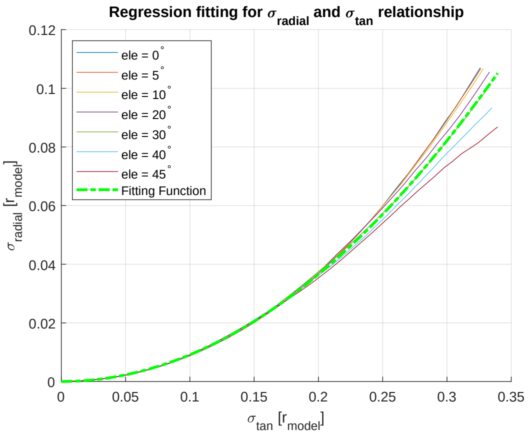

Figure 4.3: Regression for σ_{tan} and σ_{radial} relationship

Before moving to the remaining uncertainty sources, it is important to stress that the previous analysis was done considering uncertainties normalized to a circle radius and, therefore, when computing σ_{radial}, the tangential variance must be normalized and after using the parametrized function (4.29) re-dimensionalized.

The next error source to review is the measurement errors. These errors are zero mean white Gaussian noises as defined in the measurement dynamics (4.10). The correction for this errors is similar in concept to the state uncertainty correction, with a sensibility matrix $\mathbf{M}_{ft,i}$ linearizing the feature initialization in respect to the pixel input,

$$\mathbf{M}_{ft,i} = \frac{\partial^{\mathcal{AP}}\mathbf{x}_{ft,i}}{\partial \mathbf{y}_{ft,i}}, \tag{4.30}$$

and relating the noise covariance $\mathbf{R}_{ft,i}$ with the feature covariance, changing the previous formulation of $\mathbf{P}_{correlated}$ (4.28),

$$\mathbf{P}_{correlated} = \begin{bmatrix} \mathbf{P}_{pre} & \mathbf{P}_{pre}\mathbf{S}_{ft,i}^{\mathsf{T}} \\ \mathbf{S}_{ft,i}\mathbf{P}_{pre} & \mathbf{S}_{ft,i}\mathbf{P}_{pre}\mathbf{S}_{ft,i}^{\mathsf{T}} + \mathbf{e_r}\mathbf{e_r}^{\mathsf{T}}\sigma_{radial}^2 + \mathbf{M}_{ft,i}\mathbf{R}_{ft,i}\mathbf{M}_{ft,i}^{\mathsf{T}} \end{bmatrix}. \tag{4.31}$$

Although this method presents the same non-linear drawbacks as the initial state induced covariance, the magnitude of these errors was assumed to be much smaller than the ones due to the state uncertainty and, consequently, no radial correction term was added for these errors.

The last error source is the surface model uncertainty. This error appears due to the fact that Apophis is not a perfect sphere and, therefore, the actual position of the feature is not, necessarily, the one computed by the initialization. To compensate for this error, a final term is added to $\mathbf{P}_{correlated}$ (4.31), becoming

$$\mathbf{P}_{correlated} = \begin{bmatrix} \mathbf{P}_{pre} & \mathbf{P}_{pre}\mathbf{S}_{ft,i}^{\mathsf{T}} \\ \mathbf{S}_{ft,i}\mathbf{P}_{pre} & \mathbf{S}_{ft,i}\mathbf{P}_{pre}\mathbf{S}_{ft,i}^{\mathsf{T}} + \mathbf{e_r}\mathbf{e_r}^{\mathsf{T}}\sigma_{radial}^2 + \mathbf{M}_{ft,i}\mathbf{R}_{ft,i}\mathbf{M}_{ft,i}^{\mathsf{T}} + \mathbf{I}\sigma_{shape}^2 \end{bmatrix}, \tag{4.32}$$

and increasing the feature's covariance by a given amount σ_{shape}^2 in all directions equally. This value should reflect the error between the real surface and the assumed model but, if a better model for the body is not available, it becomes a tuning parameter.

There will also be the case where a known feature is initialized. In that case, there is no initial correlation of the feature with the other states, and the error is assumed to be only sized by σ_{shape}.

Finally, it is important to discuss the conditions in which a proposed feature might be rejected. The first barrier is its initialization, with the possibility of the filter not being able to find d due to a large error in the SC estimated position. Features not found are naturally rejected. Other aspects, such as the elevation of the SC in relation to the feature, or the phase angle of the SC in relation to the feature are not evaluated in this step, but in a posterior one. This means, in practice, that the feature is successfully initialized in the filter but will be deleted in the next measurement step and replaced with another available feature, redoing the initialization procedure.

4.1.5.2 Feature Removal

After a feature is initialized and tracked, it might happen that a feature is lost due to not fulfilling the required conditions for its observability: no longer being illuminated, either due to being on the non-visible side of Apophis or not being illuminated; or too far from their predicted position, with this second condition being further discussed in Section 4.2. In fact, even if the feature is still visible, it might not be desirable to keep track of it, with those situation being the result of being below a certain SC's elevation angle or even having a low Sun's elevation angle. Regardless, the features must be deleted from the filter, and this section presents how it was achieved, alongside the requirements of keeping a feature.

The feature removal from the filter is simple: when a feature is no longer tracked, the estimated position of the feature is set to $\mathbf{0}$ and all covariances related to the feature, self and cross correlations, are set to $\mathbf{0}$, indicating to posterior steps that the feature spot is empty, and, in practice, reducing the size of the filter, similar to what happens to the rotational states of Apophis when not estimated.

Regarding the requirements for a feature being tracked, the elevation of the SC is an important factor to consider, seeing that low elevation affect the error of the self initialization, as evaluated in Section 4.1.5.1, and would introduce distortions in the feature if a real application is considered. For this reason, a lower limit of 45 degrees was defined. The feature phase angle is also an important quantity to consider, although not represented in the error of the feature tracking, the illumination of the features plays an important role in how good a measurement is: a too high Sun elevation would lead to few shadows and, therefore, no contrast; a low elevation would result in large and distorted shadows where their centre would be hard to keep track of. Due to this, the upper and lower limits of 80 and 10 degrees of the feature phase angle was established. Both of these requirements should be broken before the feature is not visible.

Finally, it is important to mention that in the filter itself, only the removal of the feature is made, provided that an input flag from the feature tracking interface signals the filter to do it. The validation of the feature requirements is made in the feature management subsystem, touched upon in Section 4.2, to allow it to pick a new feature if the proposed one is not valid.

4.1.6 Modes

One aspect of the filter's environment is that the feature tracking measurements are not available at all times, and, therefore, hiding the rotational state of Apophis during the initial and final parts of the SC trajectory.

Therefore, the filter was conceived as having two modes: firstly, a mode where only the translational states of the SC and measurement biases are considered; secondly, a mode where the filter also estimates the rotational states of Apophis, that coincide with the introduction of feature tracking measurements and, therefore, the features' position estimation into the filter. This choice implies that there the attitude and angular velocity of Apophis will be initialized when receiving the first feature tracking measurements and, consequently, there is some *a priori* knowledge of these states at the desired time. Given that the feature tracking starts before the gravitational torques start taking effect, it can be assumed that this knowledge comes from an accurate ground propagation of Apophis free rotation from previous measurements [44].

Another possibility would be to fully initialize the filter and purely propagate the rotational states of Apophis until the feature tracking is available, and at that point also perform updates. However, there is a large downside to the aforementioned alternative, and that is the rapid growth of the uncertainty of the rotational states, namely the Apophis' attitude, after a long propagation time due to noise integration, which would not only cause numeric issues in the covariance calculation but also render the feature bootstrapping inaccurate, and consequently, the attitude estimation, due to a large attitude uncertainty.

With the reasoning of having modes already presented, their implementation is simple: a first sub-module verifies if the SC has entered or left the feature tracking validity region, that is defined by a sphere centred on Apophis with radius equal to the defined maximum distance for the measurements, and a second sub-modules resets the rotational states in accordance. When Apophis is out of range for the feature tracking, the covariance of the rotational states, self and cross covariances, is set to 0, the nominal attitude is set to a reference value, ${}^{\mathcal{CI}}_{\mathcal{AP}}\mathbf{q} = [1\ 0\ 0\ 0]^\mathsf{T}$, and the nominal angular velocity to $\mathbf{0}$, recalling that the nominal angular acceleration is always $\mathbf{0}$. When Apophis becomes in range of the feature tracking measurements, the filter is initialized with the true attitude and angular velocity, minus a random white Gaussian noise with a certain covariance.

4.2 Feature Tracking Interface

As said during the measurement review in Section 2.4.2.2, no feature tracking IP technique was employed in this thesis, being replaced by a noisy projection of the features on the camera. Nevertheless, an interface between the feature tracking measurements and the filter was used, effectively separating the raw feature tracking of all visible feature from the fixed size n_{ft} inputs that the filter receives. Therefore, this module is responsible to verify if a feature is tracked between measurements and initialize a new feature otherwise. Furthermore, if the features are known, the interface is also responsible to inform the filter of the stored position of the feature at its initialization.

The continuity of the feature tracking is done by checking the feature's visibility, the filter validity requirements, with its conditions being described in Section 4.1.5.2, and if the error between the actual feature measurement and the predicted measurement by the filter is within a 30 pixel wide square centred on the actual measurement. This last restriction is imposed in order to simulate the application of the feature tracking algorithm to a subsection of the image, reducing the computational effort by limiting the input into the algorithm, as well as prevent false positives between two similar features. In the case that the feature is visible but rejected, it goes to the pool of possible new features to track.

The next step is to provide a feature tacking measurement to allow the filter to initialize a new feature. Firstly, the valid feature tracking measurements for initialization are defined. These measurements exclude the measurements for the currently estimated features and already rejected measurements. Secondly, these selected measurements ordered in accordance to a cost function that describes how good a feature might be: the smaller the cost, the better the feature is. This goal function is the distance to the centre of the camera, since it is assumed that the camera is pointing to the Apophis' centre-of-mass and, considering Apophis a sphere, the elevation is larger the closer the projection is to the pointed direction.

Thirdly, after sorting the available measurements in ascending order, the first one is proposed to initialize a new feature. In this step, the feature is internally initialized to verify if the constraints described in Section 4.1.5.2 are met, with one extra condition being if the new feature is distanced of all others ones tracked by 10 m. This new condition ensures the dispersion of the tracked features across a larger surface area. This internal initialization is, at first glance, unnecessary, since it will not be used by the filter. However, it is crucial to avoid a loop between a proposal by the interface and rejection by the filter if measurements better positioned in terms of cost are not valid.

Finally, if the correspondent feature appears to be valid, the measurement is passed to the filter and the feature stored in the interface to know which measurement to keep track. If the feature of the proposed measurement does not meet the criteria of initialization, the feature is removed from the valid measurement pool for the remainder of the time step and the next best feature is evaluated, rewinding to the previous step.

This loop continues until all n_{ft} measurements are chosen or there are no more features, with the filter raising a flag indicating that no feature should be initialized by the empty outputs, or a flag indicating that the measurement corresponds to a new feature to initialized, if that is the case.

4.3 Guidance and Control

One final aspect to mention in the proposed solution is the desired interaction of the SC with the environment, be it regarding its translational states or rotational ones.

The trajectory in which the filter will be evaluated is a passive one, not requiring actuation, and, there will be no real deviation from this trajectory, in order to limit the scope of this thesis. Therefore, the translational states of the SC are not controllable and, therefore, neither guidance nor control is considered for this motion.

In contrast, the desired attitude of the SC is one that points both altimeter and camera towards the centre-of-mass of Apophis, allowing the best operation of all the sensors. For this reason, the desired attitude is dependent upon the current SC's position estimate. In this regard no attitude control was implemented, falling outside the scope of the thesis. It was assumed that the SC would be able to follow the desired attitude between time steps, apart from a zero-mean Gaussian white noise $\delta\boldsymbol{\theta}_u$ [58].

Chapter 5

Simulation Environment and Results

5.1 Real World Simulation

In order to test and validate the proposed filter, an environment was created to represent the assumed conditions in which the SC will operate on. This section presents each simulated step, starting at the trajectory of the spacecraft, presenting the measurement noises and finally moving to the Apophis' surface model.

5.1.1 Trajectory

To understand the scale of the quantities to estimate during the mission, it is important to present a brief analysis on the trajectory that the SC takes, showcasing relative distances and accelerations of it, while also looking into the rotation states of Apophis.

Firstly, is important to mention that only the SC's states and Apophis' rotational states were integrated during runtime, using the Simulink's *Ode4 (Runge-Kutta)* function, with a time step of one minute. The position of Apophis, Sun, Earth, and Moon were computed using NASA's SPICE Toolkit [59] and stored to upload in Simulink, noting that the mission starts at 21:45:03, 13 of April, 2029.

x [km]	y [km]	z [km]	$\dot{x}$ [mms^{-1}]	$\dot{y}$ [mms^{-1}]	$\dot{z}$ [mms^{-1}]
7.745	-8.015	-3.340	-70.0	100.6	39.0

(a) SC

R_{ap} [m]	q_w	q_x	q_y	q_z	ω_x [μdegs^{-1}]	ω_y [μdegs^{-1}]	ω_z [μdegs^{-1}]
170	0.0427	-0.0891	0.1868	-0.9774	621.1	-924.1	2153

(b) Apophis

Table 5.1: SC and Apophis initial conditions.

The initial conditions of the SC's translational states are presented in Table 5.1a, whereas the Apophis' rotational states are shown in Table 5.1b. The Apophis' rotational states were computed from its state at 2012 December 23.176388 UT [44], considering that the Apophis' angular momentum was

J_{xx}/J_{zz}	J_{yy}/J_{zz}	r_{ap} [m]
0.6	0.95	170

Table 5.2: Apophis parameters [44].

aligned with the z axis of $\{\mathcal{CI}\}$. The Apophis' parameters can be found in Table 5.2. Given these conditions, Fig. 5.1a and 5.1b showcase the position and velocity of the SC in $\{\mathcal{CI}\}$, respectively, noting that the relative velocity magnitude will stay in the order of 0.1 ms^{-1}.

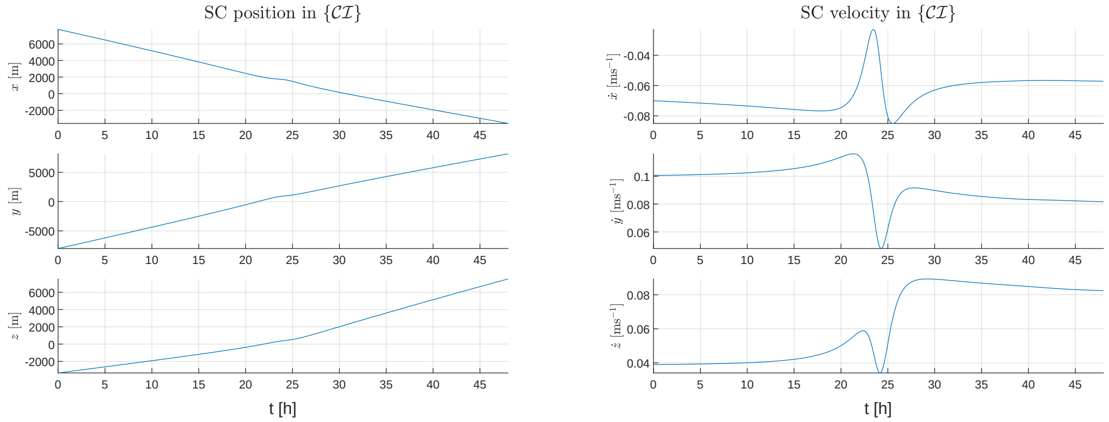

(a) Position of SC.

(b) Velocity of.

Figure 5.1: SC position and velocity in $\{\mathcal{CI}\}$.

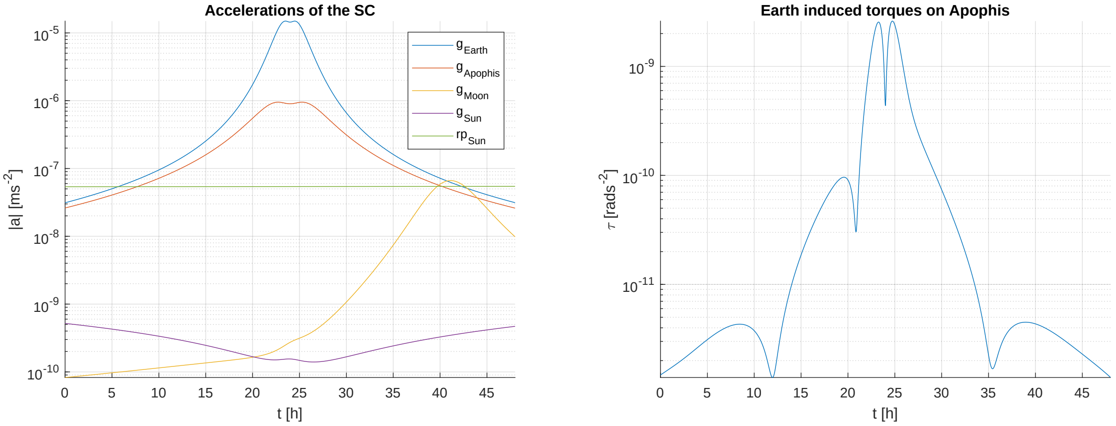

(a) Gravity, g, and radiation pressure, rp, accelerations applied on the SC in $\{\mathcal{CI}\}$.

(b) Normalized torques applied on Apophis.

Figure 5.2: SC accelerations and Apophis normalized torques during the mission.

Figure 5.2a details the accelerations of the SC, where it can be seen that the Earth and Apophis will have the most influence during the majority of the mission, with the solar radiation pressure of the Sun being more prevalent in the beginning and ending of the mission, and the Moon exerts a non-trivial acceleration in the last 13 hours of the mission due to a close passage on the outbound leg of the hyperbola, as it can be seen in Fig. 5.3b. The value of each acceleration constant can be found on Table 5.3, recalling their definitions in Section 3.

μ_{Ap} [m^{3}kg^{-1}s^{-2}]	μ_E [m^{3}kg^{-1}s^{-2}]	μ_M [m^{3}kg^{-1}s^{-2}]	μ_S [m^{3}kg^{-1}s^{-2}]	ρ_S [m^{3}kg^{-1}s^{-2}]
3.544	3.986×10^{14}	4.903×10^{12}	1.327×10^{20}	1.219×10^{15}

Table 5.3: Forces' Constants

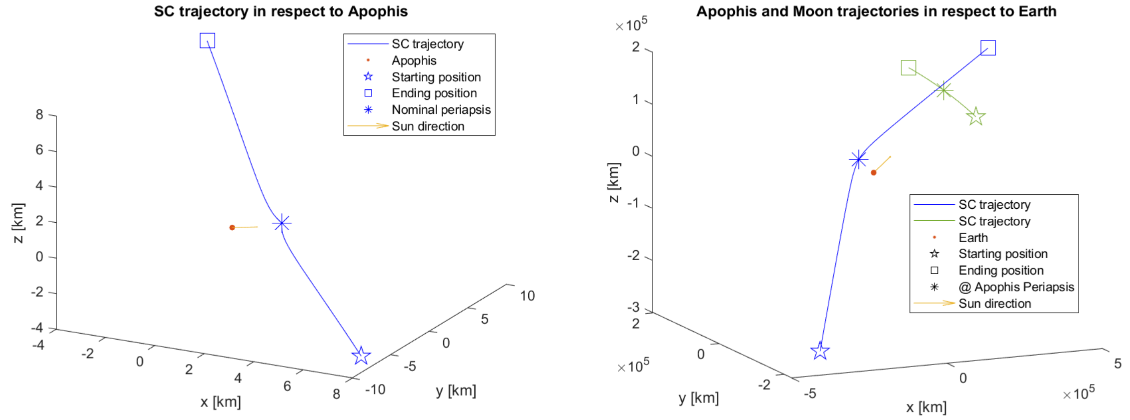

(a) SC trajectory relative to Apophis.

(b) Apophis trajectory relative to Earth.

Figure 5.3: SC and Apophis trajectories in $\{\mathcal{I}\}$

Figure 5.4 presents the distance between the SC and Apophis, alongside the Apophis-SC-Sun angle, or just phase angle, and Fig. 5.5 presents the apparent radius of Apophis with and without the phase angle influence function of the centroiding bias (2.38), using the camera parameters found in Table 5.5.

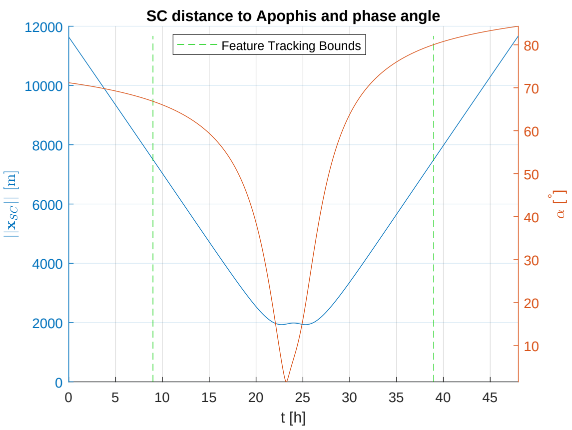

Figure 5.4: SC distance to Apophis and SC phase angle.

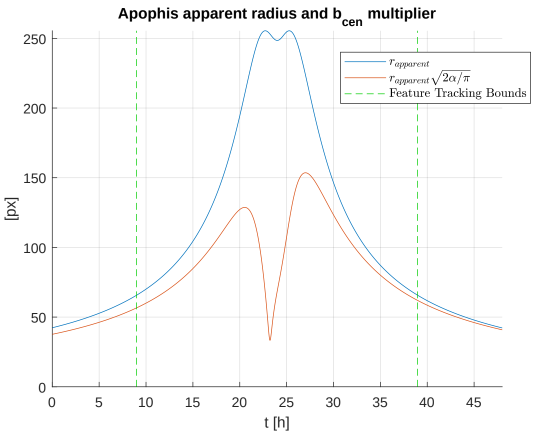

Figure 5.5: Apophis apparent radius and centroiding bias multiplier.

As it can be seen in Fig. 5.4, the SC fly-by starts with a distance of 12 km of Apophis and nominal periapsis of 2 km to Apophis, occurring after 24 hours of the beginning of the simulation, increasing the distance for the remainder of the simulation, reaching 12 km by the 48 hour mark. This point also coincides with the closest approach of Apophis to Earth, being, therefore, when its influence on Apophis is larger, as it can be seen in Fig. 5.2b by the angular accelerations forced on Apophis. Moreover, it can also be seen that the feature tracking phase will occur between 9 to 39 hours after the beginning of the mission, when Apophis has a more defined image as captured by the camera. This ranged is defined by the SC being in a distance of 7.5 km of Apophis, that is translated into 133 pixels of apparent diameter.

The phase angle of the SC, shown in Fig. 5.4, will start at 70 degrees and after the 15 hour mark rapidly decrease until it reaches 1 degree at 23 hours. After this minimum, the phase angle will rise quickly to 70 degrees at 32 hours and from there slowly reaching 85 degrees at the end of the mission. This means that, during the initial and final stages of the fly-by, the centroiding measurements will be more affected by the phase angle induced bias b_c and, at closer ranges, the white noise will become more influential. This evolution is mirrored in the bias multiplier term, $r_{ap,px}\sqrt{2\alpha/\pi}$, plotted in Fig. 5.5 and presented in the centroiding equation (2.38). Furthermore, during the maximum disturbance of Apophis rotation, between 18 and 30 hours after the start of the mission, the phase angle will be small, which will turn more features visible and give the feature tracking more options to choose from.

The rotational state of Apophis is also an interesting topic to discuss. For the initial states presented in Table 5.1b, the Euler angles of the attitude of Apophis with and without considering Earth's gravitational torque can be seen in Fig. 5.6a, while the angular velocity for both scenarios are presented in Fig. 5.6b. As it can be seen by the torque unaffected evolution of Apophis' angular velocity, ω is not aligned with the angular momentum and, therefore, even without external influence there is a change in ω, as demonstrated in Section 2.3.3.

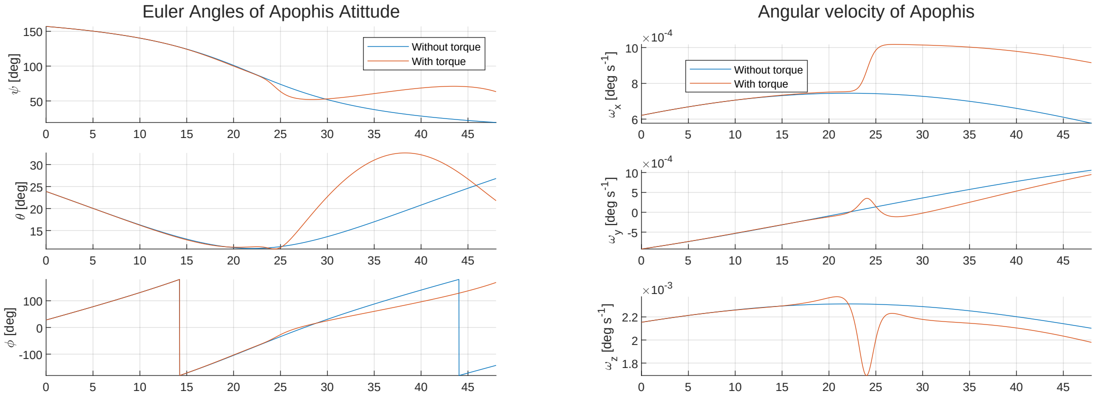

(a) Euler angles.

(b) Angular velocity.

Figure 5.6: Rotational states of Apophis with and without torques.

From both Fig. 5.6a and Fig 5.6, it is clear to see that the impact of the Earth gravitational pull on the rotational state of Apophis is not negligible, starting to make a significant difference around 15 hours after the start of the mission in the angular velocity, and its influence on the attitude can be perceived from the 24 hour mark. Since the feature tracking will, in turn, start at 9 h, as observable in Fig. 5.4, it can be assumed that, until this mode starts, the rotational states of Apophis are free from disturbances and, therefore, safely propagated and uploaded by ground, holding valid the premise of a small error filter initialization.

5.1.2 Measurement and Actuation Characterization

Two aspects that have been mentioned throughout the filter design, in Section 4.1, and measurement presentation, in Section 2.4, are the errors of each measurement and attitude control, be them white noises or biases. Further, the camera parameters, namely FoV and pixel size, are also relevant parameters to be defined.

The errors for the measurements and control are presented in Tab. 5.4, where σ_∞ is the FOGM steady-state error, $\delta\boldsymbol{\theta_u}$ is the error in the SC's attitude control, $\delta\boldsymbol{\theta_{CA}}$ is the angular misalignment of $\{\mathcal{SC}\}$ and $\{\mathcal{CA}\}$, $\sigma(\mathbf{x}_{ft,i})$ corresponds to the ground feature initialization error dispersion if the features are known. The remaining variables are defined in the measurement equations (2.40b). The camera parameters are displayed in Tab. 5.5.

$\sigma(v_l)$ [m]	$\sigma_\infty(b_l)$ [m]	τ_l [h]
$3\% r_{ap}$	$5\% r_{ap}$	6

(a) Altimeter errors.

$\sigma(\lVert\delta\boldsymbol{\theta_u}\rVert)$ [mdeg]	$\sigma_\infty(\lVert\delta\boldsymbol{\theta_{CA}}\rVert)$ [mdeg]
3	$20/3$

(b) Pointing errors and misalignment.

$\sigma(\mathbf{v}_c)$ $[\%]$	$\sigma_\infty(b_c)$ $[\%]$	τ_c [h]	$\sigma(\mathbf{v}_{ft,i})$ [px]	$\sigma(\mathbf{x}_{ft,i})$ [m]
5	$\sqrt{25^2 - 5^2}$	12	1	5

(c) Centroiding and Feature Tracking errors.

Table 5.4: Measurement and Control Errors

FoV F [°]	Pixel Size R [u]	Angular resolution $[m°]$
19.5	1048	18.6

Table 5.5: Camera parameters.

The centroiding measurement errors considered are proportional to the apparent radius of Apophis and are relatively large, reflecting the centre-of-brightness performance, mentioned in Section 2.4.2.1. Their specific value of the steady-state dispersion of b_c was defined so that the overall error dispersion in the Sun would be 25% of Apophis' apparent radius, while being the main contributor of said error, being a reasonable guess based upon GMV's heritage of previous works. The feature tracking white noise error dispersion is assumed to be as large as a pixel, which is coherent with other works [35].

The misalignment errors are constant and around one pixel, while the pointing error of the SC is around 16% of a pixel [58].

5.1.3 Apophis' Surface Model

Whether doing feature tracking or measuring the distance between the SC and Apophis, a surface model is necessary to perform both tasks, since the features are located at the surface and the altimeter measures the distance between the SC and the surface. For this reason, it is relevant to understand what assumptions were made regarding Apophis.

5.1.3.1 General Apophis Surface

An asteroid surface is usually rugged, and Apophis is no exception [44]. To simulate the uneven surface in Apophis, a Perlin noise was introduced into the surface height, since this type of correlated random noise was precisely developed for giving texture to objects [60].

The resultant surface model can be seen in both 3D and in a 2D projection in Fig. 5.7, where the maximum error is 6% of Apophis' radius.

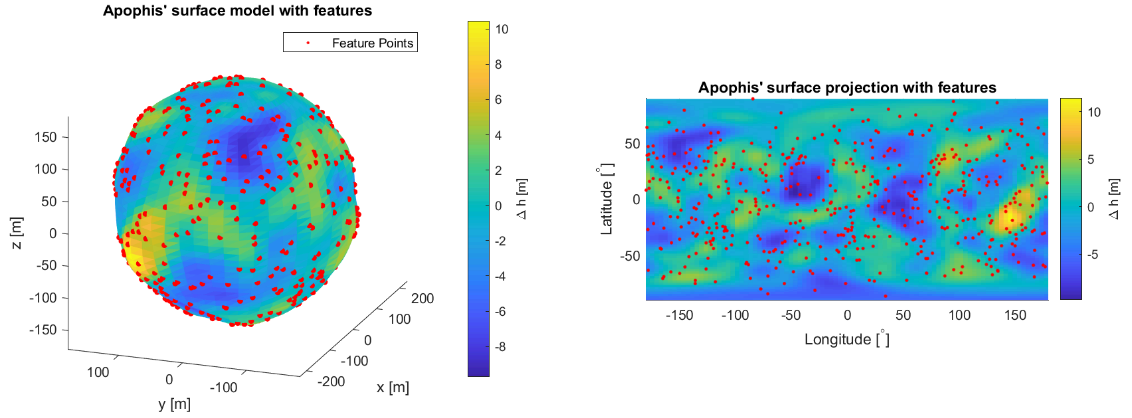

(a) 3D view.

(b) 2D projection.

Figure 5.7: Views of Apophis surface model, with features points.

Besides the true surface model, one other parameter must be discussed. The altimeter measurements, as mentioned in Section 2.4.1, were not simulated as the intersection between the noisy models and the projected ray, but instead the intersection of the ideal model plus a FOGM bias. This abstraction comes down to runtime reasons: the perfect model intersection can be solved in a small set of steps (2.34), while the intersection with the noisy model would consist in solving a set of linear equations that scale proportionally to the number of surfaces, and then process those results [61].

5.1.3.2 Feature Points

The last point to address regarding the surface of Apophis are the features and their localization on Apophis, a critical component in the performance of the feature tracking procedure and, therefore, Apophis' attitude estimation. The features' localization, presented in Fig. 5.7b, were obtained by uniformly sampling points across the Apophis' sphere surface. After having their latitude and longitude, their height was corrected so that they would match the perturbations of the surface, defined in Section 5.1.3.1. This was done by intersecting the noisy model with a ray of corresponding elevation and azimuth, using the Möller–Trumbore intersection algorithm [61] with an already available MatLab implementation [62].

5.2 Filter Parameters

With the environment set up, it is time to consider the parameters of the filter, both constants and initial states.

The assumed dispersions of measurements' errors that define matrix $\mathbf{R}$ (4.19) are shown in Tab. 5.6, where the values were tuned to improve the filter's performance and convergence.

$\sigma(v_l)$ [m]	$\sigma(\mathbf{v}_c)$ $[\%]$	$\sigma(\mathbf{v}_{ft,i})$ [px]	$\sigma(\mathbf{x}_{ft,i})$ [m]
$3\% R_{ap} \times \sqrt{2}$	$5 \times \sqrt{2}$	$\sqrt{2}$	4

Table 5.6: Filter's measurement dispersions, with quantities defined in the measurement equations 4.10

The steady-state covariances and time constants for the FOGM in the filter can be seen in Tab. 5.7, noting that they differ from the real ones as result of rough tuning, so that the performance of the filter would correspond to its estimated uncertainty. Furthermore, it is important to state that, in this case, the time constants for the measurement biases, b_l and b_c, are not relevant in practice, since these states start with their steady-state uncertainties. Unlike all other noise-injected states, the torques are only activated, from 18 to 30 hours after the beginning of the simulation, due to the fact that outside this window their influence is small enough, as seen in Fig. 5.2b.

$\sigma_\infty(b_l)$ [m]	τ_l [h]	$\sigma_\infty(b_c)$ $[\%]$	τ_c [h]
$5\% R_{ap} \times \sqrt{2}$	12	$\sqrt{25^2 - 5^2} \times \sqrt{2}$	12

(a) Measurement biases, described in the measurement equations (4.10).

$\sigma_\infty(\delta^{\mathcal{CI}}\mathbf{a}_{nm,SC})$ [ms^{-2}]	$\tau_{\delta^{\mathcal{CI}}\mathbf{a}_{nm,SC}}$ [h]	$\sigma_\infty(\delta^{\mathcal{AP}}\boldsymbol{\tau}_{nm,AP})$ [rads^{-2}]	$\tau_{\delta^{\mathcal{AP}}\boldsymbol{\tau}_{nm,AP}}$ [min]
8×10^{-8}	12	4×10^{-9}	5

(b) System biases, described in the state dynamics' equations (4.1).

Table 5.7: Filter's system and measurement biases parameters.

The initial dispersions for each state are presented in Tab. 5.8, with the added notes that $\mathbf{P}(0)$ is a diagonal matrix and Apophis' rotational states are only initialized when starting their estimation. When initializing the filters' state, a random sample from a Gaussian distribution with the true state as a mean and $\mathbf{P}(0)$ as covariance is drawn and applied to the filter. The only states that do not follow this rule are the consider parameters, being null regardless of their assumed dispersion, as one cannot know the value of a bias error that is not estimated.

All other environment constants present in the state (4.1) and measurement (4.10) dynamics are assumed to be fully known. Therefore, their are initialized with their real values.

Finally, our tasks imply the existence of different filters taking different measurements. Table 5.9 summarizes them, with the previous information applying to all of them. The name of the filters is derived from their inputs, with 0 representing an ignored measurement, 1 an accepted one, with the order being altimeter, centroiding, features pixels and features' known positions for initialization, respectively.

Filters FIL 1100, 1110 and 1111 will be employed to answer the first two questions outlined in Sec-

$\delta^{\mathcal{CI}}\mathbf{x}_{SC}$ [m]	$\delta^{\mathcal{CI}}\mathbf{v}_{SC}$ [ms^{-1}]	$\delta^{\mathcal{CI}}\mathbf{a}_{nm,SC}$ [ms^{-2}]	δb_l [m]	δb_c [%]
100	10^{-3}	2×10^{-8}	$5\%R_{ap} \times \sqrt{2}$	$\sqrt{25-5} \times \sqrt{2}$

(a) Translational states and measurement biases, defined in Tab. B.1.

$\delta\boldsymbol{\theta}$ [deg]	$\delta^{\mathcal{AP}}\boldsymbol{\omega}_{AP}$ [μdegs^{-1}]	$\delta^{\mathcal{AP}}\dot{\boldsymbol{\tau}}_{nm,AP}$ [rads^{-2}]	σ_{shape} [m]
1	100	10^{-11}	$0.1/60$

(b) Rotational states and features, defined in Tab. B.1 and in Section 4.1.5.1, respectively.

Table 5.8: Initial states' dispersion.

Filter	y_l	$\mathbf{y}_c$	$\mathbf{y}_{ft,i}$	$\mathbf{x}_{ft,i}$	β_{ft}	n_{ft}
FIL 1100	Yes	Yes	No	-	-	-
FIL 1110	Yes	Yes	Yes	No	75	10
FIL 1111	Yes	Yes	Yes	Yes	10	10
FIL 0100	No	Yes	No	-	-	-
FIL 0110	No	Yes	Yes	No	75	10
FIL 0111	No	Yes	Yes	Yes	10	10

Table 5.9: Different filters

tion 1.2, while filters FIL 0100, FIL 0110 and FIL 0111 will test the possibility of discarding the altimeter as a sensor, meeting the third task objective. The filters with known feature tracking have a double purpose: beyond evaluating the performance of this method, even if as an hypothetical, will also act as an upper bound in performance to the proposed solution. Not using feature tracking acts, in turn, as a lower bound.

5.3 Simulation Results

With both theory and implementation laid out in the previous chapters and sections, the presentation and analysis of the results obtained can be done, going firstly through each measurement combination individually and then comparing them all, building and validating all possible choices before analysing their relative strengths and weaknesses.

Moving forward, all Monte Carlo plots will have three components: the individual runs marked by solid blue lines; the nominal run, this is, with the filter initial states equal to the real ones, marked by a solid green line, and three times the dispersion, 3σ, of the nominal run for the given state marked by a red dashed line. If feature tracking is enabled, a double-headed arrow will mark the beginning and end of this kind of measurement. Moreover, normalized error plots will also be present, allowing to effectively see, for each run, if the error exceeds the 3σ mark.

The value of three times the dispersion of an Gaussian distribution, 3σ, is important, because the probability of a sample having its distance to the mean larger than 3σ is around 0.3%. Therefore, results outside of this interval might indicate issues with the filter's prediction and are worth discussing.

One of the assumptions made during the problem statement, in Chapter 4, was that the number of already initialized features would be larger than 5 after the start of the feature tracking measurements.

This condition was verified for all the relevant filters, and a plot of the features tracked over time is available in Fig. C.2.

Finally, the initial states errors and process noises were seed controlled, this is, when comparing the Monte Carlo run n^{th} of FIL 1110 with the respective n^{th} Monte Carlo run for FIL 1111 the initial errors and noise evolution are exactly the same, resulting in the possibility of a direct comparison between each filter in equal conditions. This also means that the evolution of consider parameters is the same for all filters, and Fig. C.1 collects all correspondent plots.

5.3.1 Individual analysis

In this section each filter response will be qualitatively analysed, showcasing the main characteristics of their estimated errors and uncertainties, while verifying the filters' behaviours, paving the way to a proper comparative analysis, where their performances are more scrutinized.

5.3.1.1 Filter 1100

The first filter to be evaluated is the most simple one, employing an altimeter and centroiding measurements to estimate the SC position and, therefore, without the estimation of the rotational states of Apophis.

The SC's position error in $\{\mathcal{RAC}\}$ can be seen unnormalized in Fig. 5.8a, while the normalized error can be found in Fig. 5.8b. The respective dimensioned/normalized pair for the velocity states can be seen in Fig. C.3 and the SC's pointing errors can be seen in Fig. C.4.

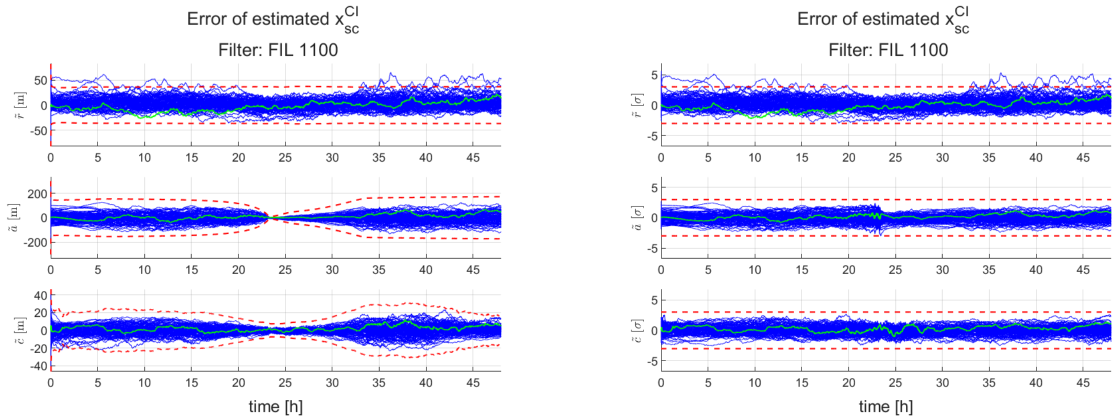

(a) Errors.

(b) Normalized errors.

Figure 5.8: FIL 1100 position estimation errors.

The results present in Fig. 5.8a show several trends: to start, the radial dispersion sits constantly after the initial convergence at around 36 m, coinciding with the altimeter bias dispersion value assumed by the filter. This is expected, since the only depth measurements available are the altimeter ones and, therefore, the filter cannot reduce the uncertainty of the measurement and, consequently, the state.

The second trend is the rapid decrease in both along and cross position errors between 22 and

26 hours. This decrease might seem contradictory with the nature of the centroiding measurement, responsible to indirectly measure these states, at first, but one must recall the decrease of the bias multiplier value at the close approach, shown in Fig. 5.5, and the fact that the bias is, indeed, the larger contributor of the measurement uncertainty, both due to the fact that is significantly larger than the white noise in magnitude and because it cannot be filtered by the filter due to a lack of observability. After the decrease mentioned, the errors in both axes grow and stabilize after 5 hours.

Some comments about the filter covariance estimation must be made. For the most part, in all runs the error stayed below 3σ, showing that the filter can successfully take into account the uncertainties of the system. However, at the start and end parts of the mission, some filters present a radial error above that of the expected. The reason for this error is connected to the same phenomena discussed during the features initialization: a relatively large pointing error will lead to depth measurement differences caused by the curvature of Apophis, leading, consequently, to measurements that would indicate a higher distance to the target, which is exactly what is observed in Fig. 5.8b.

5.3.1.2 Attitude Propagation

One major aspect of the proposed solution is Apophis' attitude estimation. To understand how relevant its inclusion as an estimated parameter is, instead of only propagating it, Fig. 5.9a and Fig. 5.9b show the results of the pure propagation in the time-frame that feature tracking is enabled, for both attitude and angular velocity, respectively.

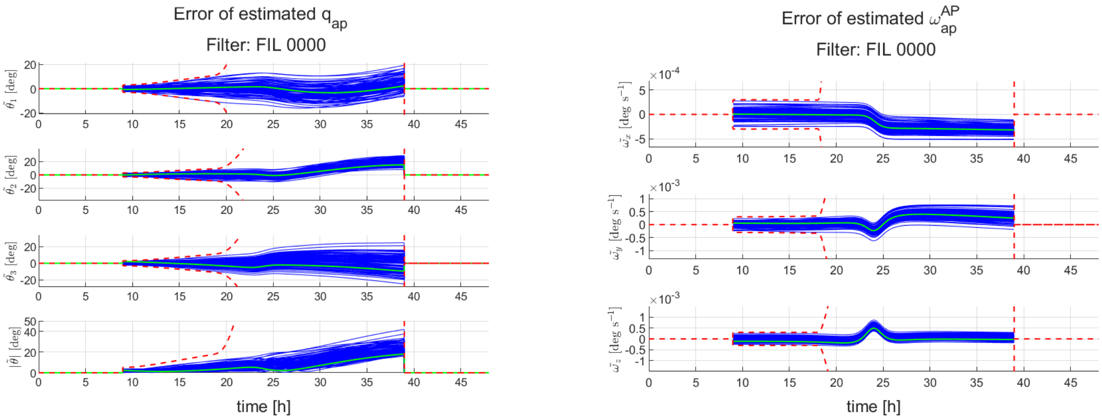

(a) Attitude.

(b) Angular velocity.

Figure 5.9: Pure propagation estimation errors.

The results show a constant growth of the attitude error until the 23 hour mark, followed by a disruption that increases the bias of the estimation and further diverges the different propagations. A similar disruption can be seen in the angular velocity propagation, in Fig. 5.9b, leading the components of the angular velocity to present a systematic error, even if it does not increase the dispersion of the estimations. These results showcase how uncertain the dynamics without a proper modelling of the gravitational torques, with the attitude propagation reaching errors of up to 40 degrees.

5.3.1.3 Filter 1111

The filter FIL 1111 uses all available measurements: altimeter, centroiding and feature tracking. In addition to those, the filter also assumes that there is a database of features already stored, and, for this reason, when a feature is detected, its initialization is done by ground and not by self-initializing, or bootstrapping. This can be seen as a solution to a relaxed version of this thesis problem, where the feature localizations are known.

The SC's position error in $\{\mathcal{RAC}\}$ can be seen unnormalized in Fig. 5.10a, while the normalized error can be found in Fig. 5.10b, with the former showing interesting results worth discussing, bringing in light to the impact of the feature tracking measurements. The respective dimensioned/normalized pair for the velocity states can be seen in Fig. C.5 and the SC's pointing errors can be seen in Fig. C.6.

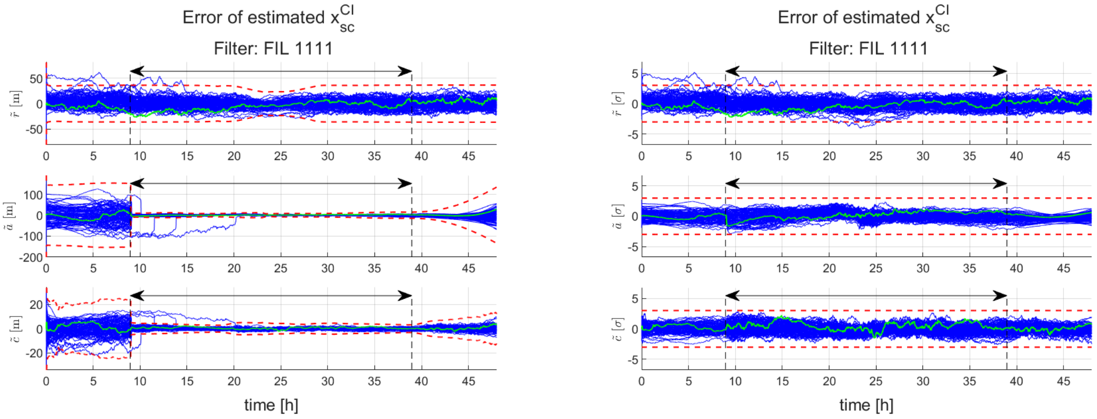

(a) Unnormalized errors.

(b) Normalized errors.

Figure 5.10: FIL 1111 position estimation errors.

Starting with the radial direction errors, the first thing to notice is that there is not a significant change when transitioning between only centroiding and centroiding plus feature tracking, with only a slight decrease in expected covariance in between 20 and 28 hours after the start. This result was expected, since the monocular camera does not produce 3D measurements of the features' positions and, due to this, the feature tracking measurements are also not 3D, resulting in their uncertainty on the radial direction being mostly maintained. The decrease can be attributed to the larger angular distance between features in relation to the camera, as it can be observed in Fig. 5.3a, which increases the depth information. Regarding the normalized errors, only one case reaches the 3σ limit. However, this error is relatively small and is caused not by the increase in error but the previously mentioned small decrease in covariance when the SC is closer to the target. Moreover, the previously seen radial errors with FIL 1100 are not present any more, supporting their origin as due to pointing errors.

The along and cross directions show a different reaction than the radial direction, presenting marked improvements in both error and filter covariance. These changes are almost immediately noticeable, with the filter's covariance dropping by around one order of magnitude in less than half an hour. Once feature tracking is no longer available, the covariance and error of the filter start increasing due to the loss of the precise measurements and uncertainty in velocity, albeit slowly. All errors are within the 3σ

boundary and, therefore, within the expected margin.

With this said, four cases clearly stand out from the rest in Fig. 5.10a, maintaining their relatively large errors until they eventually converge, but do not stand out in the normalized error, as observable in Fig. 5.10b. This indicates that for these four cases the appearance of features on the filter state vector is delayed, only being able to acquire them much later than when they start becoming available and, in the meantime, only resort to the centroiding and altimeter measurements. The next question, then, is why are the features not being used if the measurements are supposed to be available. The answer to this question lies in the initial pointing error that both cases present, alongside the hard limit imposed to the feature prediction error, with Fig. 5.11 providing a rendering of the camera scene in one of the runs when this phenomena is occurring.

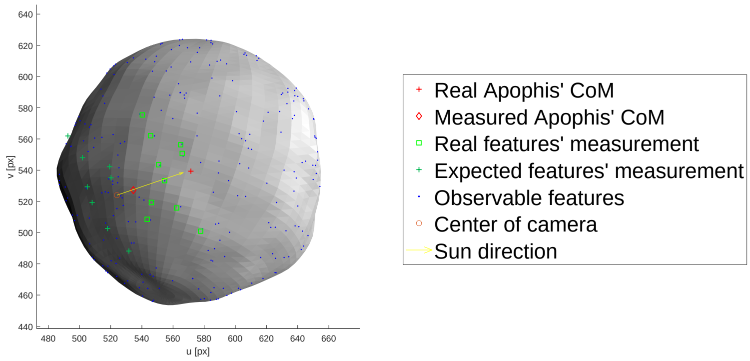

Figure 5.11: Camera rendering of an outlier case, at $t = 12$h.

Recalling the feature handling procedure in Section 4.1.5.1, the first time a feature is captured the measurement is only used to initialize it, and only subsequent measurements of the same feature contribute to the correction of the remaining estimated states. However, if the relative position between the SC and Apophis is so large that the predicted position of feature tracking measurement error surpasses the interface limit, the feature is discarded and re-initialized again, never contributing to the improvement of the desired states. The described effect can be seen in Fig. 5.11, where the SC believes that is pointing at the centre of Apophis and, therefore, predicts that the features will be in the vicinity, while their actual position is significantly distant. This effect can only exist for the case of known features, since that their initialization is not based on the measurement orientation but instead on the their known position on Apophis' surface.

Unlike with the filter FIL 1100, in this case there is an estimation of Apophis' rotational states, namely attitude and angular velocity, with their plots being presented in Fig. 5.12 and Fig. C.7, respectively.

The results of Apophis' attitude estimation error for each axis are complex to comment, since there is no intuitive relation between them and the nominal attitude, with the only remarkable note being that for all axes the error remains inside the 3σ boundary. Instead, the analysis of the total attitude error, $||\delta\boldsymbol{\theta}||$, provides a better insight of the filter's performance. This error shows that the overall attitude covariance remains fairly constant throughout the mission, having small ups and downs. The error also accompanies this evolution, noting that between the 24 and 32 hour marks it is smaller than the initial

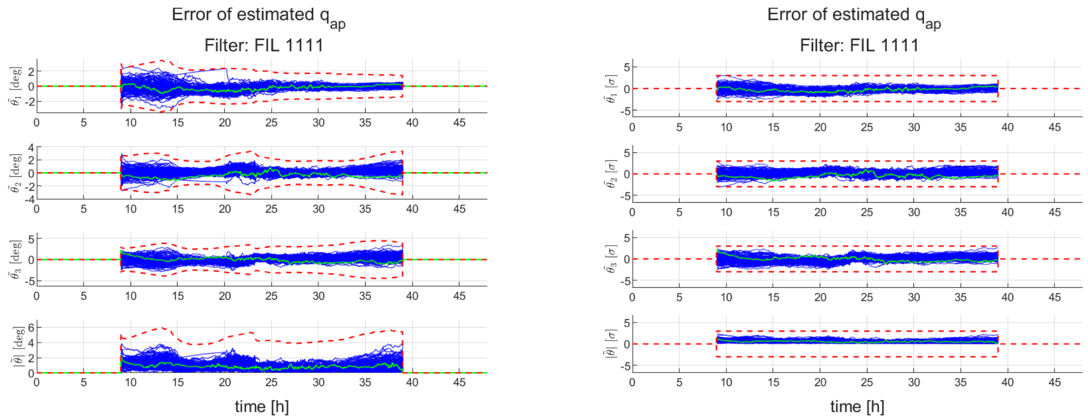

(a) unnormalized errors.

(b) Normalized errors.

Figure 5.12: FIL 1111 Apophis' attitude estimation errors.

error, and after this period it slowly rises. One explanation to this decrease in error can be found in the fact that, for smaller distances, the measurement of the feature tracking algorithm is smaller position-wise than it would be at bigger distances, since the angular error, i.e., the orientation error, is the same. In turn, this smaller measurement error of the features leads to smaller uncertainties and errors in the features' positions, resulting in a better estimation of Apophis' attitude, since it is indirectly measured by the features' relative positions.

5.3.1.4 Filter 1110

The filter FIL 1110 is the complete implementation of the proposed solution to the full problem, assuming the need for altimeter measurements: it is similar to filter FIL 1111, however it does not rely on a stored database of features, and instead bootstraps it features.

As it was done with the previous filter analysis, the SC's position error of all runs was plotted, being presented in Fig. 5.13, and velocity errors in Fig. C.8. The SC's pointing errors can be seen in Fig. C.9.

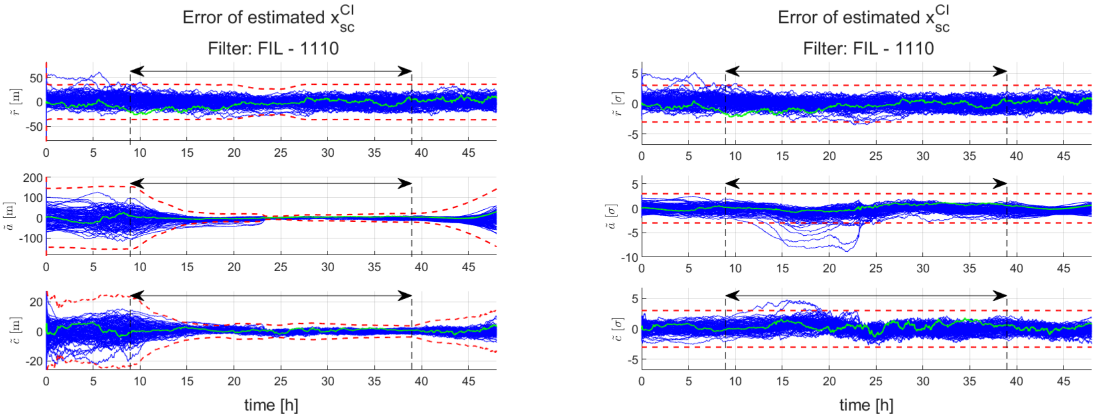

(a) Dimensionaized errors.

(b) Normalized errors.

Figure 5.13: FIL 1110 position estimation errors.

The radial position estimates' errors do not significantly change in magnitude with or without the feature tracking measurements, which goes in line with the observation made of the FIL 1111 performance in Section 5.3.1.3. Once again, there is a small decrease in the predicted error uncertainty around the 24 hour mark and one run crosses the 3σ threshold. However, this error is relatively small and comes not from an increase in the actual error but from a decrease in the state covariance.

The along and cross position errors show a different behaviour than the radial errors, with both showing a decrease in error and filter variance magnitude. This reduction is made gradually, however, taking around 8 hours for the filter to stabilize, with this delayed convergence being the result of underweighting the measurements certainties in order to mitigate non-linear issues. Moreover, the normalized errors in Fig. 5.13b show a non-trivial number cases where the along position error are larger than 3σ, with four cases standing out and being the ones that caused issues to FIL 1111.

The overconfidence in the position estimation is the result of the nonlinear nature of the relationship between the feature's position and SC's position, alongside a large initialization error. Although this behaviour of the features' uncertainties is partially taken in consideration by the methods detailed in Section 4.1.5.1, where it is thoroughly analysed, it is important to note that the cross-correlation between the feature's positions and remaining states is still fully linearized. This approximation may, in turn, lead the filter to misrepresent the actual error covariance, causing overconfidence on the filter's part for both quantities. The underweighting implement was intended to counter the erroneous evolution of the uncertainty estimation. In spite of the relatively large underweighting used, however, it can be seen that it was not completely successful in mitigating the filter's overconfidence for the cases with the largest position error at the features' initialization time.

Another solution to the features' position overconfidence would be the inclusion of estimated FOGM for the features' positions. This solution would add noise that could compensate the nonlinear relationship, opening the possibility for the filter to properly converge. However, the implementation of a FOGM for estimation requires a careful, complex and computationally heavy tuning procedure that fell outside of the scope of this thesis.

With this said, it is important to consider the quantities involved in the problem: the pointing error of the four cases ranges from 0.6 to 0.8 degrees. The minimum angular error corresponds to a tangential error of more than 83 m, corresponding to $49\ \%$ of Apophis' radius, invalidating the linearization performed when first initializing the features. The nonlinear effects of position uncertainty in the feature position can be seen by the size of the radial error dispersion on Fig. 4.2a, where, if the relationship was linear, the radial error would be always 0. Regardless of the strong non-linearities when initializing, it can be seen that the inclusion of features still improves the filter's performance and, after 24 h, the features are well positioned enough that the SC's position overestimation no longer happens.

Moving from the translational states analysis, the estimated attitude error of Apophis can be seen in Fig. 5.14a and Fig. 5.14b, while its angular velocity error can be seen in Fig. C.10.

The attitude errors remain mostly constant in both θ_1 and θ_2, with a slight increase in covariance as time goes by. The variable θ_3, however, presents significant shanges, with a steady increase in error and a perceived uncertainty, reaching, respectively, 5 and 7 degrees, respectively, discounting the

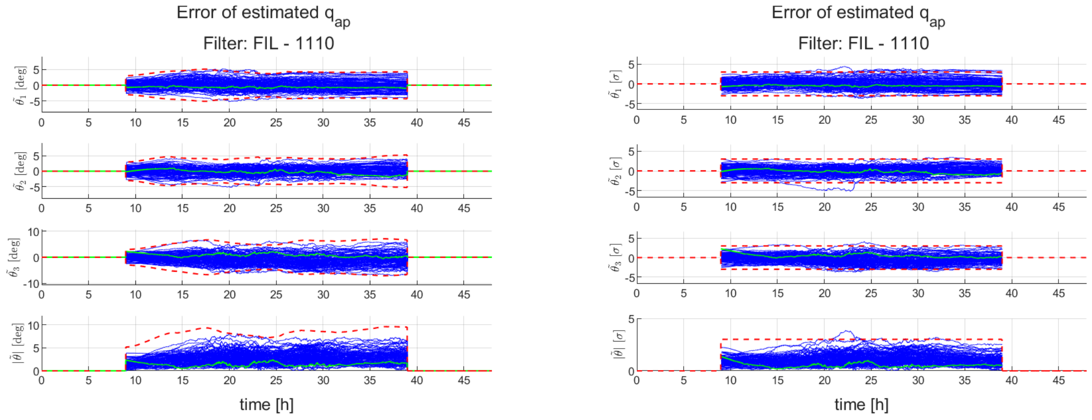

(a) Dimensionaized errors.

(b) Normalized errors.

Figure 5.14: FIL 1110 Apophis' attitude estimation errors.

outlier cases. The absolute error reflects the evolution of the previously mentioned components, growing slightly across time. Regarding their normalized errors, most stay within the 3σ range, with one persistent exception in θ_3 and θ_1 and sporadic approximations of some runs. The two cases in which the filter does not properly account for the attitude uncertainty are part of the four outlier cases and, therefore, are not completely unexpected, since the overconfidence in the features' positions also affects the confidence in Apophis' attitude.

Before moving to the next filter, it is relevant to discuss the lack of improvement in the attitude estimation across time, recalling the fact that the filter with known features FIL 1111 had an improved attitude estimation when the SC got closer to Apophis. The Filter FIL 1110 only receives an unbiased measurement of Apophis attitude at the initialization of the rotational states; notice that the feature self initializations are biased in relation to the SC position. From that initial time step, the only measurements that the filter intakes are from the feature positions that, as said previously, have an initial bias not exactly modelled, due to non-linear relationship present in the feature initialization. Additionally, the features first initialized are eventually unavailable and replaced by newly bootstrapped features, resulting in the loss of information previously held by the state vector. All these factors contribute to a degradation of Apophis' attitude estimation.

5.3.1.5 Filter 0100

The filter FIL 0100 is the first possible combination of measurements without the employment of an altimeter, using just the centroiding measurements.

The SC's position errors are showcased in Fig. 5.15a and Fig. 5.15b, where the absolute error and normalized errors can be seen, respectively. The dimensioned/normalized pair for the error of the SC's velocity state can be seen in Fig. C.11. The SC's pointing errors can be seen in Fig. C.12.

The first noticeable change is comparison to the results of its altimeter-abled counterpart, FIL 1100 seen in Section 5.3.1.1, is the significantly worse performance of the radial estimates, not being able to, for the first 18 hours, reduce its initial uncertainty. This result was expected, since FIL 0100 has

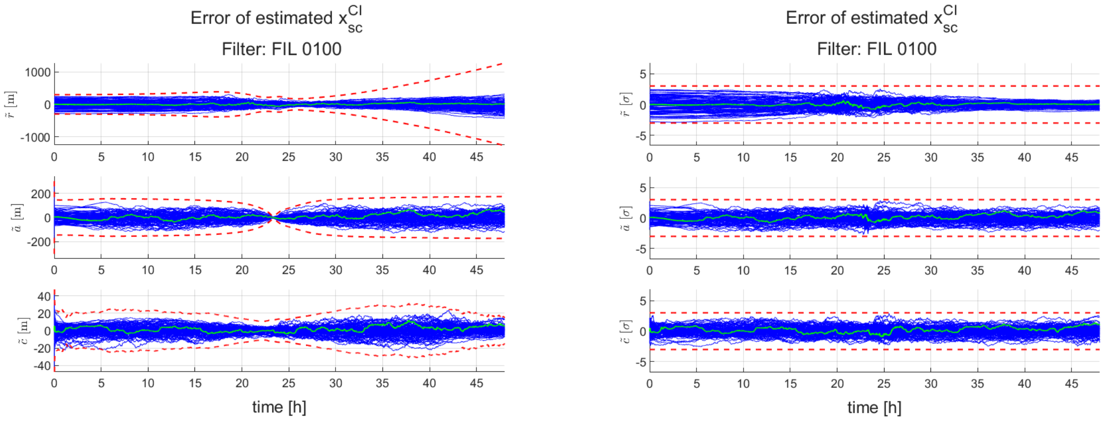

(a) Dimensionalized errors.

(b) Normalized errors.

Figure 5.15: FIL 0100 position estimation errors.

no altimeter and, therefore, cannot measure its relative distance to Apophis surface. However, there is a decrease in the uncertainty of its radial position from the 18 hour mark, with a minimum at 22 and half hours, followed by a small increase until 24 hours. It reaches its minimum value at around 25 and half hours and, from there, grows quadratically. This decrease in uncertainty can be attributed to the fly-by orbit around Apophis, with relatively similar orbits coalescing at the nominal periapsis, but afterwards scattering, leading to the large grow in uncertainty. Moreover, due to the fast angular variation of the SC position in $\{\mathcal{CI}\}$ at the SC close approach, the radial component is inferred from the along and cross track direction of the previous estimation steps without degradation of performance due to the process noises, further contributing to the decrease in the estimated radial error dispersion around this time. The error, however, is fairly constant throughout the simulation, with a small decrease 18 hours after start and increasing again, slowly, at the 25 and half hours mark. Therefore, the filter considerably overestimates its radial error from 30 hours onwards.

The along and cross directions present a different evolution, with the filter able to reduce in the same way FIL 1100 can at the start of the mission. This error remain fairly stable until the SC's fly-by of Apophis, with the uncertainty and error of the along position finding a minimum at 23 hours and the cross a bit earlier, at 22 hours. However, this decrease is short-lived, with the along error growing and stabilizing around the previously stable errors and uncertainties at the 30 hour mark, with the same effect being visible in the cross position error. For both directions the filter's uncertainty portraits correctly the error, neither over nor underestimating it.

5.3.1.6 Filter 0111

The filter FIL 0111 represents the case where the features tracked are known, but no altimeter is employed.

The SC's position errors are showcased in Fig. 5.16a and Fig. 5.16b, where the absolute error and normalized errors can be seen, respectively. The dimensioned/normalized pair for the error of the SC's velocity state can be seen in Fig. C.13. The SC's pointing errors can be seen in Fig. C.14.

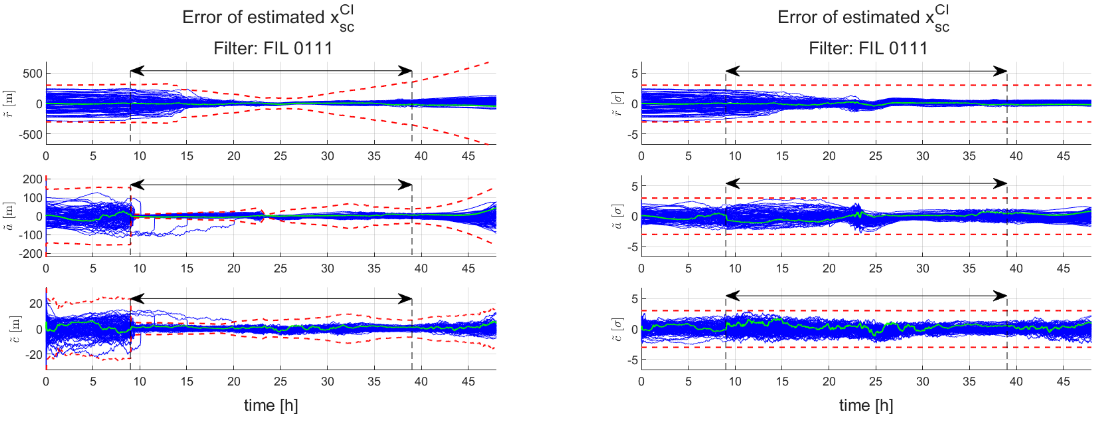

(a) Dimensionalized errors.

(b) Normalized errors.

Figure 5.16: FIL 0111 position estimation errors.

The first noticeable difference in the radial position errors, comparing with FIL 0100, is the earlier decrease after the introduction of features tracking measurements. However, this decrease is slow and only starts 5 hours after the introduction of the features, which could be due to the fact that, at closer distances, the features are further spread apart. This larger spread contributes to the relative orientation vectors of each feature, measured by the camera, having a larger relative angle, contributing in turn to a larger observability of the 3D space, even with a monocular camera. A similar effect was observed in the results of FIL 1110 and FIL 1111. However, the contribution was smaller in the previous cases due to the better altimeter measurements. The filter keeps its radial uncertainty estimate above the actual error, noting that, from the 25 hour mark onwards, the uncertainty estimated by the filter grows much faster than the actual error, i.e., the filter overestimates its uncertainty.

The along and cross directions show an immediate reaction to the feature tracking measurements, reducing them significantly in a short span of time, showing similarities with the behaviour of FIL 1111, its counterpart. However, there are also differences in their evolution, with the covariance of the along position increasing slowly from 19 to 23 hours after the mission start, falling sharply until its smallest value at 23 and half hours, slowly rising again until 32 hours, at which time it reduces slightly until the end of the feature tracking measurements, after which it grows until the end of the simulation. The covariance of the cross position is more stable, with a steady increase from the beginning of the feature tracking measurements up until 32 hours. Afterwards, it slowly decreases until it has only centroiding measurements, slowly rising from that point on. These results show an interesting phenomena, with the filter improving its tangential error even if the radial error is large. The filter has better grasp on the uncertainty of these two states, with the 3σ plot showing a smaller uncertainty overestimation without the filter falling to underestimating its errors.

Once again, the same four outlier cases can be found, reinforcing the notion that their appearance comes from an error in the along and cross positions instead of a radial error, as explained in Section 5.3.1.3.

Moving to the rotational states, the Apophis' attitude estimation errors can be seen in Fig. 5.17a and

Fig. 5.17b, while the rotational velocity errors are presented in Fig. C.15a and Fig C.15b.

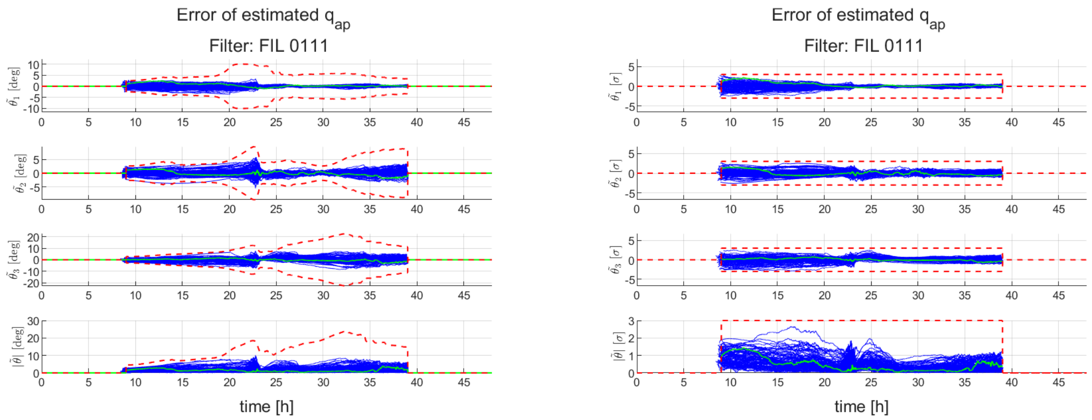

(a) Dimensionalized errors.

(b) Normalized errors.

Figure 5.17: FIL 0111 Apophis attitude estimation errors.

The evolution of the attitude error of Apophis is not as simple to explain as it is in FIL 1111. For the case under analysis, it can be seen that it has several increases and decreases, notably, quick decreases at 23 and 28 hours, both followed by increases that, overall, raise the attitude error. The main axis of uncertainty is θ_3, which is expected, since the nominal angular velocity has a larger z component, observable in Fig. 5.6b. The filter starts by estimating the states uncertainty correctly, but after the 20 hour mark it overestimates its error, especially in θ_1 and θ_3.

5.3.1.7 Filter 0110

The last filter individually analysed, FIL 0110, is a modification of proposed solution to the problem made, where the measurements are further limited to the ones that a camera can provide.

As it was done with the previous filter analysis, the SC's position error of all runs was plotted, being presented in 5.18, velocity errors in Fig. C.16, and pointing errors in Fig. C.17.

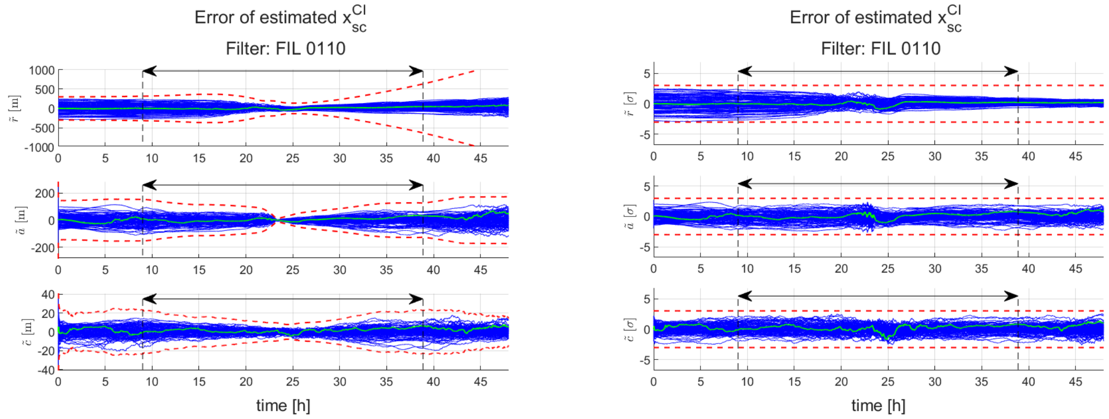

(a) Dimensionaized errors.

(b) Normalized errors.

Figure 5.18: FIL 0110 position estimation errors.

Starting with the radial position estimates' errors, it can be seen that the introduction of self-initialized features does not make a substantial difference, with the results of FIL 0100 in Fig. 5.15a as reference, resulting only in a slower increase in uncertainty after 25 and half hours, with the estimated uncertainty being much larger than the real error for this variable, after 30 hours from the beginning.

The along and cross position errors show a small and gradual reaction to the introduction of the features, reducing the expected uncertainty. Once these errors reach their minimum at 24 hours, the feature tracking allow the errors and uncertainties to grow slower than compared to FIL 0100. The filter is able to estimate the state's uncertainty correctly, as it can be seen in Fig. 5.15b.

Moving from the translational states analysis, the estimated attitude error of Apophis can be seen in Fig. 5.19a and Fig. 5.19b, while its angular velocity error can be seen in Fig. C.18.

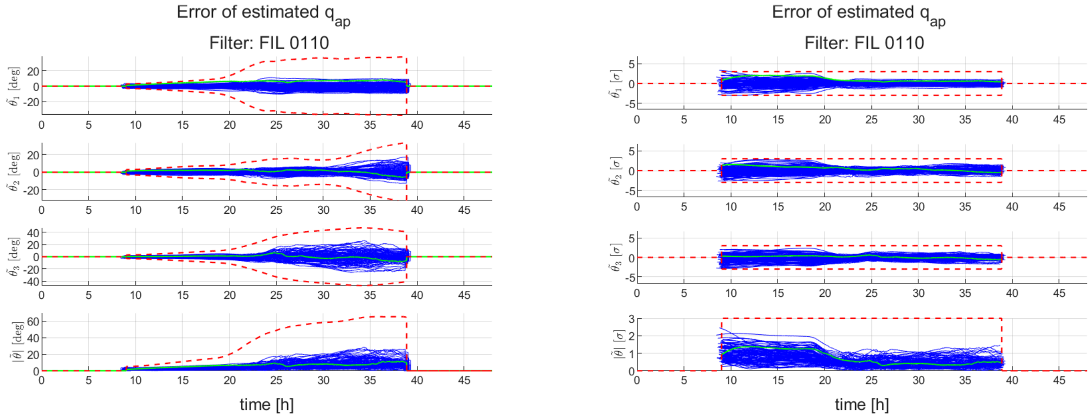

(a) Dimensionaized errors.

(b) Normalized errors.

Figure 5.19: FIL 0110 Apophis attitude estimation errors.

The attitude errors can be seen to increase through time, with an accelerated rate after 25 hours. The poor performance of the attitude tracking can be attributed to the poor position estimation: since the features are bootstrapped, their covariance is partially inherited from the SC own position uncertainty. This leads to features whose positions are highly uncertain and, therefore, their contribution to the attitude estimation being minimal.

5.3.2 Comparative Analysis

After all filter individual performances reviewed, it is possible to compare these solutions in both the SC's position estimation performance and Apophis' attitude estimation, solving the proposed objectives.

When comparing the performance of the filters, two quantities must be judged: the mean and dispersion of its error estimates. Due to this, the examination of the filter's performance might be more complex than just pointing out which one has the lower mean and/or dispersion, being relevant to also look at the relative scale of the parameters. A low mean error might indicate that, on average, the error will be small but if it is accompanied by an high dispersion the individual runs themselves can display a considerable error. This is especially problematic if the task at hand cannot be repeated, as it is the case. However, a low dispersion accompanied by a high mean error is also troublesome, since it results in the filter estimates being consistently wrong.

As seen in the previous section, there are four outlier cases in the filters using feature tracking that, due to the feature tracking initial conditions, do not correctly converge or are not taken into account. These four cases will not be considered moving forward, to better represent the overall performance of the filters in question. However, it is advised to have this problem in mind when considering their implementation.

5.3.2.1 Pointing and Position error

The first question posed was what combination of measurements was better suited to perform the SC's position estimation and, with it, a smaller pointing error. This section will analyse the performances of the different filters proposed in regards to their position and pointing performances.

Figure 5.20a presents the estimated position errors 3σ dispersion values through time for the filters FIL 1100, FIL 1110 and FIL 1111, with Fig. 5.20b presenting a detail of the same plot and Fig. 5.20c showing the mean error evolution for the same quantities. Regarding the mean of the error, there are some notes to make. Firstly, the mean error in the radial direction is generally improved from using features, be it known or unknown. There is an oscillating behaviour between 20 and 25 hours for both

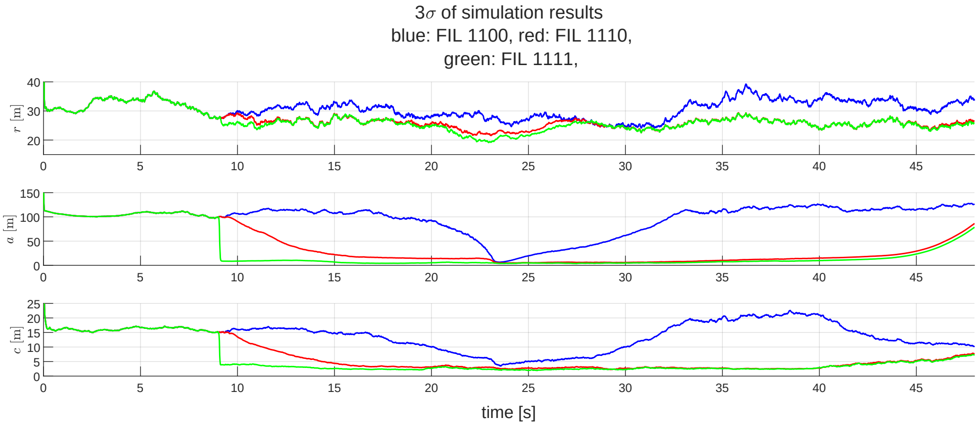

(a) Filters' errors covariance plot.

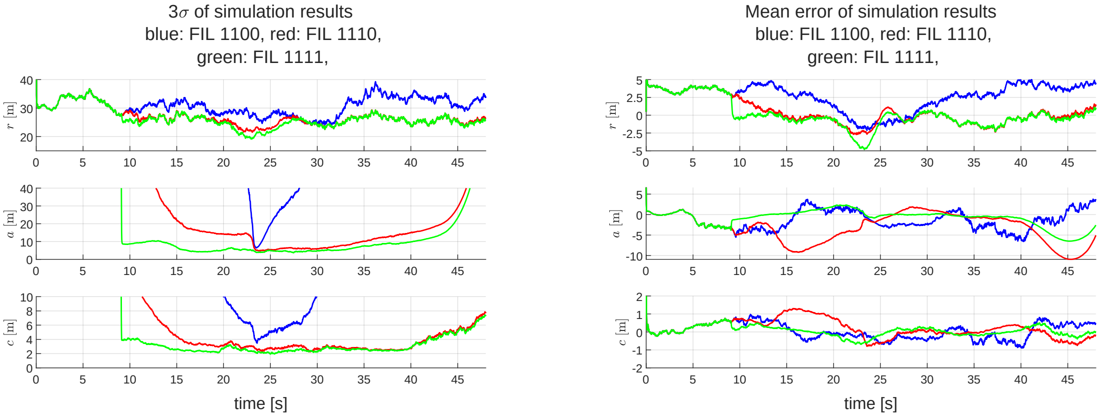

(b) Detail of the filters' errors covariance plot.

(c) Mean of the filters' errors.

Figure 5.20: FIL 1100, FIL 1110 and FIL 1111 estimation errors for the SC position in $\{\mathcal{RAC}\}$.

FIL 1111 and FIL 1110. However, it is relatively small compared to the radial dispersion of both filters. In the along and cross axes, a similar trend can be seen regarding the evolution of the mean error, where the introduction of known features reduced the error but the introduction of unknown features exacerbates it, until reaching the 23 hour mark, at which point it has a similar improvement. The reason for the initial increase in mean error of FIL 1110 has already been hinted when discussing its outliers: the bootstrapped features will inherit the SC along and cross position error. Due to the nonlinear relationship between the two errors, already reviewed in Section 4.1.5.1, the filter does not correctly take into account the error, and the error bias appears. However, in both axis, this error is within the dispersion values.

It can be seen that the dispersion of the errors on the cross and along axes are significantly reduced once feature tracking measurements are employed. This is an already established result from the analysis of the individual cases, but Fig. 5.20a further reinforces this notion. The radial error dispersion is also reduced, albeit not as much. The relative improvement of the dispersion can better be seen on Fig. 5.21a and Fig. 5.21b, where FIL 1110 is compared to FIL 1100 and FIL 1111 to FIL 1110, respectively.

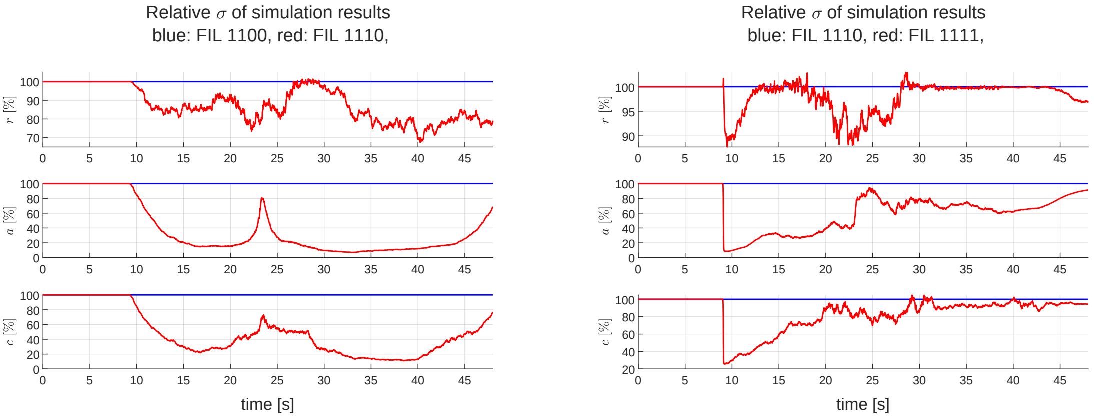

(a) FIL 1110 in respect to FIL 1100.

(b) FIL 1111 in respect to FIL 1110.

Figure 5.21: Relative SC position errors dispersions for different filters.

The results presented in Fig. 5.21a show a overwhelming improvement in both along and cross position error dispersion. In these axes, the first improvement, before the SC's close approach, reaches 80, meaning that the dispersion of the errors of FIL 1110 are 5 times smaller than that of FIL 1100. During the close approach, this performance increase is decreased to 20%, but in the time frame of 2 hours it reaches the 80% mark again and reaches 92 in the along direction, only surpassing it again at 44 hours, five hours after the feature tracking is no longer used. The cross axis error takes more time to improve, but at 30 hours it comes close to 20, and starts increasing once 40 hours have passed since the beginning of the simulation. The radial direction also presents improvements in the error dispersion, although not as much as in the other two directions.

Even with the gains already commented, FIL 1111 can achieve even better results than FIL 1110, as is showcased in Fig. 5.21b. The largest gain occurs during the first half of the mission, which is expected due to the underweighting of the feature measurements in FIL 1110. However, once the SC has been close to Apophis, the relative gain in error dispersion is much lower, with the radial error being almost identical, the along oscillating between 20 and 40%, and the cross track improvement being no larger than 20%.

Moving to the pointing error, Fig. 5.22 presents the 100^{th}, 75^{th} and 50^{th} percentiles of the desired SC's pointing error for FIL 1100, FIL 1111 and FIL 1110.

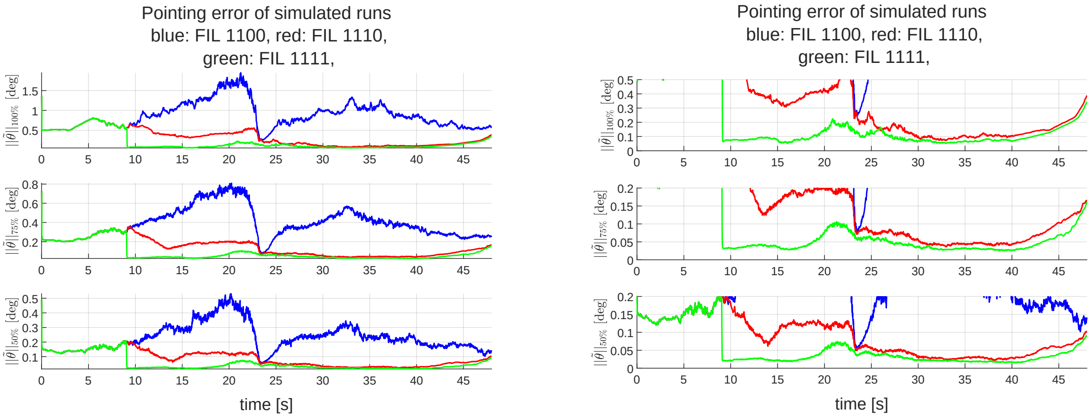

(a) Overview.

(b) Detail.

Figure 5.22: Pointing error percentiles of FIL 1100, FIL 1111 and FIL 1110.

The results presented fit with the performance of the filters in correctly estimating the along and cross positions, with FIL 1100 being the worst performer overall, and FIL 1110 gradually improving its pointing until it reaches similar values to that of FIL 1111 from 24 hours onwards, being about 10 times better than only using an altimeter and centroiding measurements. The relative behaviour of the pointing errors does not vay significantly between percentiles.

With the filters that use altimeters covered, consider Fig. 5.23, where the SC's position errors for FIL 0100, FIL 0111 and FIL 0110 are shown, alongside FIL 1110 for comparison. As was expected, the radial position estimates are worse when not employing an altimeter, both regarding mean and dispersion, with the note that FIL 0111, with known features, has a significantly better behaviour than both FIL 0110 and FIL 0100. The along and cross mean errors present a different picture, showing that the mean errors in both axes are comparable to the ones of their counterparts. However, the dispersion of the filter without altimeter is generally worse when directly comparing to the respective filters with an altimeter. Moreover, the performance of the proposed solution is, in this case, more closer to not using feature tracking at all than to tracking known features.

The error dispersion gain of using the altimeter is clear, with the difference in performance of FIL 1110 and FIL 0110 being evident, as Fig. 5.24a more clearly points out. The filter FIL 0111 can be better than FIL 1110 in the along and cross position dispersion, however, having an initial performance similar to FIL 1111. With this said, the initial gain provided by the known features does not compensate the fact that the depth measurement is missing, and after the 20 hour mark the dispersion of FIL 1110 is always lower than that of FIL 0111.

Figure 5.25 presents the 100^{th}, 75^{th} and 50^{th} percentiles of the pointing error for the filters FIL 1110, FIL 0100, FIL 0111 and FIL 1011. In Fig. 5.25, it can be seen that, once more, the pointing error is

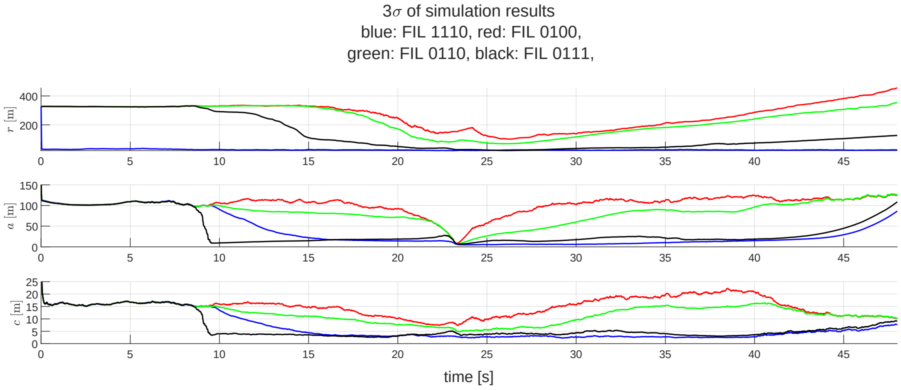

(a) Filters' errors covariance plot.

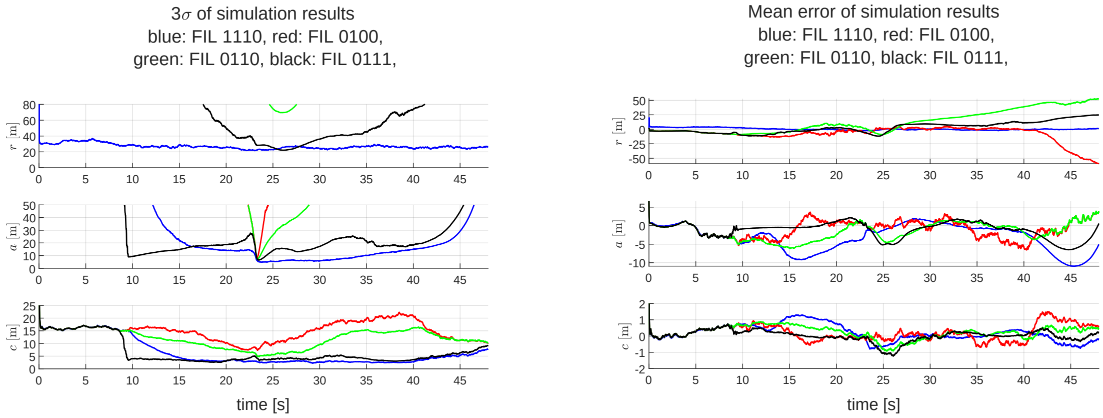

(b) Detail of the filters' errors covariance plot.

(c) Mean of the filters' errors.

Figure 5.23: FIL 1110, FIL 0100, FIL 0110 and FIL 0111 estimation errors for the SC position in $\{\mathcal{RAC}\}$.

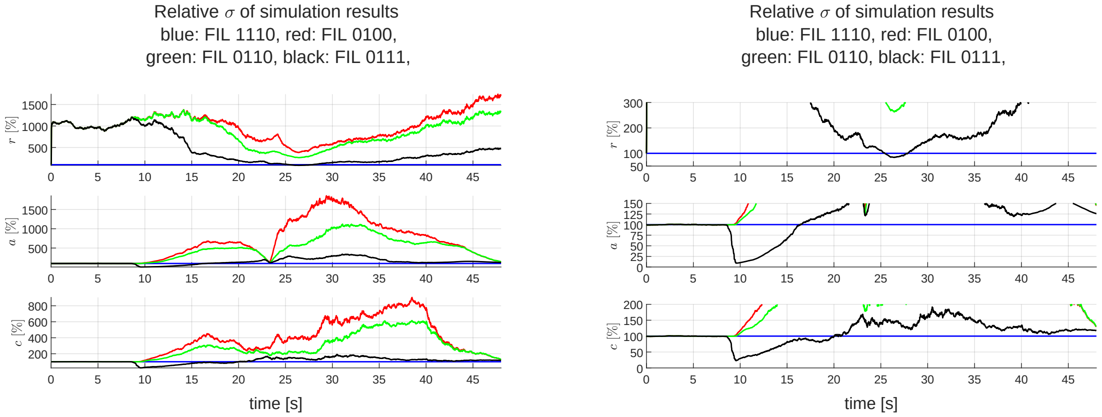

(a) Overview.

(b) Detail.

Figure 5.24: Relative SC position errors dispersions in respect to FIL 1110.

directly related to the along-cross SC position estimation of the filters. FIL 0111 is able to have a better performance than FIL 1110 until 20 hours after start, however, after it it can only be reach its performance at 37 hours. Both FIL 0100 and FIL 0110 are notably worse than the other two filters, only achieving their performance in a short period of time around 23 hours, which is followed by a sharp increase in the pointing error of these filters.

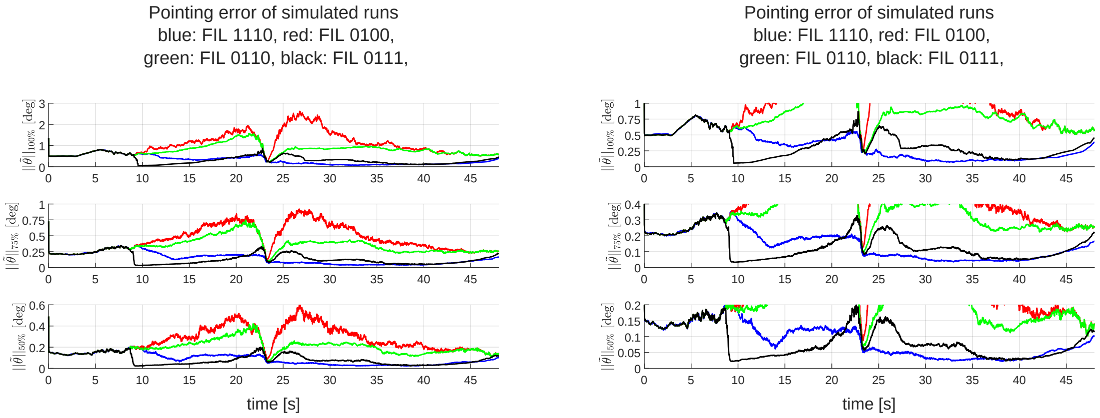

(a) Overview.

(b) Detail.

Figure 5.25: Pointing error percentiles of FIL 1110, FIL 0100, FIL 0111 and FIL 0110.

5.3.2.2 Attitude Error

After analysing the SC's position and pointing errors performance, the next quantity to examine is Apophis' attitude estimation. As it was seen in Section 5.3.1, the attitude error for each axis is not an intuitive quantity to compare. Instead, the focus of this comparative analysis will be on the magnitude of the error of Apophis' attitude estimation.

Figure 5.26 presents the 100^{th}, 75^{th} and 50^{th} percentiles for the Apophis' attitude estimation error, with Table 5.10 presenting the respective filters' errors at 10 and 38 hours. Firstly, it can be seen that the filters start to estimate the attitude of Apophis at different times. This is due to the difference in their estimation of the distance between the SC and Apophis, which results in an earlier or later acceptance of feature tracking measurements, with FIL 0111 and FIL 0110 being the more affected, due to their radial position errors, as discussed in Section 5.3.2.1.

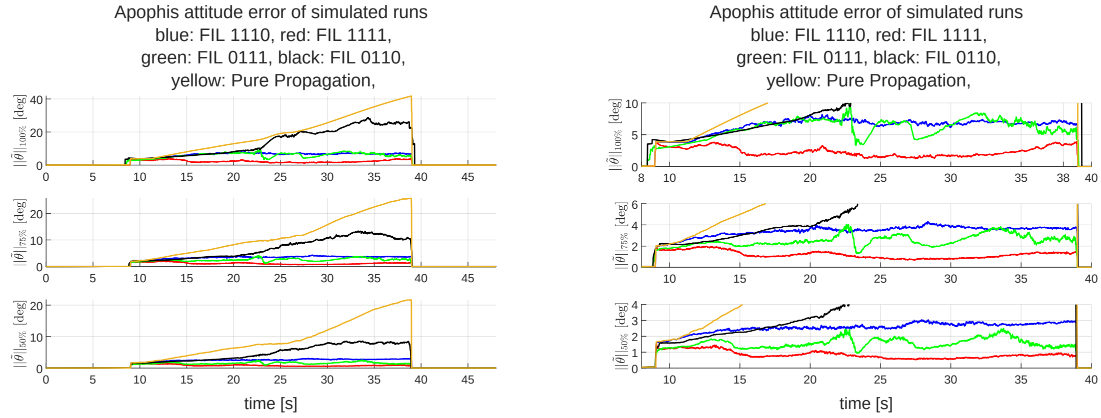

(a) Overview.

(b) Detail.

Figure 5.26: Apophis' attitude estimation error percentiles for different filters.

Regarding the attitude estimation values themselves, it is clear that FIL 0110 is the worst performing in any percentile, with the difference in performance being noticeable from 23 hours onwards. The

Filters	FIL 1111			FIL 1110		
Percentiles	100	75	50	100	75	50
Error @ 10 h	3.07	1.62	1.23	3.84	2.17	1.73
Error @ 38 h	3.32	1.38	0.80	6.29	3.77	2.82
Filters	FIL 0111			FIL 0110		
Percentiles	100	75	50	100	75	50
Error @ 10 h	3.09	1.79	1.27	3.86	2.20	1.58
Error @ 38 h	5.68	2.88	1.36	25.21	10.43	8.01
Filters	Pure Propagation					
Percentiles	100	75	50			
Error @ 10 h	3.87	2.18	1.76			
Error @ 38 h	40.3	25.32	21.2			

Table 5.10: Apophis' attitude error percentiles for different filters, in degrees.

attitude estimation of FIL 1110 is the second worse, albeit ending with less than half of the error of FIL 0110. The results show a slow constant growth of the attitude error throughout time, implying that the cause of this deterioration in estimation is not due to the non-modelled angular accelerations but due to other factors, namely the cumulative effect of non-linearities in the states relationships. Notice, also that, from the 25 hour mark, the attitude error stabilizes, further suggesting that the initial feature initialization error and related non-linearities are the culprits of the initial information loss.

The filters with the known features proved to be the better performing, although FIL 0111 worst case final value is similar to FIL 1110's estimation. FIL 1111 is able to reduce its initial estimate, shown by the reduced final values of its 75^{th} and 50^{th} percentile values, and its estimates has a tendency of decreasing until 30 hours after the start of the mission, at which the errors slowly increase, possibly due to worse feature tracking measurements. The filter FIL 0111 error has an osculating behaviour, with its value lying in between the results of FIL 1111 and FIL 1110.

Finally, it is clear that the estimations of FIL 1110, FIL 1111 and FIL 0111 are clear improvements upon the pure propagation of the rotational states of Apophis, with gains close to one order of magnitude for the filter with bootstrapped features.

Chapter 6

Conclusions

The goal of this thesis was to develop a navigation algorithm suitable to estimate the position and velocity of the SC relative to Apophis, while simultaneously estimating the attitude and angular velocity of Apophis. The main obstacles to the estimation of these quantities were three: firstly, the state dynamics' uncertainties were significant, with gravitational gradient torques due to the proximity of Apophis to Earth being present, alongside non-modelled accelerations on the SC by the Moon; secondly, the absence of a detailed mapping of Apophis makes it so that there was no feature database in which to rely when resorting to relative orientation measurements; thirdly, the SC's position, when initializing Apophis attitude and, therefore, the tracked features, had a large uncertainty when compared to Apophis' radius.

To solve these problems, an MEKF was proposed, based on the absolute and relative dynamics of Apophis and the SC, respectively, with consideration of the measurement biases and dynamic uncertainties as FOGM. The measurements available to the observer were a relative distance to the surface of Apophis and relative orientation to Apophis' centre-of-mass, with both measurements corrupted by biases and white noises. Moreover, relative orientation measurements to features on Apophis' surface were also available, albeit in a shorter time-frame. The algorithm that was developed includes the possibility of self-initializing, or bootstrapping, previously unknown features, based on the current estimate of the SC's position, Apophis' attitude and a simplified geometrical model of Apophis' surface. Special attention was given to the initialization errors and their correlation to the states' uncertainties, measurement errors, and Apophis' surface model errors, studying and developing a strategy to cope with the nonlinear relationship between the states and the feature initialization. The feature tracking measurements were also underweighted, so that corrections would not leave the linearization region.

An environment was then created to test the filter, where the full dynamics were simulated and a noisy model of the Apophis' surface was employed to take into account the ruggedness of its surface. Furthermore, six filter variants were implemented to assess their individual and relative performances, with each one addressing a different measurement strategy.

The SC's position estimation results for filters with an altimeter showed that the introduction of feature tracking measurements considerably improved the errors in the direction tangential to Apophis' direction, up to an order of magnitude, without providing significant improvements to the radial errors. It could also be seen that the main gain in having *a priori* knowledge of the features is the almost instantaneous reduction in error, with the bootstrapped filter taking longer converge, but achieves a similar performance, and is boosted by improved centroiding measurements of Apophis. Furthermore, four out of one hundred cases were revealed to delay the application of features when using a database, due to the large error when first employing them. These cases, when using unknown features, led to an overconfidence of the filter's estimation, even if resulting in an effective reduction of the SC's position estimation error. The tests without the altimeter revealed that the overall performance of the filters is heavily dependent on this measurement, even if, as was the case for the filter using known filters, it could still improve the tangential position errors in an earlier phase.

The Apophis' rotation states estimation results made it clear that, without known features, the altimeter measurements are crucial to estimate Apophis' attitude. However, with known features, the employment of an altimeter is optional, with results similar to or better than the altimeter-able but feature-unknown variant. Moreover, the results point to a gradual, but slow, degradation of the Apophis' attitude estimation during the first half of the mission for the filter with unknown features, while the filter with a feature database was able to improve, even if only slightly, its Apophis' attitude estimation.

With the tests run for the filters, and conclusion for each estimated quantity drawn, it can be said that the proposed solution, relying on unknown features and an altimeter, is a viable option for the proposed goals. Moreover, the inclusion of depth measurements proved to be essential to the proper performance of the filter, revealing their need to the mission's success.

6.1 Future Work

The main limitation of the proposed solution within the assumptions made is the filter's overconfidence in its SC and tracked features' positions estimation, due to their non-linear relationship, and future work should address this issue. Two viable strategies are the introduction of an FOGM open to estimation into the features' positions estimates, which requires a complex tuning, and the replacement of the feature uncertainty correlation procedure during initialization by a sampling method that would directly compute the estimated correlation values.

Moreover, some assumptions could be lifted to better represent the real scenario in which the RAMSES mission will occur. Firstly, a better approximation to the real Apophis' surface would be an elongated ellipsoid instead of a sphere. This change would require a different procedure for the altitude measurements, since now the measurement is dependent on the Apophis' attitude. Assuming a larger bias in the altimeter measurement, while still employing a spherical model when not estimating Apophis' attitude and, once feature tracking measurements start, switch to the new model with the correspondent bias uncertainty would be an option that could work under the framework of this thesis. The Apophis inertial parameters were also considered to be fully known. This is, however, not true, as previous studies of Apophis point to a range of possible values for the moments of inertia. An improvement would be the inclusion of these uncertainties, be it by just considering them in the rotational dynamics or even estimate them, with a FOGM being a possible model to be employed.

Bibliography

[1] W. F. Truszkowski, M. G. Hinchey, J. L. Rash, and C. A. Rouff. Autonomous and autonomic systems: A paradigm for future space exploration missions. Technical report, NASA Goddard Space Flight Center, 2004. URL `https://ntrs.nasa.gov/api/citations/20050139706/downloads/20050139706.pdf`.

[2] C. Rouff. Autonomy in future space missions. 01 2002. URL `https://cdn.aaai.org/Workshops/2002/WS-02-03/WS02-03-010.pdf`.

[3] D. Gadisa and H. Bang. Small satellite electro-optical system (eos) technological and commercial expansion. *Acta Astronautica*, 213:355–372, 2023. ISSN 0094-5765. doi: https://doi.org/10.1016/j.actaastro.2023.09.010. URL `https://www.sciencedirect.com/science/article/pii/S0094576523004642`.

[4] S. Pedrotty, R. Lovelace, J. Christian, D. Renshaw, and G. Quintero. Design and performance of an open-source star tracker algorithm on commercial off-the-shelf cameras and computers. In *Annual AAS Guidance, Navigation and Control Conference*, 2020. URL `https://ntrs.nasa.gov/api/citations/20200001376/downloads/20200001376.pdf`.

[5] J. O. Woods and J. A. Christian. Lidar-based relative navigation with respect to non-cooperative objects. *Acta Astronautica*, 126:298–311, 2016. ISSN 0094-5765. doi: https://doi.org/10.1016/j.actaastro.2016.05.007. URL `https://www.sciencedirect.com/science/article/pii/S0094576515301661`. Space Flight Safety.

[6] Y. Takao, Y. Tsuda, T. Saiki, N. Ogawa, F. Terui, and J. Kawaguchi. *Optical Navigation for Asteroid Explorer by use of Virtual Feature Points*. 2016. doi: 10.2514/6.2016-5213. URL `https://arc.aiaa.org/doi/abs/10.2514/6.2016-5213`.

[7] F. Terui, N. Ogawa, G. Ono, S. Yasuda, T. Masuda, K. Matsushima, T. Saiki, and Y. Tsuda. Guidance, navigation, and control of hayabusa2 touchdown operations. *Astrodynamics*, 4, 11 2020. doi: 10.1007/s42064-020-0086-5.

[8] G. ONO et al. Gnc design and evaluation of hayabusa2 descent operations. *TRANSACTIONS OF THE JAPAN SOCIETY FOR AERONAUTICAL AND SPACE SCIENCES, AEROSPACE TECHNOLOGY JAPAN*, 19:259–265, 03 2021. doi: 10.2322/tastj.19.259.

[9] T. Yamaguchi et al. Hayabusa2-ryugu proximity operation planning and landing site selection. *Acta Astronautica*, 151:217–227, 2018. ISSN 0094-5765. doi: https://doi.org/10.1016/j.actaastro.2018.05.032. URL `https://www.sciencedirect.com/science/article/pii/S0094576518300365`.

[10] NASA. Osiris-rex in depth, 2024. URL `https://science.nasa.gov/mission/osiris-rex/in-depth/`.

[11] B. Rizk and et. all. Ocams: The osiris-rex camera suite. *Space Science Reviews*, 214, 01 2018. doi: 10.1007/s11214-017-0460-7.

[12] O. Barnouin et al. Shape of (101955) bennu indicative of a rubble pile with internal stiffness. *Nature Geoscience*, 12:1, 04 2019. doi: 10.1038/s41561-019-0330-x.

[13] B. Williams and D. others. Osiris-rex flight dynamics and navigation design. *Space Science Reviews*, 214(4), June 2018. ISSN 0038-6308. doi: 10.1007/s11214-018-0501-x. Publisher Copyright: © 2018, Springer Science+Business Media B.V., part of Springer Nature.

[14] E. S. Agency. Esa - hera, 2024. URL `https://www.esa.int/Space_Safety/Hera/Hera`.

[15] GMV. Presentation of hera gnc subsystem, 02 2023. URL `https://www.youtube.com/watch?v=jXb61n96j24`.

[16] E. S. Agency. Introducing ramses, esa's mission to asteroid apophis, 2024. URL `https://www.esa.int/Space_Safety/Planetary_Defence/Introducing_Ramses_ESA_s_mission_to_asteroid_Apophis`.

[17] D. N. DellaGiustina et al. Osiris-apex: An osiris-rex extended mission to asteroid apophis. *The Planetary Science Journal*, 4(10):198, oct 2023. doi: 10.3847/PSJ/acf75e. URL `https://dx.doi.org/10.3847/PSJ/acf75e`.

[18] C. J. Benson, D. J. Scheeres, M. Brozović, S. R. Chesley, P. Pravec, and P. Scheirich. Spin state evolution of (99942) apophis during its 2029 earth encounter. *Icarus*, 390:115324, 2023. ISSN 0019-1035. doi: https://doi.org/10.1016/j.icarus.2022.115324. URL `https://www.sciencedirect.com/science/article/pii/S001910352200416X`.

[19] C. Bonnal, J.-M. Ruault, and M.-C. Desjean. Active debris removal: Recent progress and current trends. *Acta Astronautica*, 85:51–60, 2013. ISSN 0094-5765. doi: https://doi.org/10.1016/j.actaastro.2012.11.009. URL `https://www.sciencedirect.com/science/article/pii/S0094576512004602`.

[20] B. D. Lucas and T. Kanade. An iterative image registration technique with an application to stereo vision. In *International Joint Conference on Artificial Intelligence*, 1981. URL `https://api.semanticscholar.org/CorpusID:2121536`.

[21] C. Tomasi and T. Kanade. *Detection and Tracking of Point Features*. Shape and motion from image streams. School of Computer Science, Carnegie Mellon Univ., 1991. URL `https://books.google.pt/books?id=20wpSQAACAAJ`.

[22] J. Shi and Tomasi. Good features to track. In *1994 Proceedings of IEEE Conference on Computer Vision and Pattern Recognition*, pages 593–600, 1994. doi: 10.1109/CVPR.1994.323794.

[23] C. Luo, W. Yang, P. Huang, and J. Zhou. Overview of image matching based on orb algorithm. *Journal of Physics: Conference Series*, 1237:032020, 06 2019. doi: 10.1088/1742-6596/1237/3/032020.

[24] M. A. Fischler and R. C. Bolles. Random sample consensus: A paradigm for model fitting with applications to image analysis and automated cartography. In M. A. Fischler and O. Firschein, editors, *Readings in Computer Vision*, pages 726–740. Morgan Kaufmann, San Francisco (CA), 1987. ISBN 978-0-08-051581-6. doi: https://doi.org/10.1016/B978-0-08-051581-6.50070-2. URL `https://www.sciencedirect.com/science/article/pii/B9780080515816500702`.

[25] S. Sharma and S. D'Amico. Comparative assessment of techniques for initial pose estimation using monocular vision. *Acta Astronautica*, 123:435–445, 2016. ISSN 0094-5765. doi: https://doi.org/10.1016/j.actaastro.2015.12.032. URL `https://www.sciencedirect.com/science/article/pii/S0094576515004713`. Special Section: Selected Papers from the International Workshop on Satellite Constellations and Formation Flying 2015.

[26] V. Capuano, K. Kim, A. Harvard, and S.-J. Chung. Monocular-based pose determination of uncooperative space objects. *Acta Astronautica*, 166:493–506, 2020. ISSN 0094-5765. doi: https://doi.org/10.1016/j.actaastro.2019.09.027. URL `https://www.sciencedirect.com/science/article/pii/S0094576519312949`.

[27] Djurdjani and D. Laksono. Open source stack for structure from motion 3d reconstruction: A geometric overview. *2016 6th International Annual Engineering Seminar (InAES)*, pages 196–201, 2016. URL `https://api.semanticscholar.org/CorpusID:38653594`.

[28] D. DeMenthon and L. DAVIS. Model-based object pose in 25 lines of code. *Lecture Notes in Computer Science*, 588:335–343, 01 1992. doi: 10.1007/BF01450852.

[29] R. E. Kalman. A New Approach to Linear Filtering and Prediction Problems. *Journal of Basic Engineering*, 82(1):35–45, 03 1960.

[30] M. I. Ribeiro. Kalman and extended kalman filters: Concept, derivation and properties, 2004. URL `http://users.isr.ist.utl.pt/~mir/pub/kalman.pdf`.

[31] C. Robert and G. Casella. *Monte Carlo Statistical Methods*. Springer Texts in Statistics. Springer New York, 2013. ISBN 9781475741452. URL `https://books.google.pt/books?id=3G2vBQAAQBAJ`.

[32] E. Wan and R. Van Der Merwe. The unscented kalman filter for nonlinear estimation. In *Proceedings of the IEEE 2000 Adaptive Systems for Signal Processing, Communications, and Control Symposium (Cat. No.00EX373)*, pages 153–158, 2000. doi: 10.1109/ASSPCC.2000.882463.

[33] S. Bitzer. Ukf-exposed: First public version of the ukf exposed report. 2016. doi: https://doi.org/10.5281/zenodo.44386.

[34] J. L. Parreira, P. Lourenço, and P. Batista. Globally convergent near-optimal pose and inertia estimation of on-orbit uncooperative targets. *IEEE Transactions on Aerospace and Electronic Systems*, 60(4):4479–4491, 2024. doi: 10.1109/TAES.2024.3381925.

[35] V. Pesce, M. Lavagna, and R. Bevilacqua. Stereovision-based pose and inertia estimation of unknown and uncooperative space objects. *Advances in Space Research*, 59(1):236–251, 2017. ISSN 0273-1177. doi: https://doi.org/10.1016/j.asr.2016.10.002. URL `https://www.sciencedirect.com/science/article/pii/S0273117716305622`.

[36] P. Cassinis. Delft university of technology review of the robustness and applicability of monocular pose estimation systems for relative navigation with an uncooperative spacecraft. 2019. URL `https://api.semanticscholar.org/CorpusID:197446229`.

[37] M. Kisantal, S. Sharma, T. Park, D. Izzo, M. Märtens, and S. D'Amico. Satellite pose estimation challenge: Dataset, competition design and results, 11 2019.

[38] J. Diebel. Representing attitude: Euler angles, unit quaternions, and rotation vectors. *Matrix*, 58, 01 2006.

[39] J. Solà. Quaternion kinematics for the error-state kalman filter. *ArXiv*, abs/1711.02508, 2015. URL `https://api.semanticscholar.org/CorpusID:3754816`.

[40] A. Bani Younes, J. Turner, D. Mortari, and J. Junkins. A survey of attitude error representations. 08 2012. ISBN 978-1-62410-182-3. doi: 10.2514/6.2012-4422.

[41] J. S. Subirana, J. J. Zornoza, and M. Hernández-Pajares. Conventional celestial reference system - navipedia, 2011. URL `https://gssc.esa.int/navipedia/index.php/Conventional_Celestial_Reference_System`.

[42] A. Farres. 21 - propellant-less systems. In F. Branz, C. Cappelletti, A. J. Ricco, and J. W. Hines, editors, *Next Generation CubeSats and SmallSats*, pages 519–541. Elsevier, 2023. ISBN 978-0-12-824541-5. doi: https://doi.org/10.1016/B978-0-12-824541-5.00019-4. URL `https://www.sciencedirect.com/science/article/pii/B9780128245415000194`.

[43] P. Gil. *Elementos de Mecânica Orbital*. IST, 1.1.6 edition, 2015.

[44] P. Pravec et al. The tumbling spin state of (99942) apophis. *Icarus*, 233:48–60, 2014. ISSN 0019-1035. doi: https://doi.org/10.1016/j.icarus.2014.01.026. URL `https://www.sciencedirect.com/science/article/pii/S0019103514000578`.

[45] M. Kaasalainen. Interpretation of lightcurves of precessing asteroids. *A&A*, 376:302–309, 09 2001. doi: 10.1051/0004-6361:20010935.

[46] Y. Wang and S. Xu. Gravity gradient torque of spacecraft orbiting asteroids. *Aircraft Engineering and Aerospace Technology: An International Journal*, 85, 11 2013. doi: 10.1108/00022661311294049.

[47] J. A. Christian and S. P. Cryan. A survey of lidar technology and its use in spacecraft relative navigation. In *AIAA Guidance, Navigation and Control Conference*, 2013. URL `https://ntrs.nasa.gov/api/citations/20140000616/downloads/20140000616.pdf`.

[48] V. Pasqualetto Cassinis, R. Fonod, and E. Gill. Review of the robustness and applicability of monocular pose estimation systems for relative navigation with an uncooperative spacecraft. *Progress in Aerospace Sciences*, 110:100548, 2019. ISSN 0376-0421. doi: https://doi.org/10.1016/j.paerosci.2019.05.008. URL `https://www.sciencedirect.com/science/article/pii/S0376042119300302`.

[49] C. A. Wright, A. J. Liounis, and B. W. Ashman. Optical navigation algorithm performance. In *Annual RPI Workshop on Image-Based Modeling and Navigation for Space Applications*, 2018. URL `https://ntrs.nasa.gov/api/citations/20180003620/downloads/20180003620.pdf`.

[50] D. Grest, T. Petersen, and V. Krüger. A comparison of iterative 2d-3d pose estimation methods for real-time applications. In A.-B. Salberg, J. Y. Hardeberg, and R. Jenssen, editors, *Image Analysis*, pages 706–715, Berlin, Heidelberg, 2009. Springer Berlin Heidelberg. ISBN 978-3-642-02230-2.

[51] L. A. Mcgee and S. F. Schmidt. Discovery of the kalman filter as a practical tool for aerospace and industry. Technical report, NASA Ames Research Center, 1985. URL `https://ntrs.nasa.gov/api/citations/19860003843/downloads/19860003843.pdf`.

[52] J. R. Carpenter and C. N. D'Souza. Navigation filter best practices. Technical report, NASA Langley Research Center, 2018. URL `https://ntrs.nasa.gov/api/citations/20180003657/downloads/20180003657.pdf`.

[53] V. Madyastha, V. Ravindra, S. Mallikarjunan, and A. Goyal. Extended kalman filter vs. error state kalman filter for aircraft attitude estimation. 08 2011. ISBN 978-1-60086-952-5. doi: 10.2514/6.2011-6615.

[54] S. F. Schmidt. Application of state-space methods to navigation problems. volume 3 of *Advances in Control Systems*, pages 293–340. Elsevier, 1966. doi: https://doi.org/10.1016/B978-1-4831-6716-9.50011-4. URL `https://www.sciencedirect.com/science/article/pii/B9781483167169500114`.

[55] R. Zanetti and C. D'Sousa. Recursive implementations of the schmidt-kalman consider filter. *Journal of the Astronautical Sciences*, 60:672–685, 2013. doi: https://doi.org/10.1007/s40295-015-0068-7. URL `https://arxiv.org/abs/2203.06105`.

[56] J. H. Ramos, K. Brink, P. Ganesh, and J. E. Hurtado. A summary on the ud kalman filter, 2022. URL `https://arxiv.org/abs/2203.06105`.

[57] C. Gramsch, S. Yang, and H. Alqaderi. A batch update using multiplicative noise modelling for extended object tracking. pages 1–8, 07 2024. doi: 10.23919/FUSION59988.2024.10706375.

[58] R. E. Hodges, O. S. Sands, J. Huang, and S. Bassily. High-capacity communications from martian distances part 4: Assessment of spacecraft pointing accuracy capabilities required for large ka-band reflector antennas. Technical report, NASA Glenn Research Center, 2006. URL `https://ntrs.nasa.gov/api/citations/20070010456/downloads/20070010456.pdf`.

[59] NASA. About spice, 2024. URL `https://naif.jpl.nasa.gov/naif/aboutspice.html`.

[60] K. Perlin. In the beginning: The pixel stream editor.

[61] T. Möller and B. Trumbore. Fast, minimum storage ray-triangle intersection. *Journal of Graphics Tools*, 2, 08 2005. doi: 10.1145/1198555.1198746.

[62] Jarek Tuszynski. Triangle/ray intersection. URL `https://www.mathworks.com/matlabcentral/fileexchange/33073-triangle-ray-intersection`.

Appendix A

Background

A.1 Reference frames

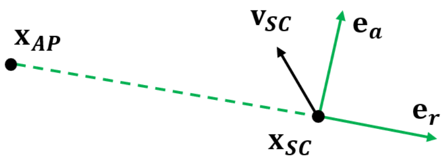

Figure A.1: $\{\mathcal{RAC}\}$ reference frame.

A.2 Measurements

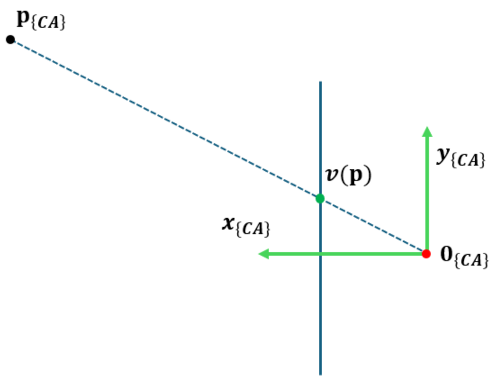

Figure A.2: 2D Pinhole projection.

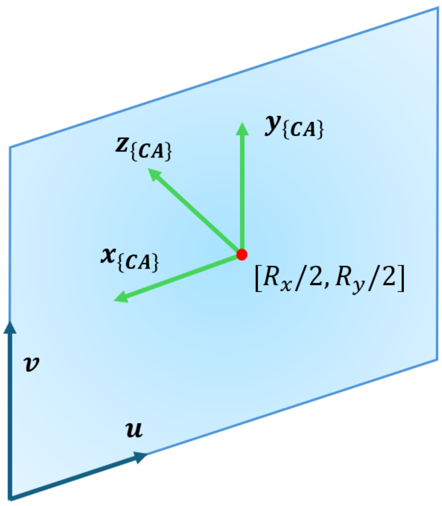

Figure A.3: Relation of $\{\mathcal{CA}\}$ and pixel output.

Appendix B

Problem Approach

B.1 Filter Design

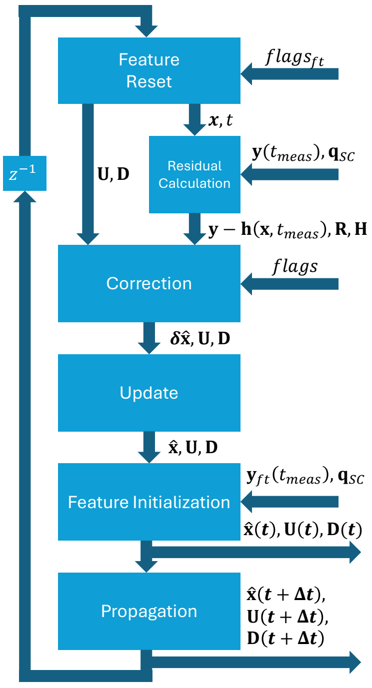

Quantity	Symbol
Covariance	$\mathbf{P} = \mathbf{U}\mathbf{D}\mathbf{U}^\mathsf{T}$
Estimated Nominal State	$\hat{\mathbf{x}}$
Estimated Error State	$\delta\hat{\mathbf{x}}$
Measurements	$\mathbf{y}$
Observation function	$\mathbf{h}(.)$
Observation Matrix	$\mathbf{H}$
Measurement Noise Matrix	$\mathbf{R}$
SC attitude	$\mathbf{q}_{SC}$
Delay	z^{-1}

Figure B.1: Filter Diagram

Name	Nominal State	Error State	Composition operation	Nominal Units	Error Units
Position of the SC	${}^{\mathcal{CI}}\mathbf{x}_{SC}$	$\delta {}^{\mathcal{CI}}\mathbf{x}_{SC}$	${}^{\mathcal{CI}}\mathbf{x}_{SC} + \delta {}^{\mathcal{CI}}\mathbf{x}_{SC}$	m	
Velocity of the SC	${}^{\mathcal{CI}}\mathbf{v}_{SC}$	$\delta {}^{\mathcal{CI}}\mathbf{v}_{SC}$	${}^{\mathcal{CI}}\mathbf{v}_{SC} + \delta {}^{\mathcal{CI}}\mathbf{v}_{SC}$	ms^{-1}	
Non-modelled acceleration of the SC	${}^{\mathcal{CI}}\mathbf{a}_{nm,SC}$	$\delta {}^{\mathcal{CI}}\mathbf{a}_{nm,SC}$	${}^{\mathcal{CI}}\mathbf{a}_{nm,SC} + \delta {}^{\mathcal{CI}}\mathbf{a}_{nm,SC}$	ms^{-2}	
Altimeter bias	b_l	δb_l	$b_l + \delta b_l$	m	
Centroiding bias	b_c	δb_c	$b_c + \delta b_c$	%	
Attitude of Apophis	${}^{\mathcal{CI}}_{\mathcal{AP}}\mathbf{q}$	$\delta\boldsymbol{\theta}$	${}^{\mathcal{CI}}_{\mathcal{AP}}\mathbf{q} \odot \mathbf{q}\{\delta\boldsymbol{\theta}\}$	adim	rad
Angular velocity of Apophis	${}^{\mathcal{AP}}\boldsymbol{\omega}_{AP}$	$\delta {}^{\mathcal{AP}}\boldsymbol{\omega}_{AP}$	${}^{\mathcal{AP}}\boldsymbol{\omega}_{AP} + \delta {}^{\mathcal{AP}}\boldsymbol{\omega}_{AP}$	rad s^{-1}	
Non-modelled torques of Apophis	${}^{\mathcal{AP}}\boldsymbol{\tau}_{nm,AP}$	$\delta {}^{\mathcal{AP}}\boldsymbol{\tau}_{nm,AP}$	${}^{\mathcal{AP}}\boldsymbol{\tau}_{AP} + \delta {}^{\mathcal{AP}}\boldsymbol{\tau}_{AP}$	Nm^{-1}	
Feature position	${}^{\mathcal{AP}}\mathbf{x}_{ft,i}$	$\delta {}^{\mathcal{AP}}\mathbf{x}_{ft,i}$	${}^{\mathcal{AP}}\mathbf{x}_{ft,i} + \delta {}^{\mathcal{AP}}\mathbf{x}_{ft,i}$	m	

Table B.1: Filter's States' Descriptions

Appendix C

Simulation Environment and Results

C.1 Simulation Results

C.1.1 All

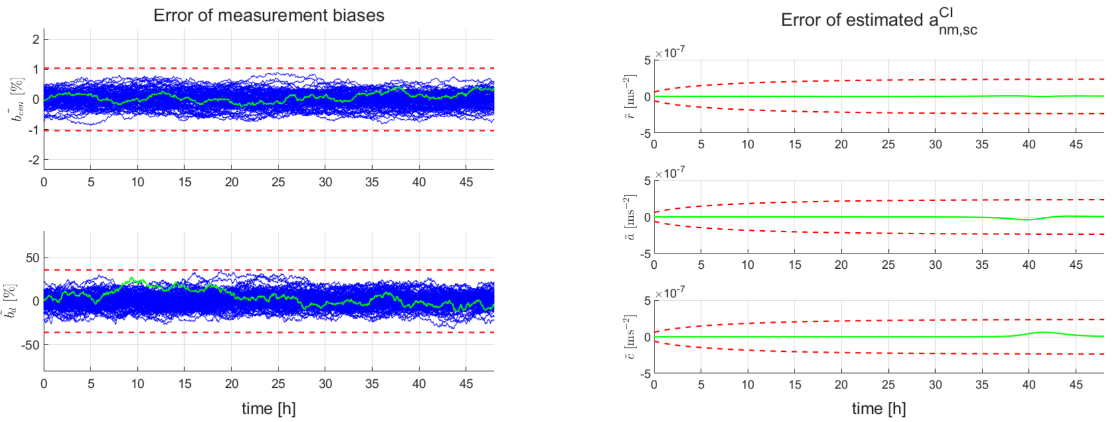

(a) Measurement biases.

(b) Non-modelled accelerations of the SC.

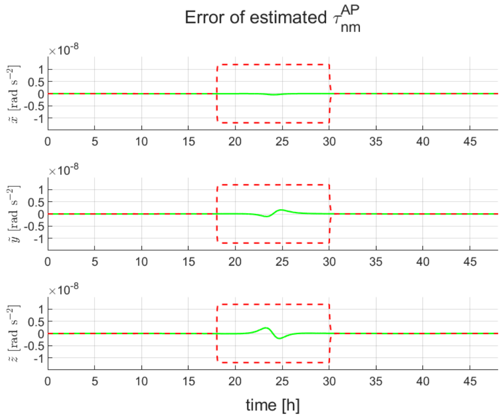

(c) Non-modelled torques of Apophis.

Figure C.1: Biases errors for all filters.

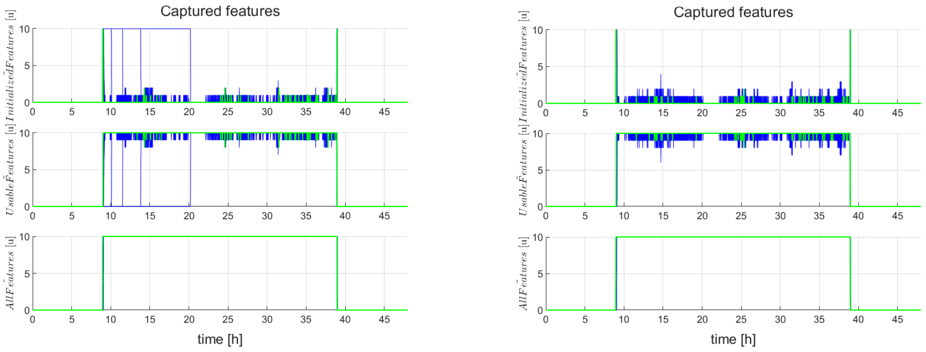

(a) FIL 1111.

(b) FIL 1110.

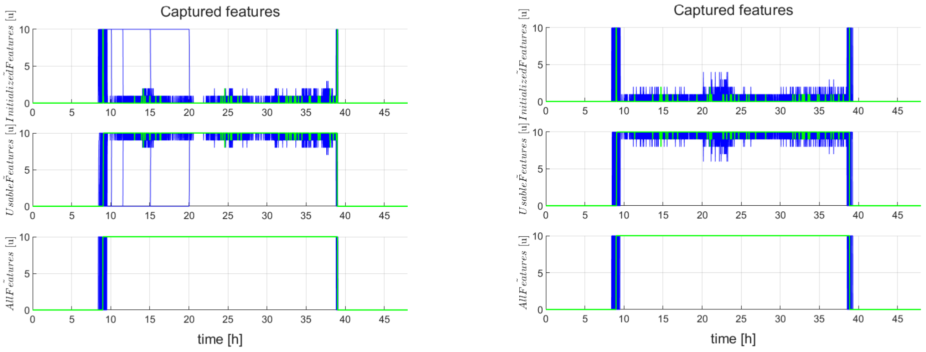

(c) FIL 0111.

(d) FIL 0110.

Figure C.2: Feature status for different filters during Monte Carlo Simulations.

C.1.2 FIL 1100

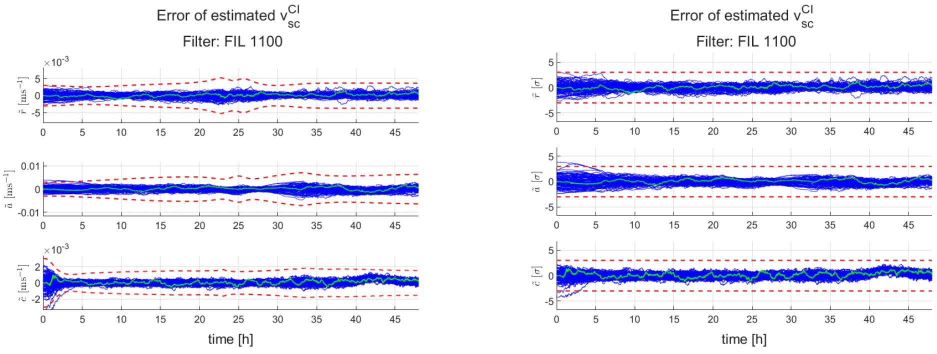

(a) Errors.

(b) Normalized errors.

Figure C.3: FIL 1100 velocity estimation errors.

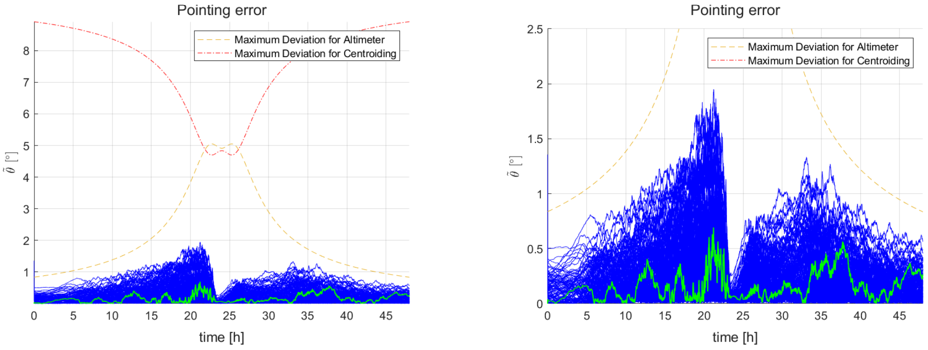

(a) Overview.

(b) Detail.

Figure C.4: FIL 1100 SC pointing errors.

C.1.3 FIL 1111

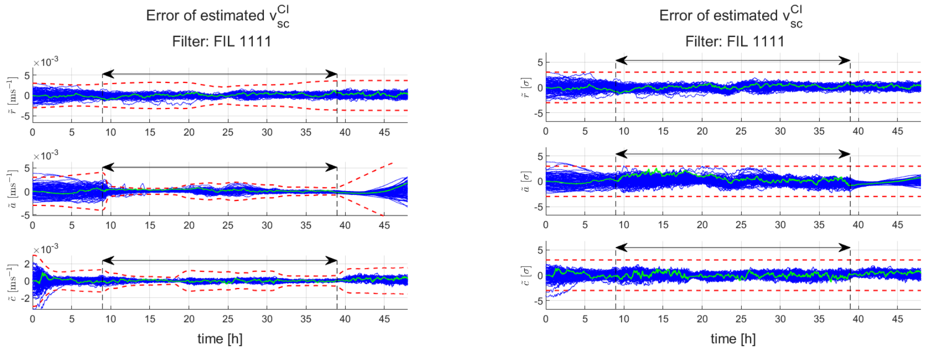

(a) Errors.

(b) Normalized errors.

Figure C.5: FIL 1111 velocity estimation errors.

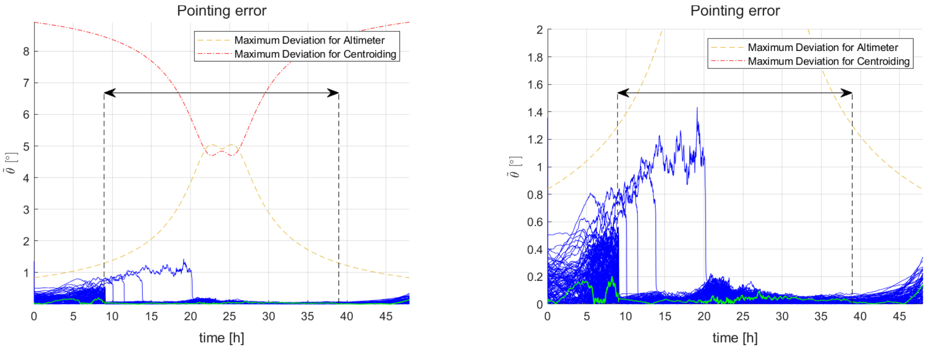

(a) Overview.

(b) Detail.

Figure C.6: FIL 1111 SC pointing errors.

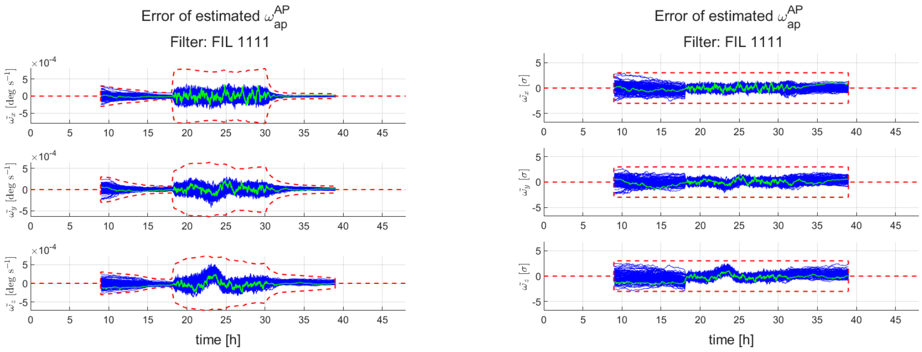

(a) Errors.

(b) Normalized errors.

Figure C.7: FIL 1111 angular velocity estimation errors.

C.1.4 FIL 1110

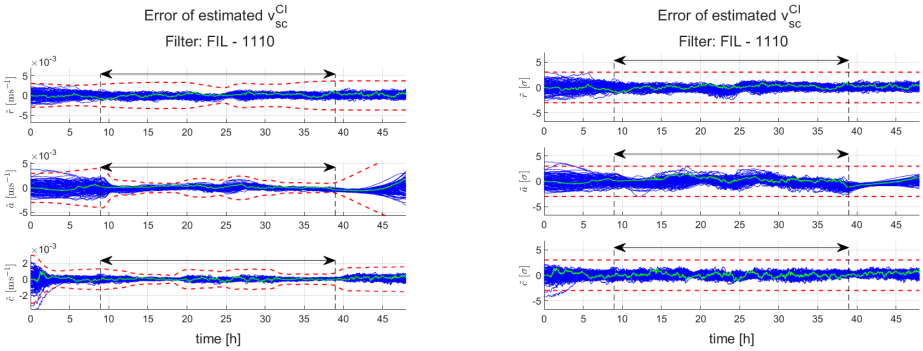

(a) Errors.

(b) Normalized errors.

Figure C.8: FIL 1110 velocity estimation errors.

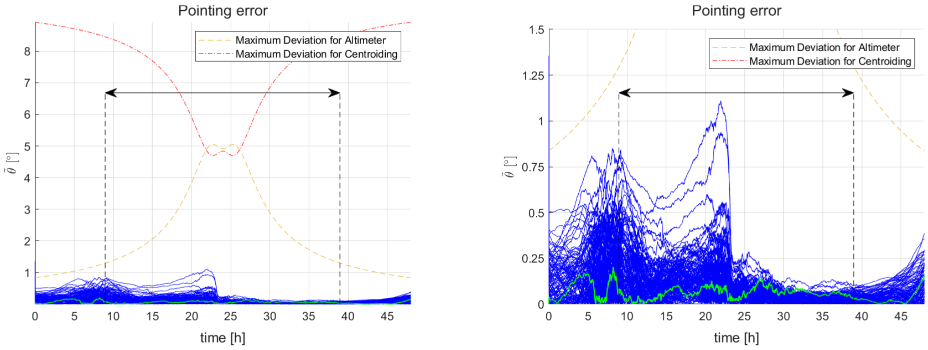

(a) Overview.

(b) Detail.

Figure C.9: FIL 1110 SC pointing errors.

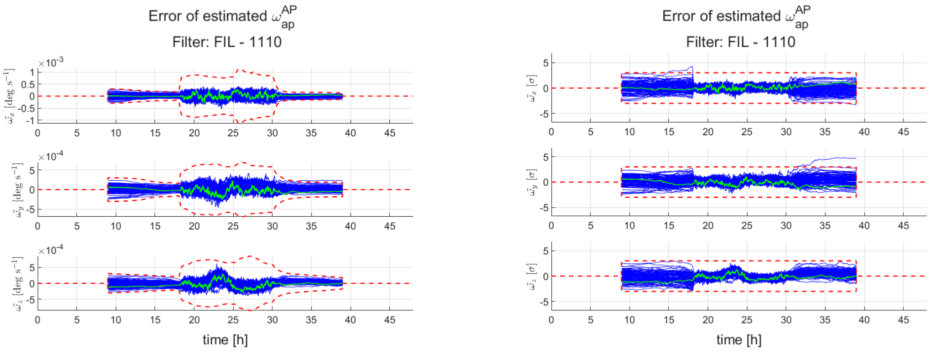

(a) Errors.

(b) Normalized errors.

Figure C.10: FIL 1110 angular velocity estimation errors.

C.1.5 FIL 0100

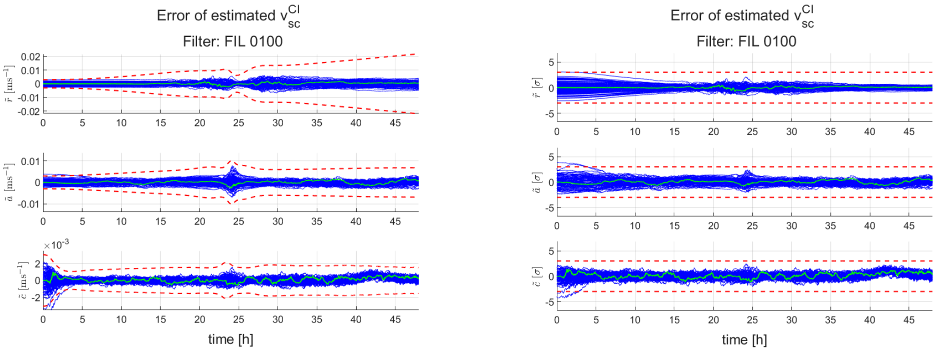

(a) Errors.

(b) Normalized errors.

Figure C.11: FIL 0100 velocity estimation errors.

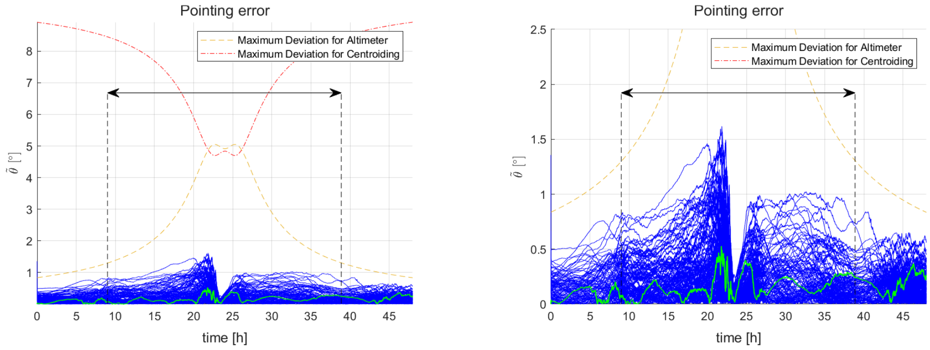

(a) Overview.

(b) Detail.

Figure C.12: FIL 0100 SC pointing errors.

C.1.6 FIL 0111

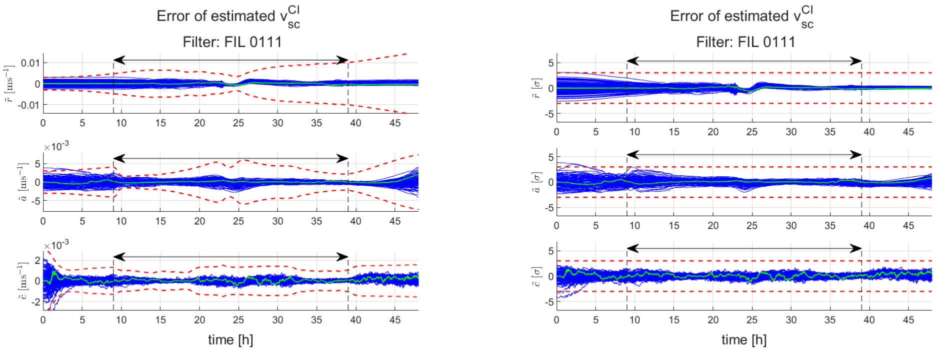

(a) Errors.

(b) Normalized errors.

Figure C.13: FIL 0111 SC velocity estimation errors.

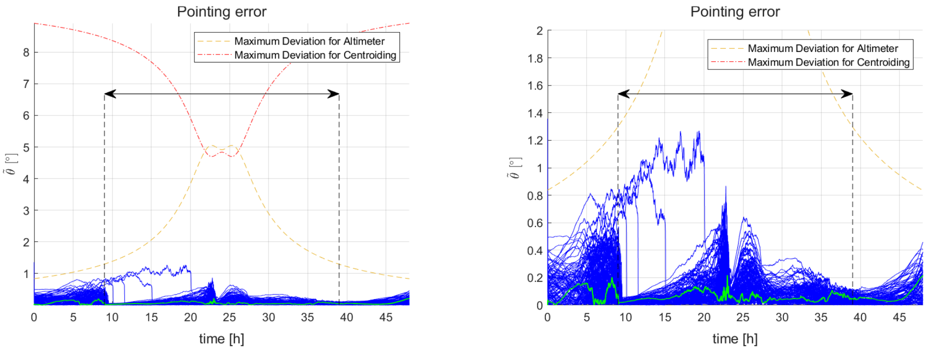

(a) Overview.

(b) Detail.

Figure C.14: FIL 0111 SC pointing errors.

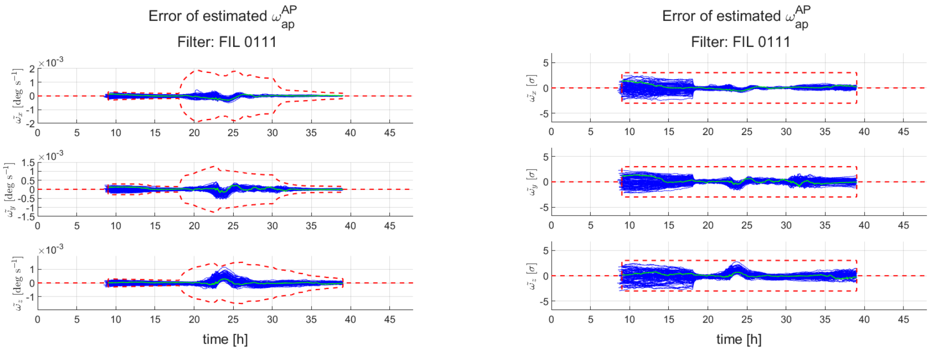

(a) Errors.

(b) Normalized errors.

Figure C.15: FIL 0111 Apophis angular velocity estimation errors.

C.1.7 FIL 0110

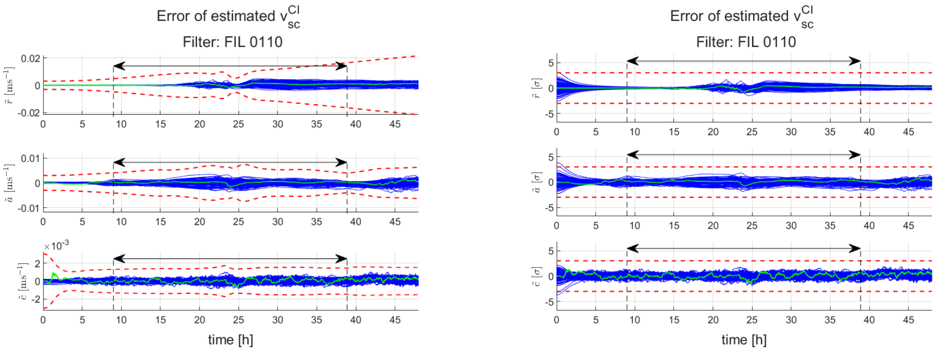

(a) Errors.

(b) Normalized errors.

Figure C.16: FIL 0110 velocity estimation errors.

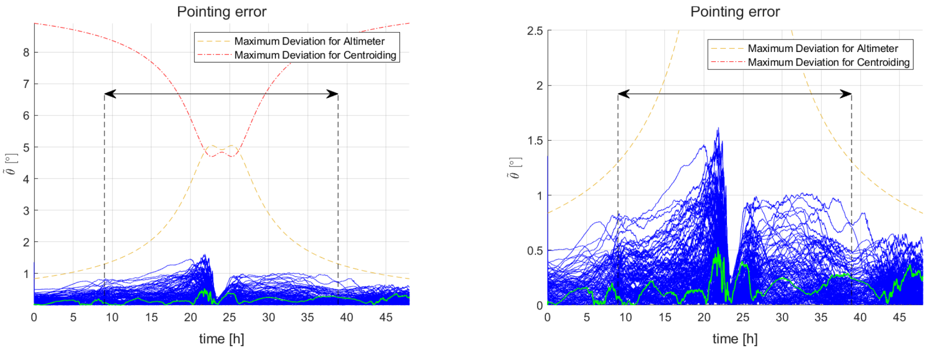

(a) Overview.

(b) Detail.

Figure C.17: FIL 0110 SC pointing errors.

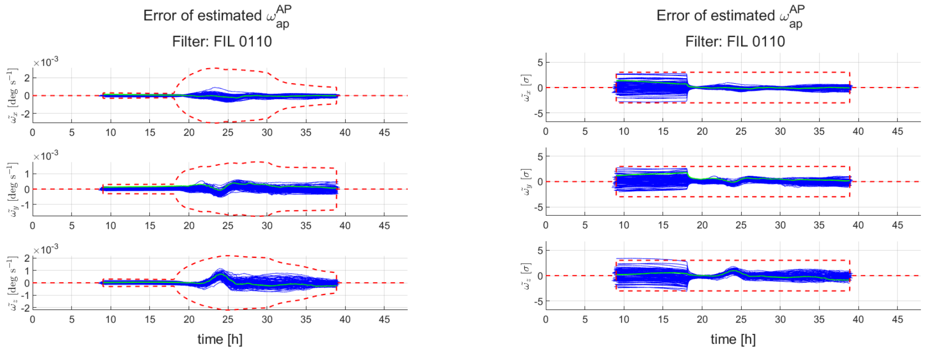

(a) Errors.

(b) Normalized errors.

Figure C.18: FIL 0110 angular velocity estimation errors.